8-14-2008

Stimulated Brillouin Scattering Phase Conjugation in Fiber Optic Waveguides

Steven M. Massey

STIMULATED BRILLOUIN SCATTERING PHASE CONJUGATION IN FIBER OPTIC WAVEGUIDES

DISSERTATION

Steven M. Massey, Major, USAF
AFIT/DS/ENP/08-S03

DEPARTMENT OF THE AIR FORCE
AIR UNIVERSITY

AIR FORCE INSTITUTE OF TECHNOLOGY

Wright-Patterson Air Force Base, Ohio

APPROVED FOR PUBLIC RELEASE

The views expressed in this thesis are those of the author and do not reflect the official policy or position of the United States Air Force, Department of Defense, or the United States Government

AFIT/DS/ENP/08-S03

STIMULATED BRILLOUIN SCATTERING PHASE CONJUGATION IN FIBER OPTIC WAVEGUIDES

DISSERTATION

Presented to the Faculty

Department of Engineering Physics

Graduate School of Engineering and Management

Air Force Institute of Technology

Air University

Air Education and Training Command

In Partial Fulfillment of the Requirements for the

Degree of Doctor of Philosophy

Steven M. Massey, BS, MS

Major, USAF

July 2008

APPROVED FOR PUBLIC RELEASE

AFIT/DS/ENP/08-S03

STIMULATED BRILLOUIN SCATTERING PHASE CONJUGATION IN FIBER OPTIC WAVEGUIDES

Steven M. Massey, BS, MS
Major, USAF

Approved:

Timothy H. Russell (Chairman)	Date
Glen P. Perram (Member)	Date
Jason D. Schmidt (Member)	Date

Accepted:

Marlin U. Thomas Dean, Graduate School of Engineering and Management	Date

Abstract

The objective of this research effort was to demonstrate the path to continuous wave, coherent beam combination through stimulated Brillouin scattering phase conjugation in optical fiber. This work experimentally determined the fiber parameters necessary for phase conjugation in step-index optical fiber. Continuous wave phase conjugation using stimulated Brillouin scattering in step-index fibers was achieved for the first time with a fidelity of 0.8 and a threshold power of 16 W in a 15-m fiber with 0.13 NA. A fidelity of 0.8 was also achieved using 40 m of fiber with 0.06-NA and a threshold power of 15 W. The fidelity of phase conjugation was found to decline by ~45% in an additional 20 m of 0.13-NA fiber and by ~15% in 20 m of the 0.06-NA fiber. The effective Brillouin gain coefficient of the multimode fibers was found to vary directly with fidelity. A new technique using interference to measure fidelity was tested, and stimulated Brillouin scattering in a 2.5-km, graded-index fiber was found to produce beam cleanup to the fundamental fiber mode of the fiber with fidelity less than 0.1. This work demonstrated that coherent beam combining via continuous wave phase conjugation in optical fiber is achievable.

Acknowledgments

I sincerely appreciate the guidance and support given by my faculty advisor, Major Timothy Russell, throughout this research effort. He was always available to provide technical advice and direction. I would also like to thank the High Energy Laser Joint Technology Office for their primary financial contributions to this research effort, and acknowledge the Air Force Research Laboratory for being generous with their equipment and knowledge. Finally, thank you to my committee, Major Jason Schmidt and Dr. Glen Perram, for their constructive criticism at key points during the completion of this work.

Steven M. Massey

Table of Contents

List of Figures

List of Tables

STIMULATED BRILLOUIN SCATTERING PHASE CONJUGATION IN FIBER OPTIC WAVEGUIDES

1. Introduction

1.1. Motivation

The laser is in use in a wide variety of applications on the battlefield and commercially. Automakers employ high-power lasers for precision welding, and it is an instrumental tool in medicine, communications, and data storage. Laser-guided munitions have led a revolution in warfare, resulting in the capability to attack multiple targets per sortie instead of multiple sorties per target.[1]

Lasers are being developed for an expanded role in warfare. For ballistic missile defense, advanced laser radar devices are being developed with such precision that the capability to discriminate between warheads and decoys midcourse is becoming a reality.[2] For this purpose, high power lasers with ultra-narrow bandwidth are needed for long range and precision tracking. This same technology is being developed for the detection of gases, aerosols, and wind velocity measurements.[3] Using laser radar systems, chemical and biological defenses are being improved and dangerous wind conditions at airports can be detected.

The laser is also being developed as a weapon with the promise of speed-of-light delivery and unparalleled precision. The most notable aircraft platforms are the

Advanced Tactical Laser (ATL) and the Airborne Laser (ABL).[4] The ATL is a program to deploy a "kilowatt class" chemical laser on a C-130H Gunship for precision strike purposes. The ABL program is developing a "megawatt class" chemical laser on a 747 designed to destroy ballistic missiles in boost phase. While chemical lasers' power is unmatched, the method of producing the power is through a chemical reaction involving high purity basic hydrogen peroxide and chlorine. The logistics burden of chemical lasers has prompted the DoD to develop solid-state lasers for high-power applications such as the 100 kW Joint High Power Solid-State Laser program.

For the success of laser weapons, the high power laser is needed in addition to advanced beam control and atmospheric compensation methods. Propagation of the laser through the atmosphere can severely degrade the beam quality of the laser and result in a much shorter kill range. Deformable optics are being used for atmospheric compensation on ground-based telescopes for space object identification and tracking.[5] The Starfire Optical Range in Albuquerque NM employs a laser to generate a fluorescent "star" at 90 km above ground level. Wavefront sensors detect the aberrations from this source and deformable optics are used to compensate these aberrations. With atmospheric aberrations reduced, the telescope provides a clear view of space objects.

The correction of aberrations is also necessary to generate high powers in bulk solid-state lasers. One approach to generating high power in a solid-state laser is with a master oscillator followed by power amplifiers (MOPA). Non-uniform heating in the amplifying medium causes aberrations that limit the beam quality of these laser systems. By using wavefront reversal after the first pass through the amplifiers, a second pass through the amplifiers corrects the beam quality rather than causing further aberrations.

Phase conjugation via stimulated Brillouin scattering (SBS) has been used for generating wavefront reversal.[6] In a similar application, SBS has been used for atmospheric compensation using a retroreflector in laboratory tests which demonstrated high precision tracking as well as phase conjugation.[7]

To improve the beam quality of solid-state lasers, high-power systems have been constructed using fiber-optic lasers and amplifiers. Optical fibers can be designed with inherently good beam quality and excellent thermal management, and powers over 2 kW have been demonstrated.[8] While there are predictions that single-element power scaling can exceed 10 kW before material constraints limit the power,[9] combining multiple amplifier channels into a single beam could allow orders of magnitude power increases.

The elements can be combined using coherent methods or incoherent methods. Spectral beam combining is one promising example of incoherent beam combining.[10] In the reverse process of splitting a beam into spectral components using a grating, multiple beams are incident on a grating from different angles with slightly different frequencies. The result is a single spatial beam comprised of multiple frequencies. Incoherent beam combining adds the irradiance of each beam to result in an overall irradiance that is proportional to the number of beams. In contrast, coherent beam combining locks the phase, frequency, and polarization of each beamlet such that the electric fields of each beam add constructively. This results in peak irradiance that is proportional to the number of beams squared.

The first step to coherent beam combination is generating a high-power single-element beam that is single-frequency and single-polarization. For fiber lasers, the

limitation on single-frequency power from a single element is currently stimulated Brillouin scattering in fiber amplifiers.[11] When the irradiance exceeds a critical value in a given length of fiber, a density wave in the material forms and acts as a moving Bragg grating to reflect the incident beam. This process effectively clamps the power transmission of the fiber. The highest reported single-frequency fiber amplifier achieved 511 W.[12]

Coherent beam combining requires that the phase and polarization of each beamlet is matched to within a fraction of a wavelength. Typically, the optical path length of each beamlet must be controlled due to dynamic fluctuations caused by heating and vibrations.[10] One method of locking the phases of each beamlet is to generate a phase conjugate reflection and propagate the beamlets back through the amplifiers in a second pass.[13] Under certain circumstances, the beam reflected by SBS is the phase-conjugate of the incident beam. Therefore, stimulated Brillouin scattering may limit the power achievable through a single beam, but it also provides a means of coherently combining multiple beams.

1.2. Overview

The objective of this research effort is to demonstrate the path to cw coherent beam combination through SBS phase conjugation in optical fiber. The theoretical background is presented in Chapter 2, starting with the physics of nonlinear optics. Stimulated Brillouin scattering is shown to arise from specific conditions of nonlinear optics, and the chapter concludes with a study of SBS phase conjugation. Relevant experimental work in SBS phase conjugation is reviewed in Chapter 3. This review of the literature traces the achievements from the first observation of SBS in waveguides in

1972 through the experimental pulsed laser systems that have successfully used SBS phase conjugation to achieve higher pulse-power, to the current challenge of avoiding SBS in high power fiber amplifiers. Particular emphasis is placed on demonstrations of SBS phase conjugation, the degree of phase conjugation (conjugation fidelity), and the irradiance required for SBS to occur under various conditions and in a variety of materials. The chapter concludes with a review of techniques in coherent beam combining.

Phase conjugation via SBS in optical fiber had not been demonstrated using a cw signal beam prior to this work. Continuous operation represents the limiting case of the lowest possible peak power with the highest average power, which is desired for use in weapons applications where the goal is to apply the most power onto a target. CW phase conjugation is preferred over pulsed systems for combining fiber amplifiers because the small cross-sectional area of fibers is prone to damage from high pulse powers. Since SBS threshold requires high irradiance, phase conjugation via SBS with cw operation presents the greatest challenge in terms of average power required.

One of the main goals of this research effort is to observe a trend in conjugation fidelity as a function of fiber length. The trend data regarding phase-conjugation fidelity as a function of fiber length is needed to show the power and beam quality necessary to achieve high-fidelity phase conjugation. Furthermore, this data is very useful for power and efficiency considerations in laser system design. For example, a fidelity of 0.8 may be an acceptable trade over a fidelity of 0.98 if it results in a 90% decrease in SBS threshold with a similar decrease in irradiance-induced damage. The trend in fidelity with fiber length was measured using moderately multimode silicate fiber and a high-

power, cw signal beam, and is presented in Chapter 6. This study was necessary since the theory that existed prior to the start of this work, presented in Chapter 2, is valid only for fidelity near 1. In addition, the experimental efforts using pulsed lasers were unable to characterize the decrease in fidelity with fiber length. This trend was measured in the laboratory for two different fibers and guided a model of the behavior performed by a Master's student in our research group. Using the model, a third fiber was examined, and, together with the experimental measurements, a correlation between the fiber parameters and fidelity was realized. This correlation allows the SBS threshold power for a given fidelity to be plotted as a function of beam quality accepted by a step-index fiber. Lastly, by measuring the SBS threshold simultaneously with the fidelity of phase conjugation, increases in fidelity were shown to decrease the SBS threshold compared to previous threshold models.

In order to complete this goal, an investigation into predicting the SBS thresholds of various candidate fibers was undertaken (Chapter 4). A model of SBS threshold was constructed which could accommodate scattering or absorption losses, different gain coefficients, and fiber amplifiers with flexible pump geometry. While previous models had ignored the difference between co-pumping and counter-pumping, this model demonstrated that the SBS threshold power could be doubled by choosing the counter-pumped geometry over co-pumping fiber amplifiers. This model was then used to design and build high-power fiber amplifiers free from nonlinear effects by choosing the pump geometry and fiber length for the amplified power predicted. However, the main use of the model was to compare candidate fiber materials for SBS phase conjugation testing, specifically looking for those with low SBS thresholds. In the process, Brillouin gain

coefficients measured by multiple research groups were unified under a single model of Brillouin gain broadening as a function of fiber NA. By including scattering loss without an approximation for low-loss, the accuracy of calculating SBS threshold was significantly improved over the previous threshold models for fibers with large scattering losses.

Methods for measuring fidelity were analyzed and tested, and a new measure of fidelity was devised and tested as described in Chapter 5. This new fidelity measurement technique relies on fringe contrast to measure fidelity equally well over the full range from zero to one. The fidelity measurements described from the literature in Chapter 3 rely on beam quality measurements or power-in-the-bucket techniques. As pass/fail measurements, these techniques are relatively accurate, but can be misleading when beam cleanup occurs. The in-line pinhole method was shown to distinguish between beam cleanup and phase conjugation while simultaneously confirming the beam-cleanup effect resulting from SBS in a graded-index fiber. A more accurate approach to measuring the fidelity of phase conjugation was tested which employs the ability of SBS phase conjugation to phase-lock two beam paths. This method was verified using a graded-index fiber to generate beam cleanup and measuring a fidelity much less than one. This contrasts the pinhole measurement of the same effect which yielded a large range of "fidelity" values between zero and 0.6 depending on fiber alignment.

Finally, using the results of this work, coherent beam combination of a two-channel fiber amplifier at 1550 nm was attempted using a chalcogenide fiber to generate a phase conjugate beam via SBS.

For reference, a glossary of symbols has been provided at the back of this dissertation.

2. Theoretical Background

In this chapter, I present the physics governing the process of phase conjugation via stimulated Brillouin scattering (SBS) in optical fiber waveguides starting with Maxwell's equations. Brillouin scattering is a 2-photon resonant process which interacts with phonons in the material. It can be described classically as a reflection of the signal field off of an acoustic wave in the material which is reinforced through the process of electrostriction.

2.1. Nonlinear Optics

The field of nonlinear optics arises from Maxwell's equations, given here in a dielectric material where there are no free currents or charges:[14]

$$\nabla \bullet \mathbf{D} = 0 \tag{2.1}$$

$$\nabla \times \mathbf{H} = \frac{\partial \mathbf{D}}{\partial t} \tag{2.2}$$

$$\nabla \times \mathbf{E} = -\frac{\partial \mathbf{B}}{\partial t} \tag{2.3}$$

$$\nabla \bullet \mathbf{B} = 0\,. \tag{2.4}$$

A dielectric in the presence of an electric field can be envisioned as a grouping of dipoles bound together representing electrons with ion nuclei. As the field passes through the material, negatively charged electrons move against the field while positively charged ions move with the field. These charged particles are constrained by the lattice forming the solid dielectric and exhibit damped harmonic motion. The lattice may bind the particles evenly in all directions, or the particles may be bound in some directions stronger than others to form an anisotropic material. The field interaction with the

material causes oscillation among the bound dipoles. The polarization **P** of the material is the dipole moment per unit volume, and the electric displacement is then defined as

$$\mathbf{D} = \varepsilon_o \mathbf{E} + \mathbf{P} \tag{2.5}$$

where ε_o is the permittivity of free space.

Since the nuclei are much more massive than the electrons, the motion of the electrons typically dominates the polarization of the material under the influence of radiation in the optical regime (10^{14}-10^{16} Hz). When the amplitude of the incident field is small, the electron motion is approximately sinusoidal with the same frequency as the incident field. Classically, nonlinear effects arise because the restoring force on the electrons is anharmonic.[15] As the field amplitude increases, the motion of the electrons begins to deviate from that of the applied field and the polarization vector will include frequencies not present in the incident field. From the perspective of quantum mechanics, the higher field amplitude is represented by more photons incident on the same region of the material. Therefore, higher irradiance increases the probability for multiple photons to interact with the material in processes such as scattering or absorption.

The polarization in the material can be represented by a power series expansion of the electric field[16]

$$\mathbf{P} = \varepsilon_o [\chi^{(1)} + \chi^{(2)}\mathbf{E} + \chi^{(3)}\mathbf{E}\mathbf{E} + ...]\mathbf{E}\,, \tag{2.6}$$

where $\chi^{(1)}$ represents the linear susceptibility of the material, and the nonlinear susceptibilities are represented by $\chi^{(2)}$, $\chi^{(3)}$, and successive higher orders. The first-order polarization results in a linear material response to the applied field and is given by

$$\mathbf{P}^{(1)} = \varepsilon_o \chi^{(1)} \mathbf{E}\,. \tag{2.7}$$

The resulting electric displacement from a linear material polarization is

$$\mathbf{D} = \varepsilon_o(1+\chi^{(1)})\mathbf{E}. \tag{2.8}$$

Continuing the expansion as a function of the electric field,

$$\mathbf{D} = \varepsilon_o(1+\chi^{(1)}+\chi^{(2)}\mathbf{E}+\chi^{(3)}\mathbf{E}\mathbf{E}+...)\mathbf{E} \tag{2.9}$$

where $\chi^{(1)}$ is a 2nd rank tensor, $\chi^{(2)}$ is a 3rd rank tensor, $\chi^{(3)}$ is a 4th rank tensor, *etc*.

When the medium is isotropic such as gases, liquids, and glasses, the electric displacement can be approximated by just the linear and third-order susceptibility terms. The first approximation is to neglect terms higher than fourth order. What makes this possible is that, in general, the contributions to the displacement from each successive order of the expansion decrease by an order of magnitude.[16] Second, $\chi^{(1)}$ reduces to a scalar function represented by the index of refraction where $n^2 = 1+\chi^{(1)}$. In addition, $\chi^{(2)}$ and $\chi^{(4)}$ vanish in isotropic materials that exhibit inversion symmetry according to Neumann's principle.[15] Neumann's principle asserts that isotropic materials such as glass must have the same properties when viewed under different coordinate systems due to their point-group symmetry. It follows that the elements of a susceptibility tensor describing an isotropic material must be identical after any rotation or inversion of the coordinate system. The result is that $\chi^{(n)} = (-1)^{(n+1)}\chi^{(n)}$, and all even orders of the nonlinear susceptibility must be identically zero in isotropic materials or any material which exhibits inversion symmetry. With diminishing susceptibility amplitude and vanishing of both $\chi^{(2)}$ and $\chi^{(4)}$, the nonlinear susceptibility in an isotropic material can be approximated by the $\chi^{(3)}$ term in the expansion of Eq.(2.6). With these approximations, Eq. (2.9) becomes

$$\mathbf{D} \simeq \varepsilon_o(1+\boldsymbol{\chi}^{(1)}+\boldsymbol{\chi}^{(3)}\mathbf{EE})\mathbf{E} = \varepsilon\mathbf{E}+\mathbf{P}^{(3)}, \tag{2.10}$$

where $\mathbf{P}^{(3)} = \varepsilon_o\boldsymbol{\chi}^{(3)}\mathbf{EEE}$, and ε is the first-order permittivity of the material.

2.1.1. Nonlinear Wave Equation

Owing to the form of the electric displacement in Eq. (2.10), the nonlinear polarization becomes a driving term in the nonlinear wave equation. Taking the curl of Eq. (2.3) and using the identity $\nabla\times(\nabla\times\mathbf{E}) = \nabla(\nabla\bullet\mathbf{E}) - \nabla^2\mathbf{E}$ results in the equation

$$\nabla(\nabla\bullet\mathbf{E}) - \nabla^2\mathbf{E} = -\nabla\times\frac{\partial\mathbf{B}}{\partial t}. \tag{2.11}$$

Since $\mathbf{B} = \mu\mathbf{H}$ with μ defined as the magnetic permeability of the material, the right hand side of Eq. (2.11) becomes

$$-\nabla\times\frac{\partial\mathbf{B}}{\partial t} = -\mu\frac{\partial}{\partial t}(\nabla\times\mathbf{H}). \tag{2.12}$$

Inserting Eq. (2.2) and Eq. (2.1) into Eq. (2.11) and Eq. (2.12) yields

$$\nabla^2\mathbf{E} - \mu\frac{\partial^2}{\partial t^2}\mathbf{D} = \mathbf{0}. \tag{2.13}$$

where $\nabla\bullet\mathbf{E} = 0$ for plane waves in an isotropic medium. Inserting Eq. (2.10) for **D** into Eq. (2.13), the second derivative of the electric displacement adds a nonlinear driving term to the wave equation such that

$$\nabla^2\mathbf{E} - \mu\varepsilon\frac{\partial^2}{\partial t^2}\mathbf{E} = \mu\frac{\partial^2}{\partial t^2}\mathbf{P}^{(3)}(t), \tag{2.14}$$

where the electric field is assumed to be a superposition of monochromatic waves with the form

$$\mathbf{E} = \tfrac{1}{2}\sum_{\omega'}[\mathbf{E}_{\omega'}e^{-i\omega' t} + \mathbf{E}^*_{\omega'}e^{i\omega' t}], \tag{2.15}$$

and similarly

$$\mathbf{P}^{(3)}(t) = \tfrac{1}{2}\sum_{\omega'}[\mathbf{P}^{(3)}_{\omega'}e^{i\omega' t} + \mathbf{P}^{(3)*}_{\omega'}e^{-i\omega' t}]. \tag{2.16}$$

From the nonlinear wave Eq. (2.14), one can derive the change in amplitude of the electric field responding to the nonlinear polarization term $\mathbf{P}^{(3)}(t)$. The field is assumed to consist of a superposition of monochromatic plane waves propagating in the *z*-direction, and each is described by the form $\mathbf{E}_\omega = \hat{\mathbf{E}}_\omega e^{ikz}$. By equating terms that oscillate only at frequency ω, Eq. (2.14) reduces to

$$\frac{\partial^2}{\partial z^2}(\hat{\mathbf{E}}_\omega e^{ikz}) + \omega^2\mu\varepsilon\hat{\mathbf{E}}_\omega e^{ikz} = -\mu\omega^2\mathbf{P}^{(3)}_\omega. \tag{2.17}$$

The second derivative of the field with respect to *z* can be reduced using the slowly varying envelope approximation: the second derivative of the field amplitude with distance is negligible compared to the first or second derivative of the phase term[15] such that

$$\frac{\partial^2}{\partial z^2}(\hat{\mathbf{E}}_\omega e^{ikz}) \approx 2ike^{ikz}\frac{\partial}{\partial z}(\hat{\mathbf{E}}_\omega) - k^2\hat{\mathbf{E}}_\omega e^{ikz}. \tag{2.18}$$

Recognizing that $k^2 = \omega^2\mu\varepsilon$, the substitution of Eq. (2.18) into Eq. (2.17) yields the change in electric field with distance due to a nonlinear polarization,

$$\frac{\partial\hat{\mathbf{E}}_\omega}{\partial z} = \frac{i\mu\omega^2}{2k}e^{-ikz}\mathbf{P}^{(3)}_\omega. \tag{2.19}$$

This equation shows directly how the nonlinear polarization term can result in growth or attenuation of the electric field at the frequency of the induced polarization of the material.

2.1.2. Frequency Dependence

Up to this point, the frequency of the nonlinear polarization has been ignored with the exception that it will cause a change in the electric field at the same frequency as the polarization. Now we will examine the frequency dependence of $\mathbf{P}_{\omega}^{(3)}$ directly.

The nonlinear polarization is the mixture of three vector fields $\mathbf{P}^{(3)} = \varepsilon_o \boldsymbol{\chi}^{(3)} \mathbf{E}\mathbf{E}\mathbf{E}$, where $\mathbf{E}$ is any field present in the material as given by Eq. (2.15). In terms of frequency, the Fourier transform of Eq. (2.15) yields

$$\mathbf{E}(\omega) = \frac{1}{2}\sum_{\omega'}[\mathbf{E}_{\omega'}\delta(\omega-\omega') + \mathbf{E}_{\omega'}^{*}\delta(\omega+\omega')]. \tag{2.20}$$

The Fourier component of the nonlinear polarization at a single frequency denoted by ω_σ is

$$\mathbf{P}_{\omega_\sigma}^{(3)} = \varepsilon_o \sum_{\omega} K\boldsymbol{\chi}^{(3)}(-\omega_\sigma;\omega_1,\omega_2,\omega_3)\vdots\hat{\mathbf{E}}_{\omega_1}\hat{\mathbf{E}}_{\omega_2}\hat{\mathbf{E}}_{\omega_3}e^{i(k_1+k_2+k_3)z}, \tag{2.21}$$

where the frequencies ω_1, ω_2, and ω_3 each represent any of the field frequencies present in the material such that $\omega_\sigma = \omega_1 + \omega_2 + \omega_3$, K is a numerical factor that takes into account permutations of frequency arguments and factors of ½ arising from Eq. (2.20), $k_i = \frac{\omega_i n_i}{c}$, and the summation denotes the addition of all distinct sets of frequencies that add to ω_σ (this summation will be assumed in future equations). In this form, with frequency arguments noted explicitly, one can see that the resulting frequency of the nonlinear polarization is a mixture of any three frequencies present in the material. These frequency arguments can be positive, negative, or zero resulting from Eq.(2.15) and Eq. (2.20).

If the frequencies present in the material are tuned to an absorption in the material, the value of $\boldsymbol{\chi}^{(3)}(-\omega_\sigma;\omega_1,\omega_2,\omega_3)$ can grow by many orders of magnitude, known as a resonant enhancement[15]. This is the situation which brings about stimulated Brillouin scattering. With $\mathbf{P}^{(3)}_{\omega_\sigma}$ resonantly enhanced, large changes in the electric field amplitude occur at frequency ω_σ. With frequency explicitly noted, Eq. (2.19) becomes

$$\frac{\partial \hat{E}_{\omega_\sigma}}{\partial z} = \frac{i\mu\omega_\sigma^2}{2k_\sigma c^2} K \chi^{(3)}(-\omega_\sigma;\omega_1,\omega_2,\omega_3)\hat{E}_{\omega 1}\hat{E}_{\omega 2}\hat{E}_{\omega 3}e^{-i\Delta kz}, \tag{2.22}$$

where $\Delta k = k_1 + k_2 + k_3 - k_\sigma$ is the phase-matching term representing conservation of momentum, and all vector notation has been incorporated into the susceptibility, resulting in a scalar equation representing a particular arrangement of fields[15]:

$$\chi^{(3)}(-\omega_\sigma;\omega_1,\omega_2,\omega_3) = \hat{\mathbf{e}}^*_{\boldsymbol{\sigma}} \cdot \boldsymbol{\chi}^{(3)}(-\omega_\sigma;\omega_1,\omega_2,\omega_3) \vdots \hat{\mathbf{e}}_{\mathbf{1}}\hat{\mathbf{e}}_{\mathbf{2}}\hat{\mathbf{e}}_{\mathbf{3}}, \tag{2.23}$$

where $\hat{\mathbf{e}}_i$ represents the polarization vector of the electric field at frequency ω_i.

In this section, the change in the electric field at a given frequency was derived as a function of the general third-order susceptibility. In the next section, stimulated Brillouin scattering will be developed specifically.

2.2. Stimulated Brillouin Scattering

There are many field frequencies that can be generated from the 3rd-order nonlinear polarization. The main concerns are that conservation of energy, $\omega_\sigma = \omega_1 + \omega_2 + \omega_3$, and conservation of momentum, $\Delta k = k_1 + k_2 + k_3 - k_\sigma \approx 0$, are fulfilled. Typical 3rd-order effects are third harmonic generation ($\omega_\sigma = 3\omega = \omega + \omega + \omega$),

four-wave mixing ($\omega_\sigma = \omega_4 = \omega_1 + \omega_2 + \omega_3$), and self-focusing ($\omega_\sigma = \omega = \omega - \omega + \omega$). But under conditions of high field strength and resonant enhancement, the nonlinear polarization due to stimulated Brillouin scattering can increase by many orders of magnitude over other nonlinear effects.

Stimulated Brillouin scattering (SBS) is represented by the frequency set, $\omega_\sigma = \omega_b = \omega_s - \omega_s + \omega_b$, where ω_s is the frequency of the signal or SBS pump laser, and ω_b is the frequency of the scattered Stokes field, denoted with a *b* for "Brillouin." Stimulated Brillouin scattering is described as a two-photon resonant process resulting in the excitation of an acoustic or density wave in the material.[15] The signal wave excites the material from an initial energy state (g) to a final state (f) via a virtual level (v) (Fig. 1). The virtual level is represented as a linear combination of all energy levels allowed through one-photon transitions from the initial and final energy states.[17] The susceptibility is greatest when the material resonance frequency is equal to the difference between the signal frequency and the Stokes frequency:

$$\Omega_{fg} = \omega_s - \omega_b . \tag{2.24}$$

In SBS, the material resonance Ω_{fg} represents an acoustic wave frequency, and the optical frequencies of the signal and Brillouin waves are very close together, separated by a frequency on the order of 10 GHz in silicate glass.

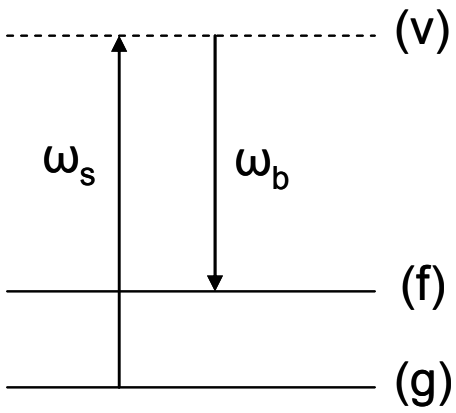

Fig. 1: Energy-level diagram depicting SBS on the two-photon transition (g) - (f).[15]

SBS can be described as the generation of an acoustic wave in the material from electrostriction.[16] The acoustic wave acts as a dynamic Bragg grating propagating at the speed of sound in the material and reflects the signal beam at the Doppler-shifted frequency ω_b. Initially, the acoustic wave exists as thermal noise in the material, and the Stokes wave generated from the interaction of the signal beam with thermal density fluctuations is known as spontaneous Brillouin scattering. After being created from noise, the backward-propagating Stokes wave beats with the signal beam to reinforce the acoustic wave, which in turn scatters more of the incident signal beam and reinforces the Stokes wave. This is the process of stimulated Brillouin scattering.

The acoustic dispersion relation

$$\Omega_B = \Omega_{fg} = | \mathbf{K}_B | v_a \tag{2.25}$$

yields an expression for the frequency of the acoustic wave in the material

where $| \mathbf{K}_B | = \frac{2\pi}{\Lambda}$, Λ is the wavelength of the density wave, and v_a is the speed of sound in the material. Due to conservation of momentum,

$$\mathbf{K}_B = \mathbf{k}_s - \mathbf{k}_b, \tag{2.26}$$

and the acoustic wave propagates in a general direction away from the signal beam as shown in Fig. 2. Together with Eq. (2.25),

$$\frac{\Omega_B}{v_a} \approx 2\frac{\omega_s n}{c}\sin\frac{\theta}{2} \tag{2.27}$$

since $\omega_s >> \Omega_B$ and $\omega_s + \omega_b \approx 2\omega_s$ [16, 18]. Therefore, the value of the Brillouin frequency shift is given by:

$$\Omega_B = 2\omega_s \frac{v_a}{c/n}\sin\frac{\theta}{2}, \tag{2.28}$$

where n is the index of refraction of the material and θ is the angle between the signal and Stokes beams as shown in Fig. 2. Eq. (2.28) shows that forward scattering is not possible under SBS since the Brillouin frequency shift drops to zero when θ equals zero.

To examine the amplification of a Stokes beam through SBS, we first look at electrostriction in general. Eq. (2.10), the equation for the electric displacement to

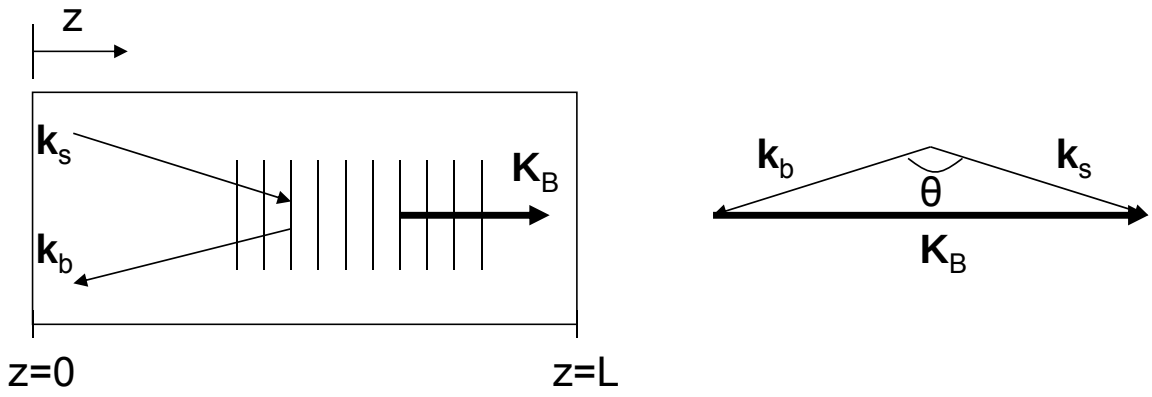

Fig. 2: Schematic representation of the SBS process via electrostriction.[16]

fourth-order in susceptibility, can be rewritten in terms of the electric permittivity and a change in the permittivity such that

$$\mathbf{D} = \varepsilon\mathbf{E} + \Delta\varepsilon\mathbf{E} \simeq \varepsilon\mathbf{E} + \mathbf{P}^{(3)}. \tag{2.29}$$

From Eq. (2.29), the third order polarization vector can be approximated as

$$\mathbf{P}^{(3)} \simeq \Delta\varepsilon\mathbf{E}. \tag{2.30}$$

The change in permittivity can be determined using thermodynamics. The differential of the permittivity with respect to the independent thermodynamic properties of temperature and density yields

$$\Delta\varepsilon = \left(\frac{\partial\varepsilon}{\partial\rho}\right)_T \Delta\rho + \left(\frac{\partial\varepsilon}{\partial T}\right)_\rho \Delta T. \tag{2.31}$$

For a low-absorption material undergoing an acousto-optic interaction, the change in permittivity with temperature is much less than the change due to density such that $\Delta T \approx 0$ [16]. The potential energy per unit volume u of a material in an electric field is given by

$$u = \varepsilon\frac{\left|\hat{E}\right|^2}{2}, \tag{2.32}$$

and the change in energy density Δu due to a change in permittivity is given by

$$\Delta u = \Delta\varepsilon\frac{\left|\hat{E}\right|^2}{2} = \left(\frac{\partial\varepsilon}{\partial\rho}\right)\Delta\rho\frac{\left|\hat{E}\right|^2}{2}. \tag{2.33}$$

The change in energy density of the material is equal to the work W performed on the material in the form of compression:

$$\Delta u = W = p_{st}\frac{\Delta V}{V} = -p_{st}\frac{\Delta\rho}{\rho}. \tag{2.34}$$

Solving for the strictive pressure p_{st},

$$p_{st} = -\gamma_e \frac{\left|\hat{E}\right|^2}{2}, \tag{2.35}$$

where $\gamma_e \equiv \rho\left(\frac{\partial \varepsilon}{\partial \rho}\right)$ is the electrostrictive constant. In general, the change in ε with respect to ρ is positive. Therefore, the strictive pressure is negative, and regions of high field strength have lower pressure.

To simplify the remainder of the derivation, assume that the signal beam is propagating in the $+z$ direction and the Stokes beam is seeded at a frequency near ω_b given by ω_b' and propagating in the $-z$ direction. The electric fields and density wave can then be described as:

$$\begin{aligned} \mathbf{E}_s(z,t) &= \hat{\mathbf{e}}_s \hat{E}_s e^{i(k_s z - \omega_s t)} \\ \mathbf{E}_{b'}(z,t) &= \hat{\mathbf{e}}_{b'} \hat{E}_{b'} e^{i(-k_b' z - \omega_b' t)} \\ \hat{\rho}(z,t) &= \rho_o + \rho(z) e^{i(K_B' z - \Omega t)} \end{aligned} \tag{2.36}$$

where $\Omega = \omega_s - \omega_b'$, and ρ_o is the mean density of the material, with the acoustic wave propagating in the $+z$ direction. For effective seeding of the Stokes beam, it is assumed that $\left|\Omega - \Omega_B\right| \lesssim \Gamma_B$, where Γ_B is the Brillouin linewidth. In Eq. (2.36), a unit vector $\hat{\mathbf{e}}_{b',s}$ was introduced to represent the polarization at frequency $\omega_{b',s}$, and the electric field amplitude at frequency $\omega_{b',s}$ is given by the scalar $\hat{E}_{b',s}$. In this geometry, the magnitude of the acoustic wave vector is the sum of the photon wave vectors $K_B' = k_s + k_b'$. Assuming the material obeys the acoustic wave equation,[16]

$$\frac{\partial^2 \hat{\rho}}{\partial t^2} - \frac{\Gamma_B}{K_B'^2} \nabla^2 \frac{\partial \hat{\rho}}{\partial t} - v_a^2 \nabla^2 \hat{\rho} = \nabla^2 p_{st}. \tag{2.37}$$

The beating of the two electric fields produces a significant material density wave. Let

$$p_{st} = -\gamma_e \frac{\left\langle \mathbf{E}^2 \right\rangle}{2} = -\gamma_e \frac{\left\langle \mathbf{E}_s \bullet \mathbf{E}_{b'}^* \right\rangle}{2}. \tag{2.38}$$

Using the slowly-varying-envelope approximation for the acoustic wave, the second derivative of the acoustic wave amplitude with respect to z is negligible. In general, the propagation of hypersonic waves is highly damped, and the propagation distance is very small compared to the distance where the electric fields vary significantly. Because of this, the first derivative of the acoustic wave amplitude with respect to z is also neglected. The acoustic wave equation (Eq. (2.37)) then reduces to:

$$-2i\Omega \frac{\partial \rho}{\partial t} + (\Omega_B^2 - \Omega^2 - i\Omega\Gamma_B)\rho = \frac{\gamma_e}{2} K_B'^2 \hat{E}_s \hat{E}_{b'}^* (\hat{\mathbf{e}}_\mathbf{s} \bullet \hat{\mathbf{e}}_{\mathbf{b}'}^*). \tag{2.39}$$

Under steady-state conditions, $\frac{\partial \rho}{\partial t} = 0$. Solving Eq. (2.39) for the acoustic wave density yields the density change under electrostriction due to two counter-propagating fields

$$\Delta\rho = \frac{\rho_o K_B'^2}{4} \left(\frac{\partial \varepsilon}{\partial \rho} \right) \frac{\hat{E}_s \hat{E}_{b'}^* e^{i(K_B z - \Omega t)} (\hat{\mathbf{e}}_\mathbf{s} \bullet \hat{\mathbf{e}}_{\mathbf{b}'}^*)}{\left(\Omega_B^2 - \Omega^2 - i\Omega\Gamma_B \right)}. \tag{2.40}$$

This change in density of the material leads to a change in permittivity using Eq. (2.31) with $\Delta T \approx 0$. From Eq.(2.30) and Eq. (2.31), the nonlinear polarization oscillating at ω_s and ω_b is given by

$$\begin{aligned} \mathbf{P}_{\omega_s}^{(3)} &= \frac{\partial \varepsilon}{\partial \rho} \Delta\rho \mathbf{E}_{\mathbf{b}'} \\ \mathbf{P}_{\omega_b'}^{(3)} &= \frac{\partial \varepsilon}{\partial \rho} \Delta\rho^* \mathbf{E}_\mathbf{s} \end{aligned} \tag{2.41}$$

and

$$\mathbf{P}_{\omega_s}^{(3)} = \frac{\rho_o K_B'^2}{8}\left(\frac{\partial\varepsilon}{\partial\rho}\right)^2 \frac{\hat{E}_s\left|\hat{E}_{b'}\right|^2 e^{i(k_s z-\omega_s t)}(\hat{\mathbf{e}}_\mathbf{s}\bullet\hat{\mathbf{e}}_{\mathbf{b}'}^*)\hat{\mathbf{e}}_{\mathbf{b}'}}{\left(\Omega_B^2-\Omega^2-i\Omega\Gamma_B\right)}$$
$$\mathbf{P}_{\omega_b'}^{(3)} = \frac{\rho_o K_B'^2}{8}\left(\frac{\partial\varepsilon}{\partial\rho}\right)^2 \frac{\left|\hat{E}_s\right|^2\hat{E}_{b'}e^{-i(k_b' z+\omega_b' t)}(\hat{\mathbf{e}}_\mathbf{s}^*\bullet\hat{\mathbf{e}}_{\mathbf{b}'})\hat{\mathbf{e}}_\mathbf{s}}{\left(\Omega_B^2-\Omega^2+i\Omega\Gamma_B\right)} \quad . \tag{2.42}$$

Using Eq. (2.19) for the change in electric field, we can now derive rate equations for the electric field amplitudes from this nonlinear polarization such that

$$\frac{\partial\hat{E}_s}{\partial z} = \frac{i\omega_s\rho_o K_B'^2}{8n_s c\varepsilon_o}\left(\frac{\partial\varepsilon}{\partial\rho}\right)^2 \frac{\hat{E}_s\left|\hat{E}_{b'}\right|^2\left|\hat{\mathbf{e}}_\mathbf{s}\bullet\hat{\mathbf{e}}_{\mathbf{b}'}^*\right|^2}{\left(\Omega_B^2-\Omega^2-i\Omega\Gamma_B\right)} \tag{2.43}$$

and

$$\frac{\partial\hat{E}_{b'}}{\partial z} = -\frac{i\omega_b'\rho_o K_B'^2}{8n_b c\varepsilon_o}\left(\frac{\partial\varepsilon}{\partial\rho}\right)^2 \frac{\hat{E}_{b'}\left|\hat{E}_s\right|^2\left|\hat{\mathbf{e}}_\mathbf{s}^*\bullet\hat{\mathbf{e}}_{\mathbf{b}'}\right|^2}{\left(\Omega_B^2-\Omega^2+i\Omega\Gamma_B\right)}, \tag{2.44}$$

where $k_\sigma = \frac{\omega_\sigma n_\sigma}{c}$ and $c^2 = \frac{1}{\varepsilon_o\mu}$. To find the gain at the Stokes frequency due to SBS, these equations must be converted from fields to irradiance. The chain rule must be used such that

$$\frac{\partial\left|\hat{E}_\sigma\right|^2}{\partial z} = \frac{\partial I_\sigma}{\partial z}\left(\frac{2}{\varepsilon_o c n_\sigma}\right) = \hat{E}_\sigma^*\frac{\partial\hat{E}_\sigma}{\partial z} + \hat{E}_\sigma\frac{\partial\hat{E}_\sigma^*}{\partial z}, \tag{2.45}$$

and the resulting rate equations are

$$\frac{\partial I_s}{\partial z} = -g_B(\Omega)I_s I_{b'}$$
$$\frac{\partial I_{b'}}{\partial z} = -g_B(\Omega)I_s I_{b'} \quad . \tag{2.46}$$

The Brillouin gain coefficient $g_B(\Omega)$ is then given by:[16]

$$g_B(\Omega) = g_o \frac{\left(\Gamma_B/2\right)^2}{\left(\Omega_B - \Omega\right)^2 + \left(\Gamma_B/2\right)^2} , \tag{2.47}$$

with

$$g_o = \frac{\omega^2 \rho_o}{\varepsilon_o^2 n v_a c^3 \Gamma_B} \left(\frac{\partial \varepsilon}{\partial \rho}\right)^2 \left|\hat{\mathbf{e}}_s \bullet \hat{\mathbf{e}}_{b'}^*\right|^2 . \tag{2.48}$$

In these equations, approximations are used such that the Brillouin-scattered Stokes frequency is approximately equal to the signal frequency, and the index of refraction is the same for both Stokes and signal beams. The equations (2.46) are the basic relations governing the growth of the Stokes beam and depletion of the signal under stimulated Brillouin scattering when the Stokes beam is seeded near the Stokes frequency. The signal depletion and Stokes growth are related to the product of the Stokes and signal irradiances.

2.3. Stimulated Brillouin Scattering Threshold

In the SBS gain equations, Eq. (2.46), the change in irradiance due to stimulated Brillouin scattering is dependent on the product of the forward propagating signal irradiance and the backward propagating Stokes irradiance. If the material is seeded with a counter-propagating beam at the Stokes frequency, then SBS takes place in the material to amplify the back-injected seed. If there is no seed, SBS can still occur. With a high signal irradiance, the thermal noise in the material provides a sufficient seed for the SBS process. Then the onset of SBS (threshold) can be described in terms of signal irradiance in a given material at which point the Stokes signal is easily distinguishable from any other reflections. When this threshold is exceeded, increases in signal irradiance are

converted to backscattered Stokes irradiance with a slope efficiency of nearly 1. The transmitted signal becomes effectively clamped near this threshold value since any additional power is efficiently converted to the backward-propagating Stokes beam.

To calculate the threshold of SBS in a fiber waveguide, Eq. (2.46) must be modified to include transmission loss of the fiber, α_s [19]:

$$\begin{aligned} \frac{\partial I_s}{\partial z} &= -g_B I_s I_b - \alpha_s I_s \\ \frac{\partial I_b}{\partial z} &= -g_B I_s I_b + \alpha_s I_b \ , \end{aligned} \tag{2.49}$$

where the subscript on α_s denotes scattering. It is a good assumption that the signal beam is non-depleted when looking for the threshold of the nonlinear effect such that $\frac{\partial I_s}{\partial z} = -\alpha_s I_s$, and the signal irradiance is

$$I_s(z) = I_s(0)e^{-\alpha_s z} . \tag{2.50}$$

Substituting this signal irradiance into Eq. (2.49) for the Stokes beam yields a first-order differential equation. For a fiber of length L, the integration results in

$$I_b(0) = I_b(L)e^{g_B I_s(0)[\frac{1}{\alpha_s}(1-e^{-\alpha_s L})]} e^{-\alpha_s L} \ , \tag{2.51}$$

where an effective length can be defined by the term in brackets:[20]

$$L_{eff} \equiv \frac{1}{\alpha_s}(1-e^{-\alpha_s L}) . \tag{2.52}$$

For the case of undepleted signal, an upper bound on the threshold can be defined as the signal power necessary to raise the Stokes power to the level of the incident signal at $z = 0$. While this is experimentally impossible, the Stokes power rises very quickly after threshold such that this point represents a slightly high estimate of threshold as

defined earlier. The Stokes beam is seeded by spontaneous scattering which is modeled by an injection of a single photon per mode at the location in the fiber where the nonlinear gain equals the natural loss of the fiber $g_B I_s(0)e^{-\alpha_s z} = \alpha_s$. The condition for threshold is then found to be[19]:

$$P_{th} \approx \frac{21A_{eff}}{g_B L_{eff}}, \tag{2.53}$$

where A_{eff} is the effective mode area of the of the confined light in a waveguide.

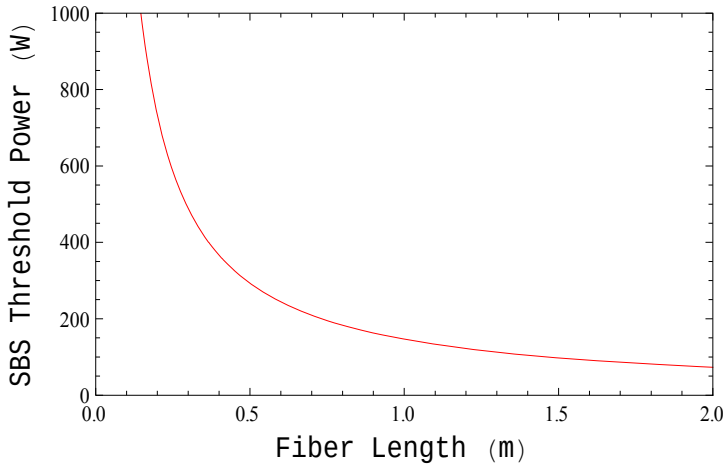

Fig. 3: SBS threshold power as a function of fiber length for a silicate fiber with a 20 μm core and 0.13 NA from Eq. (2.53).

For a cylindrical fiber, the maximum effective area supported by the fiber can be estimated from the fiber properties and wavelength being used. A typical optical fiber consists of a core with radius a and index of refraction n_{core}. This is surrounded by a region of lower index of refraction called the cladding which may consist of air or another glass or plastic material with index of refraction n_{clad}. A fiber such as this confines light incident on the end of the fiber only in a range of angles such that the light in the core is reflected inside the fiber via total internal reflection. The sine of the

maximum half-angle accepted by the fiber is called the numerical aperture (NA) and is given by

$$\sin\theta_{1/2} = NA = \sqrt{n_{core}^2 - n_{clad}^2}\ . \tag{2.54}$$

The V-number of a fiber is a normalized frequency parameter which is used to describe the number of normal modes that are relatively low loss in a fiber. The V-number is given by

$$V = k_o a(NA)\,, \tag{2.55}$$

where $k_o = 2\pi/\lambda$. It has been shown that the fundamental mode of a step-index fiber is closely approximated by a Gaussian beam with mode radius ω such that[21]

$$\omega = a\left[.65 + \frac{1.619}{V^{3/2}} + \frac{2.879}{V^6}\right]. \tag{2.56}$$

The effective area is then simply $A_{eff} = \pi\omega^2$ for a single-transverse-mode fiber.[22] However, the power contained in multimode fibers fills the fiber core more evenly than a single transverse mode. In the case of multimode fibers, the effective area is more closely approximated by the area of the fiber core.

A factor less than one, denoted by K_g here, is often used in the literature to multiply the Brillouin gain coefficient in Eq. (2.53).[23, 24] This factor is particularly important in experiments when the SBS process is seeded by an injected beam at the Stokes-shifted frequency from the back end of the fiber. The factor K_g represents the polarization overlap between the signal and Stokes seed in these experiments as given by the dot product of polarization vectors in Eq. (2.48). However, when only non-seeded SBS experiments are considered, the validity of using the polarization factor is

questionable. The Brillouin gain coefficient has been measured to be lower in fibers than in bulk silica material, and this factor with a value chosen between 0.5 and 0.67 has been used to explain the increase in SBS threshold power with no seed.[25-27] Spring *et al*.[28] measured the SBS threshold while varying the signal polarization being coupled to a polarization maintaining (PM) fiber. In this case, they measured $K_g \approx 0.5$ when the signal was launched at 45º to the polarization axes of the fiber, which varied sinusoidally to a value of 1 when the signal was aligned with the fiber polarization axes. When they tested a similar non-PM fiber, threshold was less than 10% higher than the on-axis polarization in the PM fiber, indicating the value of K_g is much closer to 1.

Inhomogeneous broadening of the Brillouin gain has been found to account for the decreased SBS gain coefficient in optical fibers. The Brillouin gain coefficient in Eq. (2.53) is reduced from the Brillouin gain at exact resonance if the acceptance angle of the fiber exceeds the backscattered angle supported by the linewidth of the acoustic phonon, Γ_B. When the fiber NA is small, $NA < \sqrt{\frac{\Gamma_B}{\Omega_B}}$, the Brillouin gain is indistinguishable from exact resonance.[29] For a silica fiber with signal wavelength of 1064 nm, this corresponds to an NA less than 0.05. For fibers with larger NA, the Brillouin scattered signal is comprised of subsets of homogeneously broadened components generated from the different angular components of the Stokes and signal modes such that[22, 30]

$$g_I(\Omega) = g_B(\Omega)\frac{\Gamma_B/2}{(\Omega_{Bo} - F_c)}\left[\tan^{-1}\left(\frac{\Omega_{Bo} - \Omega}{\Gamma_B/2}\right) - \tan^{-1}\left(\frac{F_c - \Omega}{\Gamma_B/2}\right)\right], \qquad (2.57)$$

where $F_c = \Omega_{Bo}\sqrt{1-\left(\frac{NA}{n_{core}}\right)^2}$ and $\Omega_{Bo} = \frac{2\omega_s v_a}{c/n}$. For unseeded SBS, $\Omega \approx \Omega_{Bo}$ to a good approximation, and the inhomogeneously broadened Brillouin gain can be determined purely from fiber material and characteristics. Then Eq. (2.57) reduces to

$$g_I = g_o \frac{\Gamma_B/2}{(\Omega_{Bo} - F_c)}\left[\tan^{-1}\left(\frac{F_c - \Omega_{Bo}}{\Gamma_B/2}\right)\right] \tag{2.58}$$

for unseeded SBS.

With these modifications to the parameters in Eq. (2.53), this SBS threshold prediction ("Smith model") is typically accurate only to a factor of 2. Some other factors to consider which can impact the threshold include temperature variations[31-34] due to absorption or waste heat in fiber amplifiers and lasers, dopant levels,[35] and fiber geometry fluctuations.[36, 37]

Estimating the SBS threshold in fiber amplifiers has been the subject of much research since it is seen as the main obstacle to increasing the power of single-frequency fiber amplifiers.[38-41] In low-power amplifiers, the signal power required to reach the SBS threshold is lowered in an amplifier as compared to passive fiber of the same composition. The laser gain g amplifies both the signal and the Stokes waves, which lowers the SBS threshold power as if the effective length of the fiber is longer than its physical length (see Eq. (2.53), Eq. (2.49), and Eq. (2.52) with $-\alpha_s \rightarrow g - \alpha_s$).[42, 43] However, much higher amplified powers have been achieved than were predicted by this model of SBS due to the temperature gradients present in the fiber amplifier under high-power operation.[44] The Brillouin bandwidth and frequency shift between the signal and Stokes waves is temperature dependent[31-33, 36]. With high thermal gradients

caused by end-pumping of a fiber amplifier, the Brillouin gain is effectively broadened, and SBS threshold is increased.[45]

When SBS is seeded with noise, the Smith equation (Eq. (2.53)) has typically been used to predict the SBS threshold in low-loss optical fibers. The Brillouin gain coefficient is used as a fit parameter in this equation, and other modifications have been made to this equation to accommodate gain in the fiber, broadening due to the numerical aperture of the fiber, or depolarization. For low-loss, passive fibers, it is reasonably accurate, but a more thorough model was developed to predict SBS threshold in fiber amplifiers or in fibers with high scattering losses, and is discussed in Chapter 4.

2.4. Stimulated Brillouin Scattering Phase Conjugation

Phase conjugation is the process of reflecting a wave upon itself in such a way that it behaves as the time reversal of the incident wave. In perfect phase conjugation, the wavefront of the incident wave is replicated exactly, but the propagation direction is reversed at all points. The action of a phase conjugate mirror is to conjugate the spatial and polarization properties of the incident wave. The signal beam is defined as in Eq. (2.15),

$$\mathbf{E}_s(t) = \frac{1}{2}\left[\hat{\mathbf{E}}_s e^{i(\mathbf{k}_s\cdot\mathbf{r}-\omega_s t)} + \hat{\mathbf{E}}_s^* e^{-i(\mathbf{k}_s\cdot\mathbf{r}-\omega_s t)}\right], \tag{2.59}$$

where $\hat{E}_s$ represents both the polarization and amplitude of the signal beam. The ideal phase conjugate wave is then defined as[6]

$$\mathbf{E}_c(t) = \frac{1}{2}\left[\hat{\mathbf{E}}_s^* e^{i(-\mathbf{k}_s\cdot\mathbf{r}-\omega_s t)} + \hat{\mathbf{E}}_s e^{i(\mathbf{k}_s\cdot\mathbf{r}+\omega_s t)}\right]. \tag{2.60}$$

By inspection, the phase conjugate wave is equivalent to the time reversal of the incident field $\mathbf{E}_c(t) = \mathbf{E}_s(-t)$. This conjugate beam has the time-reversed polarization of the incident beam as well, such that an incident beam with right-handed polarization will have right-handed polarization upon reflection--opposite to the case of a normal mirror.

A phase conjugate mirror can be used to compensate for aberrations induced on the beam during propagation (Fig. 4).[46] During an initial pass through an amplifier, for instance, a perfect phase front can be distorted due to inhomogeneities in the amplifying medium. Reflection by a normal mirror inverts the phase front of the incident beam and the distortion is doubled during the second pass through the aberration. However, a phase conjugate mirror does not invert the wavefront, but reverses the direction of propagation. The wavefront backs through the aberration as if time were reversed to recreate the initial perfect wavefront upon the second pass through the aberration.

The most common method for wavefront correction is through the use of adaptive optics. This method uses a wavefront sensor, a deformable mirror, and a control loop to sense and compensate distortions in the phase front of the incident light. Adaptive optics are being used in optical systems to compensate for phase distortions caused by atmospheric effects[47] and laser amplifier aberrations.[48] Highly aberrated beams present difficulties in both sensing and compensation techniques for these systems,[49] which are seeing rapid development in improved wavefront sensing techniques and control algorithms.[50-52]

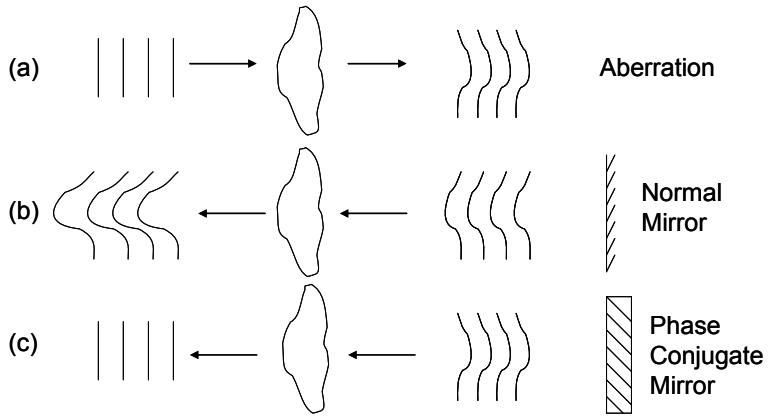

Fig. 4: Depiction of wavefront distortions (a) after passing through an aberration, (b) after reflection from a normal mirror, and (c) upon reflection from a phase conjugate mirror.

In addition to wavefront correction using adaptive optics, there are many nonlinear optical methods to achieve wavefront correction through phase conjugation such as degenerate four-wave mixing, stimulated Raman scattering, and photorefraction. With the exception of photorefractive techniques, the nonlinear optical phase conjugators have the benefit of response times in the tens of nanoseconds and do not use any signal processing or electronics in constructing the conjugate beam. Perhaps the simplest of the nonlinear phase conjugation approaches is that of SBS. SBS is characteristic of the class of self-pumped phase conjugators in that the signal beam is the only field necessary to be incident on the phase conjugate mirror. In its absolute simplest form, a signal beam is focused into a block of material. This method is referred to as the "focused geometry," and has been used with much success conjugating pulsed lasers as will be discussed in the next chapter. The focused geometry has a very high threshold, however, which makes cw phase conjugation difficult with this architecture. Until this work, cw SBS phase conjugation had not been achieved. To lower threshold to values within reach of cw systems, waveguides provide the confinement necessary to maintain high irradiance

over a long distance – two of the requirements for a low threshold as given by the threshold prediction in Eq. (2.53).

Phase conjugation via SBS was first observed in an optical waveguide by Zel'dovich in 1972 using a capillary tube filled with methane gas.[53] Through a modal analysis, Zel'dovich showed that the phase conjugate beam experiences preferential gain over all other mode combinations for the reflection of the signal. The incident field is viewed as one of many possible modes in the waveguide, which causes a rapidly fluctuating irradiance pattern in the waveguide, termed "speckle," as shown in Fig. 5. Since the Brillouin gain is proportional to the product of the irradiance of this field with that of the Stokes beam, the mode combination that experiences the highest gain is the phase conjugate of the signal beam. This can be shown starting from Eq. (2.49) with explicit radial ($r_\perp$) and longitudinal (z) dependence,[54]

$$\begin{aligned}\frac{\partial I_s(r_\perp,z)}{\partial z} &= -g_I(r_\perp)I_s(r_\perp,z)I_b(r_\perp,z)-\alpha_s I_s(r_\perp,z)\\ \frac{\partial I_b(r_\perp,z)}{\partial z} &= -g_I(r_\perp)I_s(r_\perp,z)I_b(r_\perp,z)+\alpha_s I_b(r_\perp,z).\end{aligned} \tag{2.61}$$

Integration of the equations over the radial direction transforms the equations into functions of power such that[55]

$$\begin{aligned}\frac{\partial P_s(z)}{\partial z} &= -g_{eff}(z)P_s(z)P_b(z)-\alpha_s P_s(z)\\ \frac{\partial P_b(z)}{\partial z} &= -g_{eff}(z)P_s(z)P_b(z)+\alpha_s P_b(z)\ ,\end{aligned} \tag{2.62}$$

where the effective Brillouin gain coefficient is given by

$$g_{eff}(z) = g_I \frac{\int G(r_\perp)I_s(r_\perp,z)I_b(r_\perp,z)dr_\perp}{P_s(z)P_b(z)}. \tag{2.63}$$

In Eq. (2.63), any radial dependence on the Brillouin gain coefficient is represented by the normalized variable $G(r_\perp)$, which is set equal to one for step-index fiber. According to this equation, the effective gain is the highest for the Stokes modes which exhibit the best overlap with the signal, which favors the phase conjugate beam when $G(r_\perp)$ is a constant. This analysis is applicable to any waveguide which has a homogeneous core such as a glass fiber with a step-index core.

SBS in a waveguide does not generate a perfect phase conjugate beam as defined in Eq. (2.60). As a result of the interaction with a phonon wave in the material, the Stokes beam is shifted in frequency on the order of 10 GHz. This small frequency shift leads to a limitation in the length of waveguide that can be used to generate a phase conjugate beam. Since SBS phase conjugation derives from the selected gain of the conjugate mode, the Stokes beam must overlap the signal wave path exactly to

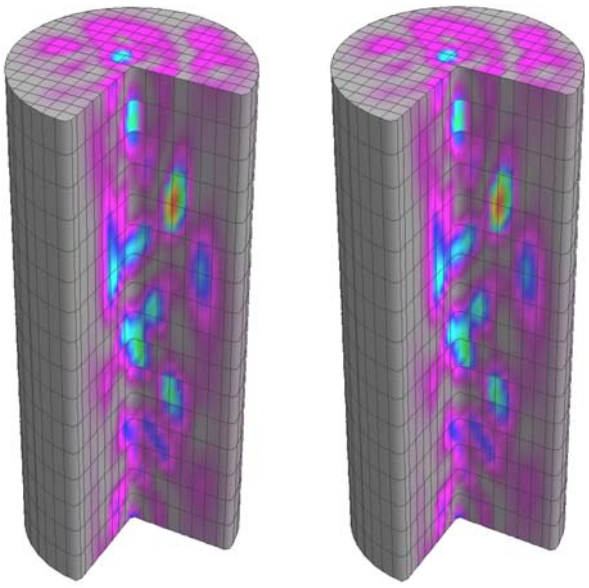

Fig. 5: (a) The irradiance pattern of the signal inside a 1 mm segment of step-index, multimode fiber. The diagram in (b) shows a phase conjugate beam at the Stokes-shifted frequency for the same segment of fiber.[56]

experience the gain from the speckle pattern generated from the signal wave. The frequency shift of the Stokes beam thus limits the interaction length for good phase conjugation. A consequence of this is higher power signals are needed to reach the SBS threshold power, which is inversely related to waveguide length. The maximum interaction length that can be used to achieve a specified quality of phase conjugation was modeled by Zel'dovich in 1977[57] and similarly by Hellwarth in 1978[29] such that

$$L \le \frac{6\sqrt{(1-F)}A_{eff}}{N_w \Delta\lambda}, \tag{2.64}$$

where N_w is the number of excited waveguide modes, $\Delta\lambda$ is the wavelength difference between Stokes and signal beams, and F is the "fidelity" of the conjugated beam. The fidelity is the fraction of the Stokes beam that is the spatial phase conjugate of the signal beam. A perfectly phase-conjugated beam has a fidelity of 1. Approximating $N_w \approx \frac{V^2}{2} = \frac{\left(k_o a\left(NA\right)\right)^2}{2}$ for multimode step-index fibers,[58] Eq. (2.64) was later given by[59]

$$L \le \frac{6\sqrt{1-F}c}{\Omega_B (NA)^2}. \tag{2.65}$$

where the Stokes shift is represented by angular frequency $\Omega_B = 2\pi c \frac{\Delta\lambda}{\lambda^2}$. Similarly, Zel'dovich' model results in a length limitation of

$$L \le \frac{3\sqrt{1-F}Mc}{n\Omega_B NA^2} \tag{2.66}$$

where n is the index of refraction of the core and M is a scalar used to account for the spatial pump irradiance pattern such as Gaussian ($M = 2.8$) or a flat-top beam ($M = 12$).

The models nearly converge in the case of a Gaussian pump. These models were derived analytically using the approximation of near-perfect fidelity. The non-conjugated fraction of the Stokes beam was assumed to be small such that only a few terms in the Taylor series were kept. As a result, these models lose validity as the fidelity declines. Another approach described the maximum interaction length as a function of phase error $\Delta\phi$ between the Stokes and signal beams by examining the modal dispersion between normal modes of a fiber waveguide. This method resulted in a maximum length of[55]

$$L \le \frac{2n_{core}c\Delta\phi}{\Omega_B \left(NA\right)^2}. \tag{2.67}$$

These methods predict a maximum interaction length of 14 cm to produce very good phase conjugation (fidelity of 0.9 or wavefront error less than $\lambda/10$) from a silicate fiber that supports ~100 modes (25 μm core diameter with 0.2 NA). As discussed in the next chapter, fibers up to 25 m long have been shown to achieve good phase conjugation using pulsed lasers.[60, 61] The discrepancy is reduced since the effective length of the interaction may be limited by the coherence length of the signal laser as in Eq. (3.2).[62]

However, the result of this dissertation discovered experimentally that these analytic models underestimate the length of step-index fiber that can be used to generate a good fidelity phase conjugate beam by an order of magnitude. In addition, the new experimental results of this work guided a numerical model that solved the differential equations governing SBS in a fiber-optic waveguide to calculate the fidelity.[63]

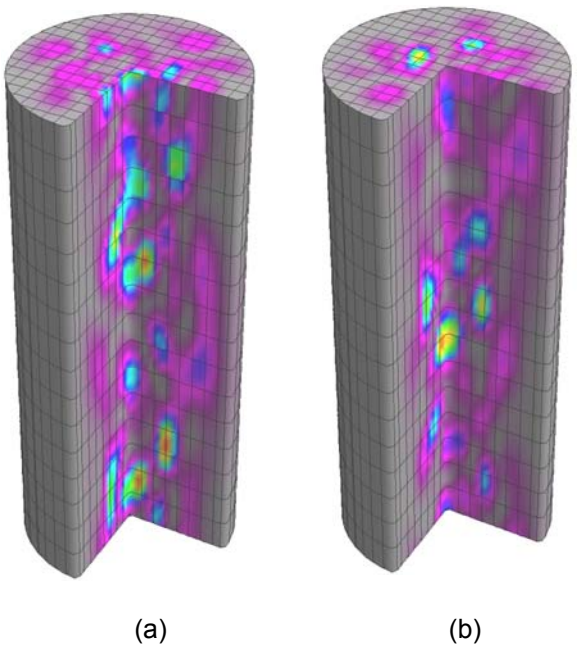

Fig. 6: The irradiance pattern inside a 1 mm segments of step-index, multimode fiber after propagating 1 km (a) for the signal beam and (b) for the phase conjugate beam.[56]

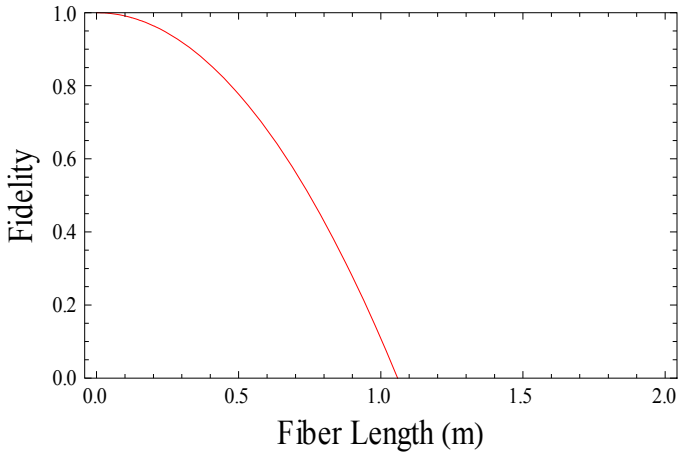

Fig. 7: Fidelity prediction as a function of fiber length from Eq. (2.65).

The previous discussion on SBS phase conjugation fidelity does not apply to a waveguide with a non-uniform core such as a graded-index fiber. A graded-index fiber has an index of refraction that decreases from the center of the fiber to the cladding in a parabolic profile, and is common in telecommunications applications because the

dispersion is reduced over step-index fibers. Due to the reduction in modal dispersion, the previous discussion would lead one to believe that longer lengths of graded-index fiber could be used to create high fidelity phase conjugation. Unfortunately, this is not the case. In this type of fiber, the fundamental Stokes mode is usually favored over all other fiber modes by a small margin and experiences the highest SBS gain.[55, 64] Both the modal structure and the dopant distribution in the fiber used to create the index variation serve to increase the SBS gain in the center of the core. In Eq. (2.63), $G(r_{\perp})$ is not a constant, and the fundamental Stokes mode is favored through gain guiding.[55] Instead of a phase conjugate, SBS in a graded-index fiber causes a Stokes beam primarily in the fundamental mode regardless of the modes excited by the signal beam.[64, 65]

In summary, phase conjugation is achievable through SBS in a step-index optical fiber provided the length is short enough. This length limitation was calculated with approximations for high fidelity in Eq. (2.65) and Eq. (2.66). However, the power needed to achieve SBS threshold is inversely proportional to the fiber length as given by Eq. (2.53). These considerations frame this work.

3. Literature Review

In this section, experimental observations, techniques, and accomplishments will be reviewed that pertain to SBS phase conjugation in optical fibers. Most of the work that has been conducted has focused on pulsed laser sources to generate the high intensities needed to exceed the SBS threshold. A progression towards phase conjugation at lower intensities will be shown to the level where this work's achievement of cw phase conjugation becomes feasible.

The earliest work, including the discovery of the effect, used gas-filled waveguides. Many pulsed lasers have been conjugated by simply focusing into a cell filled with a liquid or gas, or into a block of solid material. The interaction length is small in these devices, leading to a large pulse energy requirement. Multiple cells were employed to conjugate lower energy pulsed systems. A large amount of work has also been done using pulsed lasers with solid waveguides as the SBS material. In these cases, the coherence length of the pulsed laser typically limits the effective length of the Brillouin scattering interaction. Long coherence length lasers with long fiber SBS media have been used to reduce threshold energy, but as indicated at the end of Chapter 2, this has produced beam cleanup or the loss of phase conjugation fidelity. The SBS threshold using cw signal lasers has been recently modeled in fiber amplifiers by several authors since it is a limiting factor in high-power, single-frequency fiber amplifiers. The SBS threshold has also been studied in newly developed glass fiber materials such as tellurite and chalcogenide glass fiber for the development of fast optical switches. Those experiments demonstrate the promise of using fiber amplifiers, chalcogenide glass, or tellurite glass fibers as the SBS media for cw phase conjugation.

3.1. Initial Observation of SBS Phase Conjugation

The earliest example of phase conjugation was performed by Zel'dovich *et al.*in 1972 using a large aperture glass square waveguide placed in a cell of methane gas at 125 atm[53]. The experimental apparatus shown in Fig. 8 is one of many methods used to measure phase conjugation fidelity and will be described in detail here. A pulsed laser was used to generate 110 ns pulses with a peak power of 1.3 MW. The pulses were passed through a 6 mm x 6 mm aperture and an aberrator made from etched glass and focused into the methane cell with a 1 m focal length lens. Stimulated Brillouin scattering was observed with 25% reflectivity, and the divergence of the light was measured before the etched glass (at C1) and after the etched glass (not shown) to examine the amount of distortion the etched glass caused. The Stokes beam reflected from the cell was then measured before (not shown) and after the etched glass (at C2) to measure the beam quality improvement caused by the second pass through the aberration. A perfect phase conjugate beam will recreate the incident beam divergence after the second pass through the aberration. Comparing the final divergence to the initial beam divergence (C2/C1 in Fig. 8) therefore gives a measure of fidelity. The final corrected divergence is also compared to the final divergence observed using a standard mirror instead of the SBS cell to reflect the incident beam twice through the aberration. In Zel'dovich' experiment, the divergence of the signal beam was measured at 0.14 mrad x 1.3 mrad before passing through the etched glass. The divergence immediately after the etched glass had degraded to 3.5 mrad. The divergence after being reflected in the SBS cell and passing through the etched glass twice was nearly identical to that of the incident beam. However, replacing the SBS mirror with a standard mirror resulted in a

divergence of 6.5 mrad – nearly twice the single-pass divergence through the etched glass.

This successful demonstration of SBS phase conjugation was quickly followed by a similar experiment by Nosach *et al.,*[66] which was the first experiment to show that phase conjugation could correct for aberrations induced by an amplifier. They used a ruby laser amplifier as the aberrator with a 3 mm diameter capillary tube 1 m in length filled with carbon disulfide to generate SBS. In one pass, the amplifier caused the divergence to increase from 0.13 mrad to 2.5 mrad. The SBS cell reflected 60% of the incident amplified light, and after a second pass through the amplifier, the resulting beam had a divergence of 0.15 mrad. These results were confirmed by duplicating the experiment at Hughes Research Laboratories in 1978 using 17 ns pulsed laser [67]. These early experiments generated phase conjugate beams using short pulses with greater than 1 MW peak power.

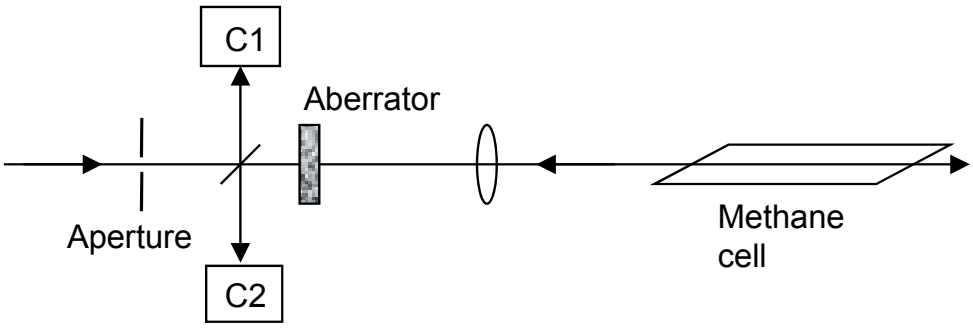

Fig. 8: Experimental apparatus for the earlies observation of SBS phase conjugation. Cameras 1 and 2 measure the divergence of the signal and Stokes beams, respectively.

3.2. Focused Cells and Capillary Tubes

Following this work, a large number of experiments were carried out by simply focusing pulsed laser light into a cell containing pressurized gases or liquids as the phase conjugate media.[6, 46] Pulsed lasers were always used due to the high powers necessary to exceed the SBS threshold in the focused cell geometry. For comparison, the Brillouin gain coefficient and phonon lifetimes measured in some of the materials used is listed in Table 1.[46, 68-70]

As a demonstration of the capabilities of an SBS phase conjugator, Eichler used an SBS cell in 1995 to improve the beam quality of a 2-pass rod amplifier operating at 100 W average power. The beam was improved from 2 times the diffraction limit to 1.2 times the diffraction limit by reflecting from a phase conjugate mirror instead of a planar mirror.[71] The oscillator produced a beam that was 1.2 times the diffraction limit, and the phase conjugating mirror corrected amplifier aberrations such that the resulting output beam had nearly the same quality as the oscillator. The pulse width was 70 ns, and the SBS cell was filled with CS_2 liquid. The signal beam was reflected through a flash lamp pumped Nd:YALO rod using a polarizing beamsplitter and a Faraday rotator. The beam

Table 1: Brillouin gain coefficients and phonon lifetimes measured in selected materials. [46, 68-70]

Material	g_b (10^{-11} m/W)	τ_p (ns)
CH_4 (100 atm)	65	17
N_2 (135 atm)	30	22
SF_6 (22 atm)	35	24
Xe (39 atm)	44	30
CS_2	130	4.6
Acetone	20	1.9
CCl_4	6	0.5
SiO_2	5	4.3

was focused into the SBS cell using a 2 m focal length lens, and the maximum reflectivity of the SBS cell was measured at 60% at an incident irradiance approximately 7 times above the SBS threshold. After reflection in the SBS cell, the beam passed through the amplifier and Faraday rotator a second time before outcoupling at the polarizing beamsplitter. The thermal lens effect is a main problem in rod amplifiers. When operating at high powers, the lens focal length varies with pump power.[72] As a demonstration of the phase conjugate properties of the SBS cell, the beam quality of the laser output was found to be 1.2 times the diffraction limit despite a range in pump power from 2 to 8 kW, with corresponding average output powers from
2 W to 102 W.

SBS phase conjugation has also been used to increase the pulse power and beam quality from zig-zag slab architectures.[73-75] In zig-zag slab ampifiers, the signal beam is incident on the edge of a typically Brewster-cut slab of solid gain material such as Nd:YAG pumped on its large face with flash lamps or laser diodes. The signal reflects multiple times inside the slab via TIR. The optical path averages out much of the thermal lens experienced with bulk solid-state amplifiers. Using a single flash lamp-pumped slab in a 4-pass geometry with a phase-conjugate reflection, Offerhaus generated 20 W average power at the diffraction limit in 25 ns pulses at 400 Hz. To generate the phase conjugate beam, two cells filled with Freon-113 were used in succession termed an "oscillator-amplifier" SBS configuration. After two passes through the amplifier, the signal was focused through a 500 mm cell ("SBS amplifier") with a 200 mm focal length lens. Any residual transmitted beam was then focused through a 100 mm cell

("oscillator") with a 50 mm lens to increase the reflectivity of the SBS reflection, which was reported to be 60%.

The double-SBS cell in a focused geometry used by Offerhaus lowers the power required to achieve SBS. It was originally developed by Crofts *et al.*[76] with the more accurate name of "generator-amplifier." SBS threshold depends on the cross-sectional area of the beam divided by the effective length as in Eq. (2.53). The effective length in a focused geometry is typically taken as two to three times the Rayleigh range of the beam.[77] It is interesting to note that if the area is approximated as the cross-section of the beam at the focus, the quotient reduces to:

$$\frac{A_{eff}}{L_{eff}} \approx \frac{\pi w_o^2}{2\pi n w_o^2 / \lambda} = \frac{\lambda}{2n}, \tag{3.1}$$

which is independent of spot size and therefore independent of focusing optic used as long as the cell is longer than the effective length. A reduction in SBS threshold arises from the existence of the second cell and not the power of the lens used. In fact, Duignan *et al.* reported a reduction in SBS threshold of a factor of up to 3.4 by using a Herriott cell to generate an SBS mirror consisting of effectively 24 cells.[78] 1.7 μs pulses from an HF laser at 500 mJ per pulse were focused and refocused into a single cell filled with high pressure xenon. The beam was refocused through the 50 cm cell up to 24 times by 100 cm focal length mirrors. They measured ~85% conjugation fidelity with this arrangement with peak powers at ~0.3 MW.

Dane *et al.* at Lawrence Livermore National Laboratory used SBS phase conjugation to clean up aberrations in an 8-pass zig-zag slab laser using flash lamp-pumped Nd:glass amplifiers.[74] The SBS mirror consisted of a double-cell of CCl_4. After 4 passes through the amplifier, the signal beam was collimated through a 33 cm cell

with a beam diameter such that this SBS amplifier cell is operating at 1-2 times SBS threshold. Then the beam was focused into a second "oscillator" cell using a 14 cm focal length lens. At low powers, the oscillator cell performs a majority of the conjugation. As power is increased, the amplifier cell becomes more active and reduces the irradiance in the oscillator cell. The purpose of the two-cell architecture in this case is to enable a broad peak power range to be conjugated without concern for competing processes such as stimulated Raman scattering, self-focusing, or material breakdown. Using this arrangement, they achieved 88% reflectivity. They note that to avoid transient effects or fidelity fluctuations, it is important when using pulsed systems to ensure the rise time of the leading edge of the pulse is long compared to the phonon decay time of the Brillouin medium. Ultimately, their laser system produced over 25 J/pulse in 14 ns pulses, 6 Hz PRF, in a beam 1.25 times the diffraction limit for an average power over 150 W.

While SBS in focused cells has been shown to work well with such high powers typically found in flash lamp-pumped, short-pulse lasers as noted above, the SBS threshold is prohibitive for most cw lasers. Some success at lowering the SBS threshold in focused geometries was achieved by using ring cavities or SBS-cell resonators to create a longer path length through the material.[79, 80] Using an amplifying medium as the SBS cell has also been used to lower threshold by increasing the effective length as shown in Section 2.3.[81] However, as the peak power incident on the cell reduces toward threshold levels, the fidelity of focused-cell SBS phase conjugation decreases. Near threshold, only the most intense portions of the focused beam in the cell are conjugated.[82] In addition, the aberrations in the incident beam can cause such a large transverse profile at the single focus that the conjugated components of the beam are

uncorrelated.[83] To reduce the SBS threshold for lower peak power lasers, waveguides were employed to maintain high intensities for longer effective lengths.

Gas or liquid-filled capillary tubes have been used to reduce the SBS threshold in pulsed laser systems to as low as 40 W peak power. Liquids have typically been chosen as the SBS medium since the higher index of refraction than the capillary tube results in a high NA, which results in better guiding as compared to gas-filled waveguides. As reported by Jones *et al*.,[84, 85] a benzene-filled capillary tube with a diameter of 60 μm was used to lower SBS threshold to 130 W peak power. Jones achieved 40% reflectivity at an even lower peak power of 70 W using a 500 ns pulsed laser and a CS_2-filled capillary tube that was 2 m long with a 100 μm inner diameter. In separate experiments with CS_2-filled waveguides, Jones obtained up to 50% reflectivity and 80% conjugation fidelity. The lowest SBS threshold among pulsed laser experiments with liquid or gas-filled waveguides was obtained in a tapered waveguide filled with CS_2.[86] The diameter of the waveguide was rapidly tapered from 0.5 mm to 10 μm for an additional 30 cm. An SBS threshold value of 40 W peak power was measured for this waveguide using 15 ns pulses with a reflectivity of ~60%, but fidelity measurements were not reported. In experiments such as this, the small waveguide acts as an SBS seed. The two-waveguide system may begin to act as an amplifier for the seed instead of a phase conjugate mirror, which degrades the fidelity.

3.3. Glass Fiber Optics

SBS phase conjugation has been achieved at low peak powers using pulsed lasers with silicate-fiber phase conjugators. The threshold reduction with fiber length has enticed some research in cw phase conjugation using silicate fibers, but the

implementation has not been successful until this research effort. Phase conjugation has also been explored using pulsed lasers with silicate-fiber amplifiers as the SBS media, which resulted in peak power SBS thresholds of less than 10 W, well within the range of cw lasers. Most research related to SBS in fiber amplifiers was aimed at increasing the power-limiting threshold of SBS. Recently, new glass fibers have been manufactured commercially such as tellurite and chalcogenide (As_2Se_3) glasses, which have been found to exhibit a very high Brillouin gain coefficient. While the threshold of SBS has been explored in these new glass fibers, phase conjugation experiments have not been performed. Chalcogenide glass, tellurite glass, and silicate-fiber amplifiers represent some of the most promising materials for cw phase conjugation via SBS.

3.3.1. Silicate Fiber

One of the earliest examples of phase conjugation in multimode silicate fibers was done by Kuzin in 1985.[60] Using a 7 m multimode fiber (30 μm diameter, 0.12 NA) and a pulsed laser with pulse duration of 500 ns, they measured SBS threshold at 50 W and achieved ~80% reflectivity at higher powers. The fidelity was reportedly near 1. They tested a fiber with a length of 130 m and encountered depolarization in the Stokes beam. The SBS threshold was measured at ~10 W, and power reflectivity approached 100% with incident peak powers of 500 W. From these results, they concluded the length of the fiber lowered SBS threshold, but the fidelity was limited by depolarization as high as 50% in the fiber at the longer length of fiber. They did note that analysis of the Stokes beam with only the same polarization as the signal exhibited high fidelity conjugation.

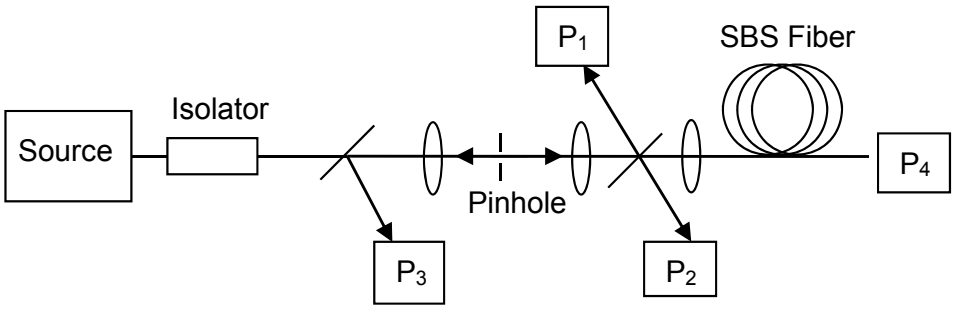

Fig. 9: Apparatus used by Kuzin to measure phase conjugation fidelity with an in-line pinhole.[60]

The method used by Kuzin to measure fidelity employs an in-line pinhole through which the incident beam is sent prior to being coupled into the fiber.[60] The SBS fiber itself acts as an aberrating medium, and the pinhole diameter was chosen "so that only that fraction of the Stokes wave which was the phase-conjugate replica of the laser beam could pass through in the reverse direction." The fidelity was measured as the ratio of Stokes power that transmits through the pinhole to the total Stokes power, $F = P_3/P_2$. Kuzin notes that the error in the Stokes power measurements was 20%, but claims total transmission through the pinhole and near perfect phase conjugation using the 7 m fiber.

Kuzin's experiment, performed with a pulsed laser, is one case where fibers 100 m or longer were shown to reduce the fidelity of phase conjugation attributed to depolarization. However, the high fidelity obtained in this pulsed laser experiment with 7 m of fiber suggests fibers much longer than predicted by Eq. (2.65) and Eq. (2.67) may produce good fidelity phase conjugation. In fact, Vasil'ev *et al.* employed a 25 m fiber as a phase conjugate mirror to effectively remove amplifier-induced aberrations in pulsed laser system.[61]

The coherence lengths of the pulsed lasers used in Kuzin and Vasil'ev's experiments were not reported. The work of Eichler would later show the effective

length of the SBS interaction in the fiber is reduced based on the coherence length of the signal laser.[62] Eichler used a pulsed laser to study SBS phase conjugation in silicate fibers with 200 μm diameter, step-index cores. The signal laser produced 30 ns pulses at 1064 nm wavelength, and the coherence length of the laser was varied from 20+/-10 cm to 80+/-30 cm. Fiber length was varied up to 10 m to study reflectivity, fidelity, and threshold of SBS phase conjugation. A schematic of the apparatus is shown in Fig. 10.

Eichler found that the reflectivity and fidelity achieved through SBS in the fiber behaved as if the length of fiber were only ~1 m even when the fiber was physically longer. After conducting measurements of fidelity, reflectivity, and threshold power as a function of both fiber length and laser coherence length, he defined an SBS effective length limited by the signal laser coherence length as

$$\frac{1}{L_{eff}} = \frac{1}{L_{coh}^{s}} + \frac{1}{L_{fiber}}, \tag{3.2}$$

where L_{coh}^{s} is the coherence length of the signal laser. Using a 4.1 m fiber, the threshold was found at 17 kW peak power and reflectivity reached 50% of the incident power.

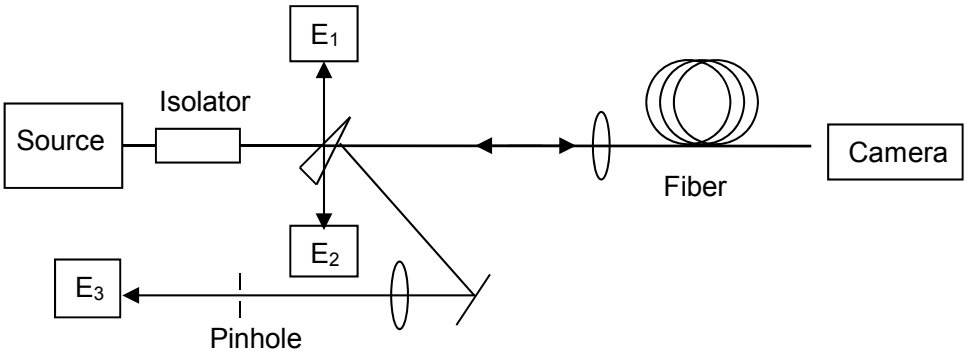

Fig. 10: Apparatus used to measure fidelity and reflectivity from a fiber phase conjugate mirror.[62]

The result of Eichler's work shows good fidelity phase conjugation can be achieved using effective lengths of a few meters of fiber. Eichler's experiments are in reasonable agreement (within a factor of 2) with the fiber length predicted by Eq. (2.65) for good fidelity conjugation when the coherence length of the signal laser is taken into account. Due to the short coherence length of the signal laser, the expected decrease in fidelity with fiber length was not explored during these experiments even though the fiber length was increased to 10 m. Eichler's conclusions regarding the effective fiber length were confirmed in larger diameter fibers (0.4 mm to 1.0 mm diameters) by Pashinin *et al.* using a 10 cm coherence length signal laser and fibers up to 20 m long.[87] Yoshida published similar research using 10 m fibers of 200 μm diameter with a pulsed laser of 1.2 m coherence length.[88] Yoshida's laser had short pulses of only 10 ns and experienced damaging effects from the transient effects of SBS in short pulses approaching the phonon lifetime of the material. Eichler later reduced SBS threshold powers to 300 W peak power using a 25 μm diameter silicate fiber that was 10 m long with an NA of 0.22, but fidelity was not reported.[89, 90]

The technique Eichler used to measure fidelity is known as the power-in-the-bucket technique. First, the signal beam transmission, T, is measured through a pinhole at the focus of a lens, measured at E_1 in Fig. 10 above. The Stokes beam is focused through a similar pinhole by a similar lens as shown in Fig. 10, and the energy transmitted, E_3, is recorded. The total energy in the Stokes beam is also recorded, E_2. The fidelity is then given by the ratio of the Stokes energy transmitted through the pinhole to the product of the total Stokes energy and the incident beam transmission,

$F = \frac{E_3}{E_2 T}$. The reflectivity is simply the Stokes energy divided by the incident energy, $R = E_2 / E_1$.

Several high-pulse-power laser systems have been constructed using multimode silicate fibers as phase conjugate mirrors. In 1985, Vasil'ev *et al*. used a multimode fiber as the phase conjugating medium in a four-pass Nd:glass amplifier[61]. The fiber had a core diameter of 50 μm and a length of 25 m. A single pass of the amplifier typically aberrated the single-mode beam to 15 times the diffraction limit. When the fiber phase conjugator was used, the output of the amplifiers matched the divergence of the source beam, amplified by an overall gain of ~300. Eichler's research team realized similar results with a 4-pass MOPA system. By using a multimode fiber as the phase-conjugate mirror, they increased power from 84 W to 124 W with a slight improvement of beam quality to 2.2 times the diffraction limit.[91] In a different arrangement, two amplifier channels were separately phase-conjugated and polarization combined to form a total of 315 W average power in 120 ns pulses with 2.6 times the diffraction limit in beam quality.[92] The SBS fiber was 2 m long with a 200 μm core diameter. They noted that the phase-conjugate reflection from each amplifier leg automatically superimposes the beams spatially at the polarizing beamsplitter (Fig. 11).

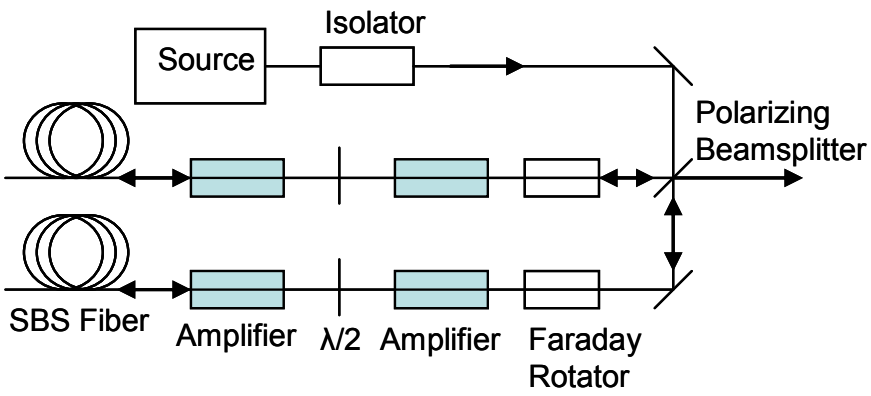

Fig. 11: Two-channel, polarization-combined 315 W MOPA with multimode fiber phase conjugating mirrors.

In attempting to lower the SBS threshold even further while maintaining high conjugate fidelity, Heuer *et al.* applied a two-cell oscillator/amplifier approach to fiber-optic phase conjugators.[93] In this method, a 45 cm-long, 100 μm-core fiber was tapered over a length of 5 cm into a 20 μm diameter fiber that was 50 cm long. The narrow section of fiber served to decrease the threshold by a factor of 6.6 times lower than if just the 100 μm-core fiber were used with a full length of 1 m. The reported fidelity was above 0.95 with a maximum reflectivity of 92%. However, the fidelity was not reported for energy levels less than 5 times above SBS threshold. Lower pulse-power operation approaching SBS threshold may cause a larger portion of the incident signal beam to be conjugated in the narrow portion of the tapered fiber. This may decrease the fidelity since the narrow fiber portion cannot accept the full structure of the signal beam, and therefore cannot conjugate the full beam. This is similar to seeded SBS which will be discussed next.

Providing feedback into the SBS medium at the Stokes-shifted frequency can also lower or even remove the SBS threshold. The feedback provides a higher power seed

than the usual noise source that typically generates SBS.[16] However, these methods tend to degrade the fidelity of phase conjugation. Enclosing the fiber in a Fabry-Perot resonator leads to a lower threshold but also results in periodic power spikes at the roundtrip time of the cavity until the signal power is increased to many times above threshold.[94, 95] The disappearance of the spiking at roundtrip times could be due to a large portion of the incident power being converted to Stokes power in a single pass of the material without using the cavity feedback. A second method of feedback is the loop scheme or ring cavity pictured in Fig. 12. This method reduced SBS threshold by a factor of 1.6 in an experiment using a 30 ns pulsed laser and a 1 m fiber with a 50 μm diameter.[96] The conjugation fidelity was not measured in this test, but very short pulses in the Stokes beam with a periodicity of the roundtrip time in the loop were observed. In a separate use of the ring resonator, a much longer fiber of 4.4 km was placed in a ring cavity which reduced the SBS threshold by 25%.[65] While the temporal profile of the Stokes beam was studied in these research efforts involving feedback, the conjugation fidelity was absent. The ability of feedback cavities to provide high fidelity conjugation is questionable and has not been demonstrated.

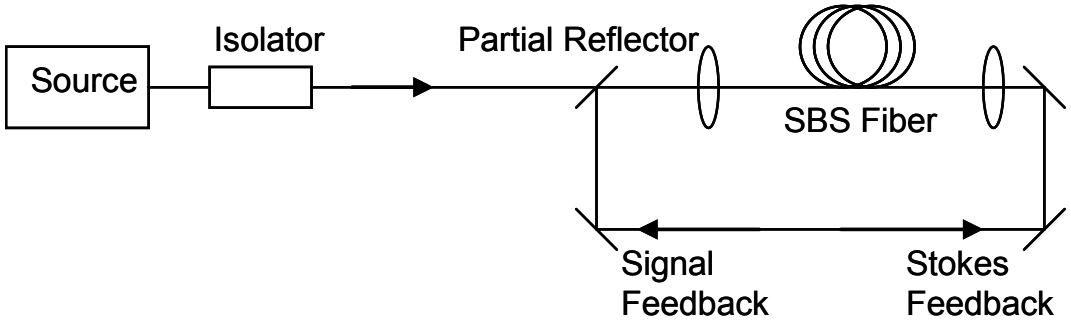

Fig. 12: Loop or ring cavity used to reduce SBS threshold.[96]

Since the threshold of SBS is reduced as the length of fiber increases (see Fig. 3), it is important to review some published results seeking SBS phase conjugation and beam cleanup in long fibers on the order of 1 km or more. When a signal beam is launched into a long, multimode fiber in such a way as to excite nearly all the supported modes of the fiber, the backward propagating Stokes beam may emerge in only the LP_{11} or fundamental mode.[64, 65, 97-99] The effect is known as SBS beam cleanup, as mentioned earlier in Section 2.4. This is different from phase conjugation since a phase conjugate beam would be as distorted as the incident signal when reflected by the fiber and only experience beam cleanup upon a second pass through the original aberration. Bruesselbach first observed beam cleanup using fiber lengths of 2.2 km and 3.3 km that supported several hundred modes. Rodgers demonstrated beam cleanup using a few-mode, 4.4 km graded-index fiber operated in a ring geometry. Russell *et al*. used a 4.4 km graded-index fiber with a 50 μm core for beam cleanup. The Stokes beam emerged from the fiber with a beam quality near the diffraction limit while the signal beam was measured at 18 times the diffraction limit. To eliminate the possibility of spatial filtering, Russell measured the coupled beam quality after 2 m propagation in the fiber and found it to be 9 times the diffraction limit. Grime carried out similar experiments confirming beam cleanup in long graded-index fiber with larger diameter cores of 62.5 μm and 100 μm. The results of these experiments showed that beam cleanup will occur as opposed to phase conjugation in long graded-index fibers, as discussed in Section 2.4.

In both modeling and pulsed experiments, Lombard explored graded-index and step-index fibers to find conditions for phase conjugation and beam cleanup.[64] In the step-index fiber model, the Brillouin gain was found to be uniform across all supported

fiber modes, which is necessary for accurate phase conjugation. However, the Brillouin gain for lower-order modes in a graded-index fiber was nearly twice the gain than the higher-order modes, which leads to beam cleanup. In experiments, Lombard achieved "good quality" phase conjugation using a 2 m step-index fiber with a 50 μm core diameter, but "bad quality" phase conjugation using a 2 m graded-index fiber with 62.5 μm core and NA of 0.27. Beam cleanup was observed using multimode graded-index fiber longer than 30 m, and the Stokes beam emitted in the LP_{11} or LP_{01} modes depending on signal coupling. In this case, the input beam had a pulse duration of 1 μs and was 6.5 times the diffraction limit while the Stokes beam was 1.2 times the diffraction limit. Lombard's investigations using a 1 km length of the step-index fiber did not yield beam cleanup nor phase conjugation.

In contrast to the theory and experiments regarding graded-index fibers presented above, there are several reports of cw phase conjugation in long, multimode, graded-index fibers.[95, 100-105] The experiments typically used several kilometers of 50 μm-core, graded-index fiber to generate SBS. The fidelity is measured by comparing beams as they transmit an aberration, reflect from the fiber via SBS, and re-transmit the same aberration. The comparisons are done using pictures of beam irradiance, the measured beam divergence as done by Zel'dovich, a power-in-the-bucket technique as done by Eichler, or an M^2 measurement. In one experiment, a power-in-the-bucket technique was used to measure fidelity and phase conjugation was claimed with a fidelity of 0.3. Since beam cleanup can produce a Stokes beam at the diffraction limit, divergence measurements, beam quality, and power-in-the-bucket measurements can be deceiving. Using these techniques, low fidelity measurements less than 0.5 are especially

ambiguous. The most-likely explanation for their observations is beam cleanup, and these papers demonstrate the care that must be taken to distinguish phase conjugation from beam cleanup when measuring fidelity. In this work, the in-line pinhole technique is applied to distinguish phase conjugation from beam cleanup, and a new technique to measure fidelity more accurately throughout the full range from zero to one is described and tested.

3.3.2. Fiber Amplifiers

While much of the research into SBS in fiber amplifiers has been focused on raising the SBS threshold to obtain higher power amplifiers, Heuer *et al.* used fiber amplifiers as a phase conjugate medium.[42, 106] In the experiment achieving the lowest SBS threshold, Heuer used a 10 m Yb-doped fiber with a 47 μm core co-pumped with a 20 W, 940 nm wavelength diode laser (see Fig. 13). The fiber core was doped with Yb to achieve a cladding-launched pump absorption of 1.5 dB/m. The signal laser was pulsed with a duration of 100 ns. With no pump power, the SBS threshold was reached with a signal energy of 12 μJ/pulse. The effective length of the unpumped fiber is somewhat shorter than the length with a low pump power due to signal absorption by Yb. With 20 W pump power, threshold was achieved at 0.5 μJ for a threshold reduction by a factor of 24. Considering the signal pulse duration, Heuer assessed the equivalent cw threshold power at ~5 W. In addition, due to the use of a fiber amplifier to generate the phase conjugate, a reflectivity of ~8000% was achieved when operating just above threshold. This reflectivity declined with increased signal power due to amplifier saturation. Fidelity was measured using an aberration with the energy-in-the-bucket technique at 0.9

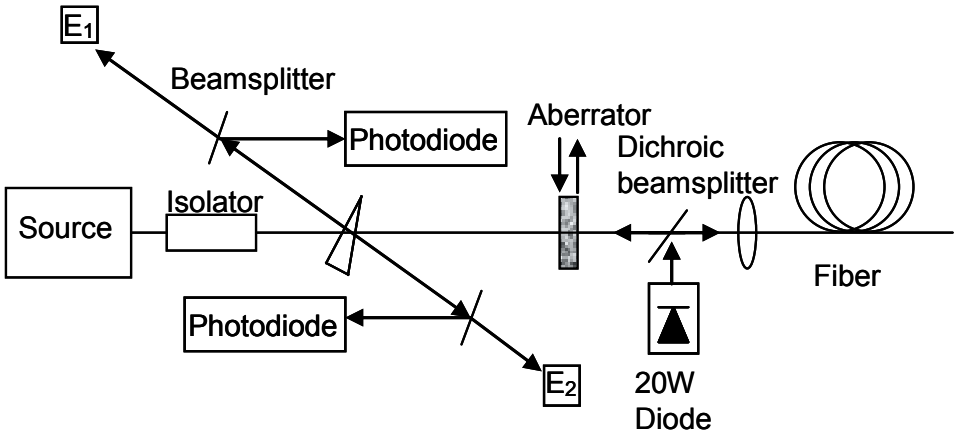

Fig. 13: Apparatus used to investigate SBS phase conjugation using a fiber amplifier.[106]

for signal energies at ~20 times threshold, and the fidelity decreased slightly to 0.8 as the signal energy was increased to 200 times threshold.

3.3.3. Chalcogenide Fiber

Recent experiments using chalcogenide glass fiber have discovered a very high Brillouin gain coefficient in this material. SBS threshold has been achieved with a cw signal laser in single-mode chalcogenide fiber, but there have been no phase-conjugation experiments conducted.

Chalcogenide glass has been made into mid-IR transmission fiber and is now available commercially. This breakthrough was made possible by research at the Naval Research Laboratory which succeeded in reducing impurities.[107, 108] In addition to its low attenuation in the mid-IR region, chalcogenide fiber is being developed for its high nonlinear properties. Using fiber drawn at the Naval Research Laboratory, Florea *et al.* measured the Brillouin gain coefficient of a single mode As_2Se_3 glass fiber at (6.76+/-0.36)x10^{-9} m/W.[109] The fiber was 5 m long with a core diameter of 6.5 μm and an NA of 0.14. The measurement was performed using an amplified 1.56 μm wavelength DFB

laser source to generate SBS. The attenuation in the fiber was estimated at 0.9 dB/m, and the SBS threshold was found at 127+/-7 mW. In a similar experiment, Abedin determined the Brillouin gain coefficient using a 5 m length of As_2Se_3 fiber to be $6x10^{-9}$ m/W.[25] The fiber had an attenuation of 0.84 dB/m at 1.55 μm wavelength, a 6 μm core diameter, and an NA of 0.18. The SBS threshold for this fiber was 85 mW. This is approximately 120 times greater than the Brillouin gain coefficient of silica. It should be noted that in the reports of both Abedin and Florea, the reported Brillouin gain coefficient includes the use of a polarization factor of $K_g = 0.5$ (see Section 2.3).

3.3.4. Tellurite Fiber

Tellurite glasses have recently been developed into fiber optics with scattering losses as low as 20 dB/km at 1.2 μm wavelength.[110] The development is being pursued mainly due to the large gain bandwidth of the tellurite host doped with erbium, as well as the ability to dope tellurite with erbium at a much higher concentration than silicate glasses.[111-115] Some of this work has been sponsored by the Defense Threat Reduction Agency in a contract with NP Photonics.[116] It was discovered that the Brillouin gain coefficient in tellurite glass is approximately 20 times higher than silica, but phase conjugation experiments have not been conducted.

It was predicted and discovered that the stimulated Raman scattering gain coefficient in tellurite fiber is much higher than in silica fibers.[115, 117-119] Mori *et al.* found the Raman gain coefficient to be 16 times that of silica fiber in side-by-side experiments. Measurements of the Brillouin gain coefficient in tellurite soon followed. In 2004, scientists at the Army Research Laboratory measured the Brillouin gain of bulk tellurite glass at ~$1x10^{-9}$ m/W. The Brillouin gain coefficient in single-mode tellurite

fiber was measured experimentally in 2006 by Abedin.[26] Using 2 m and 3 m lengths of single-mode tellurite fiber with an NA of 0.36, the SBS threshold was found at launched signal powers of 1 W and 630 mW, respectively. The fiber had an attenuation of 0.51 dB/m, and Abedin calculated the Brillouin gain coefficient through several different methods to be (1.82+/-0.35)x10^{-10} m/W, where the factor $K_g = 0.667$ was used. A second group found SBS threshold in a low-loss, single-mode tellurite fiber at 1.7×10^{-10} m/W .[120, 121] This fiber had an NA of 0.43 and a length of 200 m. In determining the SBS gain coefficient, the factor $K_g = 0.5$ was used.

3.3.5. Conclusion

In this section, a reduction of SBS threshold and improvement in phase conjugation fidelity was shown using pulsed lasers focused into waveguides. The SBS threshold was reduced further using smaller diameter waveguides. Other techniques that have resulted in reduced SBS threshold include the use of fiber amplifiers, longer fibers, feedback or Stokes seeding techniques, and materials with higher Brillouin gain coefficients. Longer fibers have produced phase conjugation fidelity higher than predicted by Hellwarth and Zel'dovich's models as given in Eq. (2.65) and Eq. (2.66), but the coherence length of the signal laser may have limited the interaction length between signal and Stokes beams. Feedback and seeding techniques were shown to reduce threshold but interfere with the fidelity of phase conjugation. The SBS gain coefficient has been measured in the single-mode tellurite and chalcogenide fibers, but phase conjugation has not been reported. A measurement of the fidelity of phase conjugation as a function of fiber length has not

been conducted, and cw phase conjugation has not been achieved. This is the main goal of this research effort.

3.4. Phase Conjugation Models

In the literature, when SBS is not being generated in a fiber amplifier, the seed is called a pump. The language is valid since the pump excites a virtual energy level to generate a Stokes beam through the scattering process. In the description of these models, the seed will be called the pump since SBS is not being generated in a fiber amplifier where the terminology would become ambiguous.

Several models have been produced which calculate the phase conjugation fidelity from SBS in optical waveguides. There are several models that are accurate for the case of fidelity near 1, but approximations were made which invalidate the models for decreased fidelity. Lehmberg's numerical model examined the fidelity as a function of average irradiance and divergence angle over short interaction lengths.[122] Lehmberg accounted for pump depletion, but the model sets $\Delta\lambda = 0$ and therefore fails to account for a decrease in fidelity as fiber length is increased. Both Zel'dovich *et al.*[57] and Hellwarth[29] reached analytical solutions for the length limitation on fidelity by neglecting pump depletion and solving for the case of near perfect fidelity. Zel'dovich approximated the non-conjugated fraction of the Stokes beam in Taylor series expansion and kept only the first few terms, which limited the validity of the model to near-perfect fidelity.[57] This method resulted in an equation showing a dependence on the seed profile and beam shape. Hellwarth evaluated the phase-conjugate fidelity that could be obtained from a waveguide as a function of waveguide length, core area, and number of

modes excited. His analysis was based on a perturbation of perfect fidelity phase conjugation which loses validity as fidelity decreases.

Without making approximations of high fidelity, Lombard *et al.* solved for the SBS gain per mode of both a step-index and graded-index fiber with the assumption that all modes were equally excited by the pump.[64] Pump depletion was included in the gain determination under the approximation of uniform depletion of the pump and amplification of the Stokes modes. However, the fidelity achieved was not analyzed as a function of fiber length. The authors deferred to Hellwarth for that discussion, and used the model only to show uniform gain across modes in a short, step-index fiber, while showing preferential mode selection for a long, graded-index fiber.

In a model related to phase conjugation fidelity, Russell *et al.* analyzed the phase difference accumulated between the lowest and highest-order modes supported by the fiber. [55] This model determines the maximum fiber length allowed by a given difference in phase accumulated between the Stokes and pump modes. This model clearly showed an increasing phase error as the length of fiber was increased, but the relationship between phase mismatch and phase conjugation fidelity was undetermined.

The experimental work of this dissertation inspired a full, three-dimensional analysis of phase conjugation in step-index waveguides which included pump-depletion effects.[63, 123] Free-space Fourier propagation was used to propagate a Gaussian beam through a pinhole and focus off-center onto the tip of a fiber as done in the experiment which is described in Chapter 6. The fiber modes were determined from the physical characteristics of the fiber with numerical root solving methods to find the modal transverse and longitudinal propagation constants. The electric field of each mode in a

transverse plane was then determined from the propagation constants. The product of the incident field and a random field in the fiber was integrated over the transverse dimension at the face of the fiber and maximized using a perturbation algorithm to obtain a set of fiber modes with amplitudes and phases that closely matched the incident field. The SBS portion of the model solved for the Stokes field at the tip of the fiber by perturbing the Stokes field until one was found which received the highest SBS gain over the volume of the fiber. The resulting Stokes beam was then counter-propagated in free space to determine the transmission through the pinhole. The SBS portion of the model is discussed in more detail here.

The equations describing stimulated Brillouin scattering are given by Eq. (2.49) and are shown again here:[54]

$$\begin{aligned}\frac{\partial I_p(r_\perp,z)}{\partial z} &= -g_B(r_\perp)\frac{\omega_p}{\omega_s}I_p(r_\perp,z)I_s(r_\perp,z)-\alpha_p I_p(r_\perp,z)\\ \frac{\partial I_s(r_\perp,z)}{\partial z} &= -g_B(r_\perp)I_s(r_\perp,z)I_p(r_\perp,z)+\alpha_s I_s(r_\perp,z)\end{aligned} \tag{3.3}$$

where $g_B(r_\perp)$ represents the Brillouin gain, $I_{p,s}(r_\perp)$ represents the irradiance of the pump or Stokes beam, $r_\perp$ is the transverse fiber direction, and $\alpha_{p,s}$ represents transmission loss in the fiber at the pump and Stokes beam frequency. The transmission loss in silicate fibers is typically less than 5 dB/km and was neglected due to the relatively short lengths of fiber where this model was concerned. The pump and stokes fields are represented as a summation over the fiber mode fields as[55]

$$E_{p,s}(r_\perp,z,t)=\sum_f A^f_{p,s}(z)\psi^f_{p,s}(r_\perp)\cos(\beta^f_{p,s}z-\omega_{p,s}t+\phi^f_{p,s}). \tag{3.4}$$

The summation is over all the modes allowed by the fiber f, and includes both radial and azimuthal dependence represented by a single variable, $r_\perp$. The amplitude of each pump

or Stokes mode is represented by $A_{p,s}^{f}(z)$, and the field radial and azimuthal dependences are given by $\psi_{p,s}^{f}(r_{\perp})$. The longitudinal propagation constant, $\beta_{p,s}^{f}$, applies to the particular pump or Stokes mode, while $\omega_{p,s}$ and $\phi_{p,s}^{f}$ are the pump or Stokes radial frequency and modal phase factors, respectively. Following the work of Russell *et al.*,[55] the irradiance of a pump or Stokes mode was given by

$$\begin{aligned} I_{p,s}(r_{\perp},z) &= 2\varepsilon_0 cn\left\langle E_{p,s}(r_{\perp},z,t)^2\right\rangle \\ &= \varepsilon_0 cn\sum\nolimits_{f,q} A_{p,s}^{f}(z)A_{p,s}^{q}(z)\psi_{p,s}^{f}(r_{\perp})\psi_{p,s}^{q}(r_{\perp})\cos(\Delta\beta_{p,s}^{fq}z+\Delta\phi_{p,s}^{fq}), \end{aligned} \tag{3.5}$$

where the brackets indicate a time average of the field, ε_0 is the permittivity of free space, n is the index of refraction of the fiber core, and c is the speed of light. Shorthand notation was used such that $\Delta\beta_{p,s}^{fq}=\beta_{p,s}^{f}-\beta_{p,s}^{q}$, and similarly for $\Delta\phi_{p,s}^{fq}$.

SBS causes an increase in amplitude of the scattered fields which correspond to a decrease in amplitude of the pump fields. In reality, these rates are mode dependent and coupled together such that the Stokes increase in one mode may correspond to a decreased amplitude of multiple pump modes. To simplify the analysis, all the modes of either the pump or Stokes were approximated to vary at the same rate. This was represented by[55]

$$A_{p,s}^{f}(z)=\kappa_{p,s}(z)A_{p,s}^{f}(0). \tag{3.6}$$

In this equation, $\kappa_{p,s}(z)$ represents the change in amplitude common to all modes of either the pump or Stokes beams, and $A_{p,s}^{f}(0)$ represents the mode field amplitude at the pump input end of the fiber. By integrating over the transverse area, the change in Stokes irradiance described by Eq. (3.3) was expressed as[55]

$$\frac{\partial P_s(z)}{\partial z} = g(\varepsilon_0 cn)^2 \sum_{f,q,j,v} A_{ppss}^{fqjv} \gamma_{ppss}^{fqjv} \kappa_s(z)^2 \kappa_p(z)^2 \cos(\Delta\beta_p^{fq} z + \Delta\phi_p^{fq}) \cos(\Delta\beta_s^{jv} z + \Delta\phi_s^{jv}), \quad (3.7)$$

which includes new notation

$$\begin{aligned} A_{ppss}^{fqjv} &= A_p^f(0) A_p^q(0) A_s^j(0) A_s^v(0) \\ \gamma_{ppss}^{fqjv} &= \int \psi_p^f(r_\perp) \psi_p^q(r_\perp) \psi_s^j(r_\perp) \psi_s^v(r_\perp) dr_\perp \ . \end{aligned} \quad (3.8)$$

After making the substitution $\kappa_s(z)^2 = P_s(z)/P_s(0)$, Eq. (3.7) was integrated using separation of variables to yield an equation for $P_s(L)$ such that[63]

$$P_s(L) = \exp\left[-\frac{g(\varepsilon_0 cn)^2}{P_s(0)} \int \sum_{f,q,j,v} A_{ppss}^{fqjv} \gamma_{ppss}^{fqjv} \kappa_p(z)^2 \cos(\Delta\beta_p^{fq} z + \Delta\phi_p^{fq}) \cos(\Delta\beta_s^{jv} z + \Delta\phi_s^{jv}) dz \right]. \quad (3.9)$$

To evaluate the integral in the exponential, an expression for $\kappa_p(z)$ was derived. The assumption that all the pump modes are depleted at the same rate is equivalent to a single-mode fiber approximation with a constant transverse intensity profile across the core for purposes of pump depletion. With the additional approximation that the fiber is lossless, the differential equations are:

$$\begin{aligned} \frac{\partial I_p(z)}{\partial z} &= -g_B I_p(z) I_s(z) \\ \frac{\partial I_s(z)}{\partial z} &= -g_B I_s(z) I_p(z) \end{aligned} \quad (3.10)$$

As discussed by Boyd,[16] these equations imply $I_p(z) = I_s(z) + C$ where C is a constant. Since $\kappa_p(z)^2 = I_p(z)/I_p(0)$, separation of variables was used to solve Eq. (3.10), yielding

$$\kappa_p(z)^2 = \frac{I_s(0)[I_p(0) - I_s(0)]}{I_p(0)^2 \exp\{gz[I_p(0) - I_s(0)]\} - I_s(0) I_p(0)} + 1 - \frac{I_s(0)}{I_p(0)}. \quad (3.11)$$

The procedure detailed by Boyd[16] for the "SBS Generator" was used to solve a transcendental equation for $I_s(0)$ in terms of total SBS gain, $G_B = g_B I_p(0)L$, and SBS threshold gain as determined by experiment. Using this description of pump depletion, Eq. (3.9) was evaluated numerically.

To reduce computation time, the product of cosines in Eq. (3.9) was approximated as done by Hellwarth[29] using a trigonometric identity such that

$$\begin{aligned} &2\cos(\Delta\beta_p^{fq} z + \Delta\phi_p^{fq})\cos(\Delta\beta_s^{jv} z + \Delta\phi_s^{jv}) \\ &= \cos[(\Delta\beta_p^{fq} - \Delta\beta_s^{jv})z + \Delta\phi_p^{fq} - \Delta\phi_s^{jv}] + \cos[(\Delta\beta_p^{fq} + \Delta\beta_s^{jv})z + \Delta\phi_p^{fq} + \Delta\phi_s^{jv}]. \end{aligned} \tag{3.12}$$

For nonzero $\Delta\beta_p^{fq}$ and $\Delta\beta_s^{jv}$, most mode combinations would result in large values for these $\Delta\beta$ terms which oscillate rapidly and integrate to negligible values over short fiber distances. Only certain mode combinations were computed in the model. When $f = q$ and $j = v$, both cosine terms on the right-hand side of Eq. (3.12) equal one. Owing to the similarity of the propagation constants under the small frequency shift of SBS, the contribution of the cosine term is small compared to the case of $f = j$ and $q = v$ for the first cosine term on the right-hand side of Eq. (3.12). This is the case when the pump and Stokes modes being compared are in corresponding fiber modes. The same is true when $f = v$ and $q = j$ for the second cosine term on the right of the equation. Therefore, the product of cosines was simplified to[63]

$$\begin{aligned} &\cos(\Delta\beta_p^{fq} z + \Delta\phi_p^{fq})\cos(\Delta\beta_s^{jv} z + \Delta\phi_s^{jv}) \\ &\simeq \begin{cases} \frac{1}{2}\cos[(\Delta\beta_p^{fq} - \Delta\beta_s^{jv})z + \Delta\phi_p^{fq} - \Delta\phi_s^{jv}], & \text{if } f = j \text{ and } q = v \neq f \\ \frac{1}{2}\cos[(\Delta\beta_p^{fq} + \Delta\beta_s^{jv})z + \Delta\phi_p^{fq} + \Delta\phi_s^{jv}], & \text{if } f = v \text{ and } q = j \neq f \\ 1, & \text{if } f = q \text{ and } j = v \\ 0, & \text{otherwise .} \end{cases} \end{aligned} \tag{3.13}$$

The Stokes beam generated in the fiber is the combination of fiber modes that experiences the highest SBS gain. For a given combination of Stokes modes, the backscattered Stokes power was computed using Eq. (3.13) and Eq. (3.11) to solve Eq. (3.9). An algorithm was used to find the amplitudes and phases of the Stokes modes that produced the maximum backscattered power for a given pump configuration. The algorithm steps through the amplitude and phase of each Stokes mode and outputs the solution when the iteration fails to improve power more than a set percentage. The sum of all the Stokes modes was then propagated back through free space to the pinhole aperture to determine fidelity.

The results of the model are plotted in Fig. 14 for two different fibers. In Fig. 14(a), the fiber core diameter was 20 μm with an NA of 0.13. In Fig. 14(b), the fiber core diameter was 40 μm with an NA of 0.06. Hellwarth's model is also shown for these fibers. The results show that Spring's model predicts the same fidelity in lengths of fiber that are approximately an order of magnitude longer than the calculations of Hellwarth's model. In addition, Spring's model predicts that fidelity declines slower with length for the fiber with a lower NA.

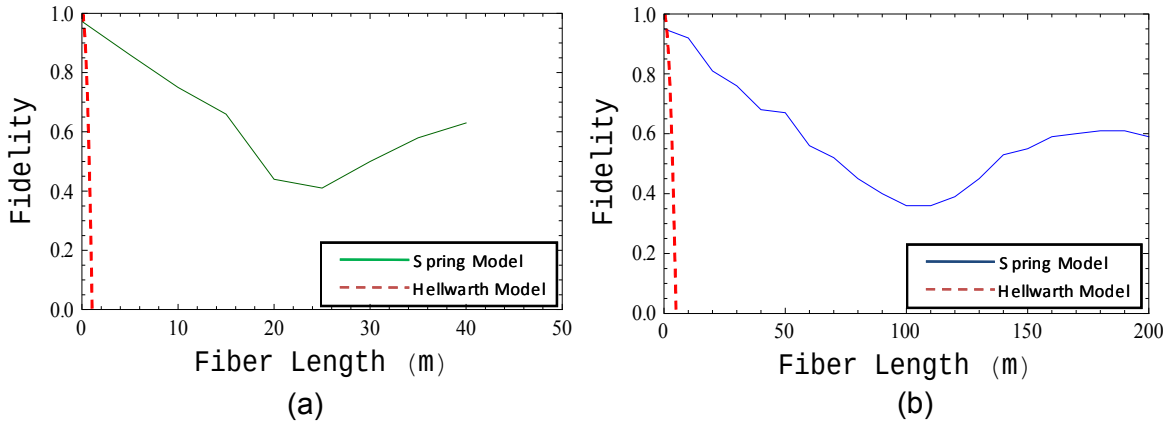

Fig. 14: Spring and Hellwarth models of fidelity achieved as a function of fiber length for (a) the 0.13-NA fiber and (b) the 0.06-NA fiber.[29, 63]

After the fidelity has dropped to a low value, the model predicts a rise in fidelity as the fiber length increases. This effect resulted from modal phase interactions such that $(\Delta\beta_p^{fq} \pm \Delta\beta_s^{jv})z = m2\pi$, where m is an integer.[63] When multiple mode sets reach an integer number of 2π change in phase near the same length of fiber, the mode mismatch is mitigated, and the model predicts fidelity increases at that length of fiber.

3.5. Coherent Beam Combination via SBS

While coherent beam combining is not the direct goal of this research effort, it is the main application of cw phase conjugation via SBS that is being explored in this work. Due to materials constraints, single-fiber power scaling of single-frequency beams reaches a power ceiling. By combining elements, the power can be scaled beyond the restrictions set by the single elements. By simply overlapping a number of beams N in space, the irradiance of each beam adds to result in a beam that is N times the single element irradiance. However, if the beams are coherent, the electric fields add. This results in an incident irradiance that can be N^2 times the single element irradiance if the beams are in phase and constructively interfere. The problem becomes the construction of an array of lasers that are all in phase with each other. The two main approaches are through electro-optic control of each element or to combine the amplifiers using nonlinear optics.

To combine an array of elements coherently using electro-optics, each element is first seeded by the same master oscillator. The optical paths of each of the fiber amplifiers must be set and controlled to within a fraction of a wavelength to account for vibrations and temperature fluctuations. To accomplish this, these methods typically

compare the phase of each element with that of a reference beam at a photodetector and electronically adjust the phase of each element using fiber stretchers or electro-optic phase modulators to maintain coherence.[124-128] Using high-power, Yb-doped, single-mode amplifiers and lithium niobate phase modulators, Anderegg *et al.* achieved 470 W by coherently combining 4 amplifier channels.[129] AFRL recently demonstrated locking of 9 passive channels and, separately, an array of 6 amplifier channels using a self-referencing technique that resulted in residual phase error of $\lambda / 20$.[124]

Beam combination can also be performed by SBS phase conjugation without wavefront sensors or electronic feedback and control mechanisms. If the phase conjugate fidelity is high, the effect of wavefront reversal ensures that the Stokes beam propagates back through the amplifier channels and that the phases of the beams are locked after the second pass through the amplifier channels. Coherent beam combination via SBS has been studied thoroughly in pulsed laser systems with many successful results. There have been several studies using cw lasers, but none have employed a full spatial phase-conjugate beam.

As reported by Valley *et al.*, the first experiments demonstrating phase locking of two channels via SBS were performed by Basov in 1980 using a pulsed laser.[130] Basov split a single beam into two passive channels using a 50/50 beamsplitter and coupled both channels into a common waveguide for SBS phase conjugation. The two channels became a single aberrated wavefront in the SBS cell. A high-fidelity, phase-conjugate reflection was created by the SBS cell which locked the phases of the Stokes beam after back-propagation through the two channels.

Basov *et al.* were also the first to demonstrate a constraint on the path length differences that can be compensated by SBS phase conjugation. Due to the frequency shift between the signal and Stokes beams, there is a residual phase error between different channels when path length differences exist. The residual phase error or "piston error" is given by[131]

$$\delta = \frac{\Omega_{Bo}\Delta L}{c}, \tag{3.14}$$

where ΔL is the optical path length difference, Ω_{Bo} is the SBS frequency shift given by $\Omega_{Bo} = \frac{2\omega_s v_a}{c/n}$, and δ is in radians. As reported by Moyer,[132] when the Stokes beams in the two channels were conjugated with high fidelity, the beams recombined at the 50/50 beamsplitter and constructively interfered in the direction towards the source laser. However, when Basov introduced a delay in one of the legs such that $\delta = \pi$, the beams constructively interfered in the direction away from the source laser. Basov remarked that this effect may be used to out-couple power from a phase-locked, multiple-channel amplifier system. The residual phase error given by Eq. (3.14) was confirmed in experiments by Rockwell *et al.* in 1986.[131]

Many investigations have been performed to coherently combine multiple channels using pulsed lasers in focused SBS cells filled with a liquid or gas.[130, 133-139] The reported experiments were typically successful, combined up to 8 parallel amplifiers,[134] and achieved phase errors among the channels as low as $\lambda/27$.[135] However, the scientists routinely discuss the extreme sensitivity to misalignment of the beams in the SBS cell. Sternklar *et al*. quantifies the misalignment sensitivity to a tolerance of +/-0.64 beam spot diameters in the focal plane. The beams must be carefully

overlapped in the SBS cell to obtain a common phase. Aberrated beams were shown to have more relaxed overlap requirements,[130] presumably due to the larger diameter at focus of an aberrated beam. SBS in an optical fiber as discussed in this work relaxes this requirement slightly, requiring only that the beams are coupled into the same waveguide where an SBS phase conjugate beam is generated.

Another attempt to lock the phases of multiple channels using SBS in a focused cell architecture seeded the SBS cells with a frequency-shifted Stokes seed. This technique has been examined theoretically[138, 140] and experimentally,[130, 138] with the goal of fixing a common phase among all the channels through seeding the SBS process. Using a computer model of steady-state SBS processes called BOUNCE,[122] Moyer *et al.* calculated that the phases of multiple channels should be locked when the SBS process is seeded with a Stokes beam with an irradiance that is greater than 10^{-6} times the signal beam irradiance. In contrast to this, Moyer discovered experimentally that the power in the seed beam that was needed to lock the phase of the Stokes beams to that of the seed was closer to 1% of the signal power. In addition, when a seed was used as a common reference to lock the phase, the conjugation fidelity dropped and the coherence of the piston-error conjugation disappeared. Moyer comments that seeding the SBS cell causes the cell to act as a seed amplifier rather than a phase conjugate medium. Seeding the SBS process is one method to lower the SBS threshold, but Moyer's results show that phase conjugation fidelity suffers when this technique is used.

The use of a light guide for SBS phase conjugation in beam combining ensures the overlap of the signal beams once coupled into the guide.[134, 141] Using a pulsed laser with pulse duration of 15 ns, phasing of two optical paths was investigated at AFIT

using a 600 μm-core fiber as the phase-conjugate medium.[142] The two paths were split and recombined using prisms before being coupled into the same multimode fiber. Willis *et al.* used a lateral shearing interferometer to show that the two channels were phased when a phase-conjugate reflection was generated, and that the beams were not phased when reflected using a basic mirror.

The beam-cleanup property of long, graded-index fibers has also been used for beam combination without generating a phase-conjugate reflection.[65, 99, 143] In these experiments, up to five beams were coupled into a multimode, graded-index fiber several kilometers in length. Through SBS beam cleanup, the Stokes beam emerges with beam quality near the diffraction limit. This effect was demonstrated for coherent combining as well as incoherent beam combining. In contrast to beam combination using SBS phase conjugation, the Stokes beam generated in these experiments does not propagate back through the amplifiers.

Grime *et al*. demonstrated cw phasing of a 2-channel amplifier using polarization conjugation in long, optical fiber without generating a spatial phase conjugate (Fig. 15).[144] This technique involves polarization combining of a maximum of two single-mode amplifier channels into a long fiber where beam cleanup occurs. In the experiment, the single-frequency beam from an NPRO was amplified by a rod amplifier to 2 W before being split into two beams of semicircular cross-section by a prism. Each beam was coupled into separate single-mode fiber amplifiers and amplified to ~10 W. The beams were then polarization combined and coupled into a 4 km long fiber with a 50 μm-core diameter. Through the beam cleanup effect of graded-index fibers, a single-mode Stokes beam was created which conjugated the polarization of the combined input signal.

After propagating back through the polarizing beamsplitter, the Stokes beams passed once more through the amplifiers to recombine at the prism beamsplitter. A lateral shearing interferometer was used to verify that the two beams were phased at this point. If a phase-conjugate beam was created by SBS, there could be more than 2 amplifier channels and the amplifiers could be multimode.

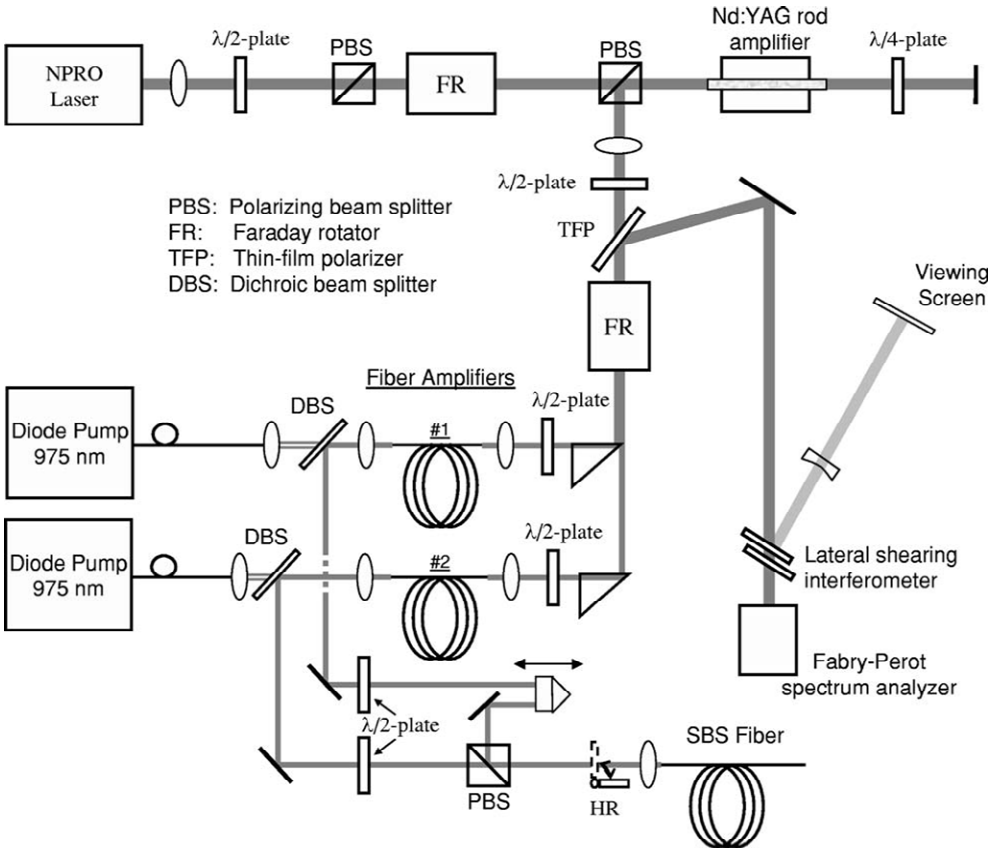

Fig. 15: Schematic of the apparatus used to phase two amplifier channels using SBS beam cleanup in multimode fiber.[144]

4. SBS Threshold Modeling

4.1. Overview

In this work, high power, narrow-bandwidth amplifiers must be constructed without reaching SBS threshold. In contrast, multimode fibers must be evaluated such that SBS threshold is achievable to generate the phase conjugate beam using the output power from the fiber amplifiers. An SBS threshold model was created for this purpose.

The SBS threshold power in high-power, fiber amplifiers has been found to be much higher than predicted by using the Smith model given by Eq. (2.53) and repeated here, $P_{th} \approx 21 A_{eff} / (g_B L_{eff})$. By incorporating the change in SBS frequency shift with fiber temperature in a model of SBS gain in fiber amplifiers, Kovalev was able to explain the increased SBS threshold power.[45] The temperature variation is a result of the quantum defect between the pump and laser frequencies coupled with non-uniform pump irradiance throughout the length of the fiber. However, the choice of pump geometry was ignored in Kovalev's model. Using traditional pump-coupling techniques through the tip of the fiber, the pump can be introduced into the signal output end (counter-pumped), the signal input end (co-pumped), or both ends (dual-end-pumped). Unlike the amplifiers he was modeling, Kovalev's model included only the counter-pumped architecture.

With the pump power and pump absorption set to near zero, the model predicts the SBS gain and threshold of a lossless, passive fiber similar to Smith's model. As discussed in Chapter 3, chalcogenide and tellurite fibers have significant scattering loss at the wavelengths being considered in this work. These scattering losses not only suppress the signal, but also the SBS gain.

In this work, the choice of pump-coupling geometry was added to the model and predicts that the SBS threshold of a co-pumped amplifier can be less than half the threshold of a counter-pumped amplifier. Scattering loss was incorporated, and no approximations were made to require low-loss fiber as in Smith's derivation. The deviation from Smith's model becomes significant at approximately 0.5 dB/m of attenuation. The approach used in this model was confirmed by the modeling efforts of two research groups.[145-147] In addition, the disparate Brillouin gain coefficients measured by several research groups are shown to be related through Brillouin gain broadening as a function of fiber NA without use of the polarization factor K_g.

4.2. Model of SBS Threshold

The model starts with the growth of a signal beam (P_s) with distance as given by Yariv:[148]

$$\frac{dP_s(z)}{dz} = \frac{\gamma P_p(z)}{P_{st} + P_s(z)} P_s(z) P_{st} - \alpha_s P_s(z), \tag{4.1}$$

where $P_s(z)$, $P_p(z)$, and P_{st} are the signal, pump, and saturation powers respectively, γ is the pump-to-gain conversion coefficient, and α_s is the scattering loss coefficient of the fiber. To account for pumping from the front or back ends of the fiber, let $P_{pf}(z)$ represent the pump power coupled into the front of the fiber, while $P_{pb}(z)$ represents the pump power coupled into the back end of the fiber. Assuming that the pump absorption from the front and back are independent, the total pump power along the length of the fiber is the sum of power from the two ends such that $P_p(z) = P_{pf}(z) + P_{pb}(z)$. The equations

$$\frac{dP_{pf}(z)}{dz} = -(\alpha_s + \alpha_{Yb})P_{pf}(z)$$
$$\frac{dP_{pb}(z)}{dz} = (\alpha_s + \alpha_{Yb})P_{pb}(z) \tag{4.2}$$

describe the attenuation of the pump as a function of fiber length when co-pumped and the growth of the pump power in the fiber as a function of length when counter-pumped.

The amplification of the signal can be described as:

$$\frac{dP_s(z)}{dz} = \frac{P_s(z)P_{st}\gamma}{P_{st} + P_s(z)}[P_{pf}(0)e^{-(\alpha_s+\alpha_{Yb})z} + P_{pb}(L)e^{(\alpha_s+\alpha_{Yb})(z-L)}] - \alpha_s P_s(z), \tag{4.3}$$

where the pump power has been integrated from Eq. (4.2) and substituted into Eq.(4.1). Then the change in Stokes power with fiber length is:

$$\frac{dP_B(z)}{dz} =$$
$$-g_b(z,F)P_B(z)\frac{P_s(z)}{A_{eff}} - \frac{P_B(z)P_{st}}{P_{st} + P_s(z)}\gamma[P_{pf}e^{-(\alpha_s+\alpha_{Yb})z} + P_{pb}e^{(\alpha_s+\alpha_{Yb})(z-L)}] + \alpha_s P_B(z), \tag{4.4}$$

where

$$g_b(z,F) = \frac{g_I\Gamma_B(\Gamma_B + C_\delta\Delta T(z))}{(\Gamma_B + C_\delta\Delta T(z))^2 + 4(F_o + C_f\Delta T(z) - F_v)^2}. \tag{4.5}$$

In Eq. (4.5), g_I is given by Eq. (2.58), C_δ is the change in bandwidth with temperature, and C_f is the change in Brillouin frequency shift with temperature. The room temperature Brillouin frequency shift is F_o, F_v is the frequency of the Stokes beam, ΔT is the change in temperature as a function of fiber length, and Γ_B is the Brillouin gain bandwidth at room temperature. The terms on the right hand side of Eq. (4.4) represent the gain and loss of the Stokes power as a function of fiber length. The first term represents the gain in Stokes power due to SBS, $-P_B(z)G_B(z,F)$, where the negative sign represents increasing power in the direction of $-z$. The second term is the gain in Stokes

power from the amplifier, $-P_B(z)G_L(z)$, and the third term is a scattering loss, $+P_B(z)G_s(z)$. After integrating over *z*, the SBS threshold is approximated by $G_B(F)+G_L-G_s \approx 21$. Provided the scattering loss term includes negligible absorption, the change in temperature along the length of the fiber is given by[44]:

$$\Delta T(z) = \frac{\alpha_{Yb}\eta P_p(z)a^2}{2\pi b^3 h} \tag{4.6}$$

where η is the quantum defect, *a* and *b* are core and pump cladding radii respectively, and *h* is the convective coefficient at the fiber surface, approximated at 0.8+/-0.3 W/m^{2}K for a fiber in ambient air and 1.7+/-0.3 W/m^{2}K for an actively air-cooled fiber.[45]

Assuming high power operation allows $P_s(z) >> P_{st}$, such that the denominators can be approximated as $P_{st}+P_s(z) \approx P_s(z)$. With this approximation, Eq. (4.3) can be integrated to find an equation for the signal power as a function of fiber length:

$$P_s(z) = P_s(0)e^{-\alpha_s z} + \frac{\gamma P_{st}}{2\alpha_s+\alpha_{Yb}} P_{pb} e^{-(\alpha_s+\alpha_{Yb})L}(e^{(\alpha_s+\alpha_{Yb})z} - e^{-\alpha_s L}) + \frac{\gamma P_{st}}{\alpha_{Yb}} P_{pf}(e^{-\alpha_s z} - e^{-(\alpha_s+\alpha_{Yb})z}). \tag{4.7}$$

In the absence of scattering losses, the slope efficiency of the fiber amplifier is represented by

$$\eta_{sl} = \frac{\gamma P_{st}}{\alpha_{Yb}}, \tag{4.8}$$

which can be used to estimate γ. The Brillouin gain is found by integrating Eq. (4.4) over the length of the fiber. This integration can be performed using the NIntegrate function of Mathematica. The result is that the Brillouin gain is the sum of the amplification of the Stokes signal owing to SBS and that due to laser gain. Stimulated Brillouin scattering threshold occurs when the sum of the Brillouin gain, laser gain of the Stokes beam, and

scattering loss reaches approximately 21 when started from noise (1 photon per mode) at the output end of the fiber.[19]

4.3. Fiber Amplifier SBS Threshold

The general trend this modeling has revealed is that co-pumping (exciting the Yb by launching the pump into the cladding of the fiber from the same end as the incident signal) results in relatively high signal power through a long section of the fiber amplifier where the thermal gradient is small. The thermal gradient in the fiber follows the pump absorption according to Eq. (4.6), resulting in a large thermal gradient at the front end of the fiber where the signal power is lower. At the back end of the fiber, the signal power is higher and the thermal gradient is less, resulting in favorable conditions for SBS generation. In contrast, counter-pumping (launching pump power into the cladding from the signal output end of the fiber) causes the signal power to increase rapidly near the back end of the fiber. The thermal gradient is high at this portion of the fiber where the signal power increases due to counter-pumping. This results in a much lower SBS gain and higher threshold power for the counter-pumped amplifier. Using the model, the fiber amplifiers used in this work were designed and built at wavelengths of 1064 nm (ytterbium fiber amplifiers) and 1550 nm (erbium-ytterbium fiber amplifiers).

4.3.1. Ytterbium Fiber Amplifier

The amplifiers in this work are constructed using Nufern large-mode-area fibers. The Yb-fiber amplifiers are pumped with one or two 100 W LIMO diodes at 976 nm. The fiber characteristics are listed in Table 2.

To demonstrate the difference between a co-pumped and counter-pumped amplifier configuration, a diagram of a co-pumped amplifier is shown in Fig. 16. The diode pump is coupled to the fiber amplifier at the front end of the fiber where the seed is also coupled. With a seed power of 4 W, the temperature difference and signal power as a function of position in the fiber at the calculated SBS threshold is shown in Fig. 17 for a co-pumped amplifier. The SBS gain coefficient was approximated at 3×10^{-11} m/W for modeling purposes. The output power achieved in this configuration for a 10 m fiber is ~22 W. In contrast, the SBS threshold for a counter-pumped amplifier of the same length is over 50 W. In the counter-pumped architecture, the power rises rapidly and is high over a very short length of fiber, and the temperature gradient is high over the same length of fiber. These two conditions raise the SBS threshold for the counter-pumped configuration.

Table 2: Characteristics of Nufern, large-mode-area, fiber amplifiers.

	Fiber characteristics
Core diameter (μm)	20
Core NA	0.06
Cladding diameter (μm)	400
Cladding Yb absorption (dB/m)	1.4
Fundamental mode $1/e^2$ diameter (μm)[a]	18
Slope efficiency (%)[b]	77

[a]Marcuse, D., *Loss analysis of single-mode fiber splices.* Bell Syst. Tech. J, 1977. 56(5): p. 703–718.
[b]This work

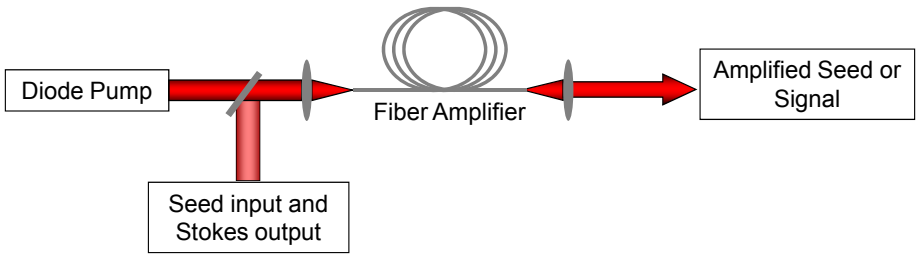

Fig. 16: Diagram of a co-pumped fiber amplifier.

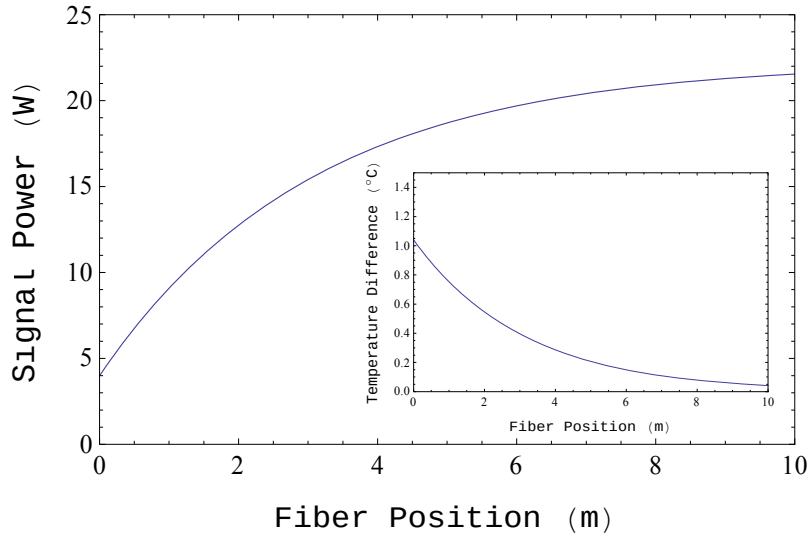

Fig. 17: Signal power and temperature difference as a function of position in a co-pumped fiber amplifier at the SBS threshold.

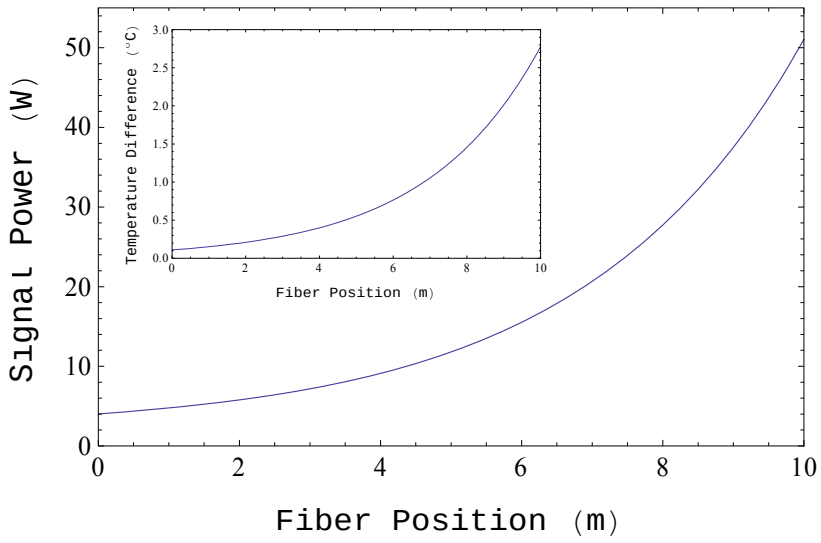

Fig. 18: Signal power and temperature difference as a function of longitudinal position in the fiber for a counter-pumped fiber amplifier at the SBS threshold.

The SBS threshold model of Nufern's amplifiers was then used to design the amplifiers for this work. The SBS-limited power obtainable under various pump geometries is shown in Fig. 19 with a seed power of 4 W. Longer fiber will absorb more pump power and increase the efficiency of the system. However, the SBS threshold

decreases with length, limiting the maximum amplified signal power. In addition, co-pumped fiber amplifiers are preferred to limit damage to the diode pumps, but result in a lower SBS threshold power for a given fiber length. For example, this work will have access to a maximum of 100 W from a single diode pump. With dichroic mirror losses, Fresnel reflections, and imperfect, free-space coupling to the fiber, an estimate of pump power coupled to the fiber is 75 W. In a co-pumped amplifier using 20/400, Yb fiber, the length of fiber must be kept to 5 m or less at this pump and signal power to avoid SBS. The shorter fiber length limits pump absorption and the expected output power is 50 W. In a counter-pumped architecture, the fiber length is limited to 8 m for an output power of 57 W. The counter-pumped amplifier increases amplifier efficiency by 15% in this case (57% optical-to-optical), but includes increase risk of diode damage due to amplified signal transmission through the dichroic mirror. If two diodes are available, the power of the amplifier can be increased to 82 W with dual-end pumping and a fiber length of 3.6 m limited by SBS. While this is the highest output power, it is the most inefficient (41% optical-to-optical) of the architectures due to coupling losses on both pumps combined with the shorter length of fiber to absorb the pump. Additional dichroic mirrors must be used in the counter-pumped and dual-pumped architectures, which decrease the efficiency further over what is presented in this example.

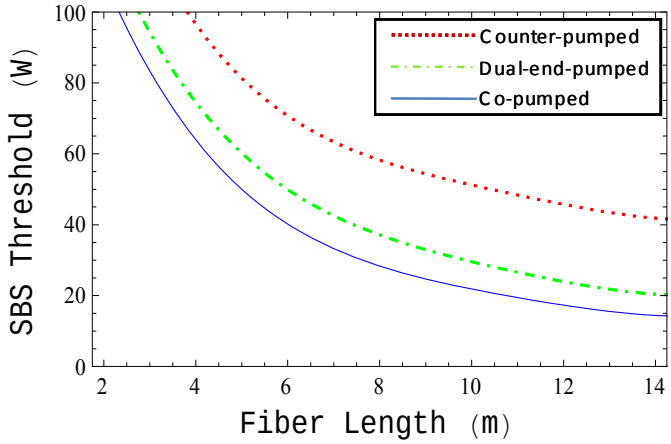

Fig. 19: Modeled SBS threshold power of fiber amplifier under different pump architectures.

A MOPA (Fig. 20) was designed and built using the model to generate high power with a narrow-frequency bandwidth while avoiding SBS. A 700 mW non-planar ring oscillator was the initial seed source. The linewidth is nominally < 5 kHz, much less than the Brillouin gain bandwidth of ~36 MHz. A preamplifier was constructed with 10.3 m of Yb-doped, PLMA (polarization-maintaining, large-mode-area) fiber counter-pumped with a 20-W, fiber-coupled diode at 976 nm. The output of the pre-amplifier was sent through a polarization-dependent, optical isolator to prevent feedback from the high-power amplifier. Polarization was maintained above 95% linearly polarized at an output power of ~5 W.

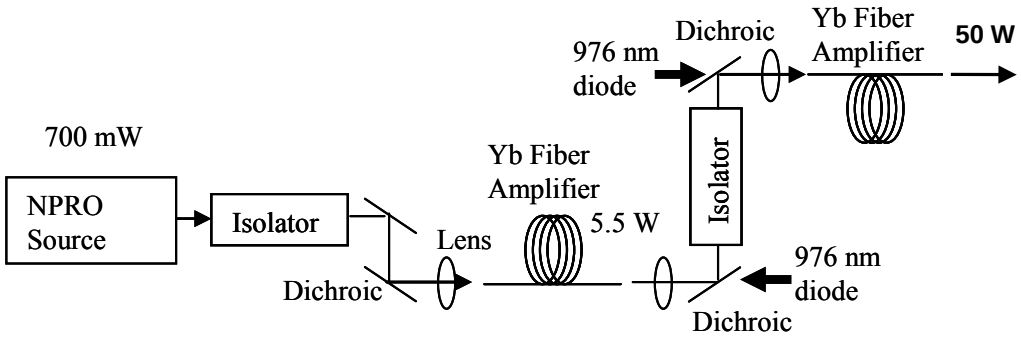

Fig. 20: Diagram of the MOPA constructed with a wavelength of 1064 nm.

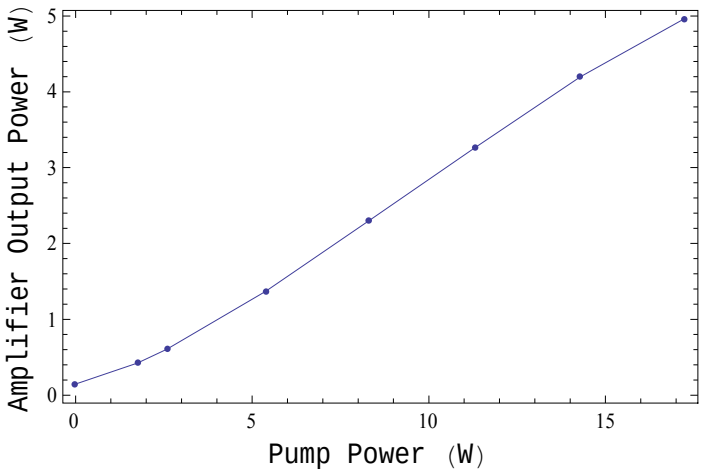

Fig. 21: 1064 nm pre-amplifier output power as a function of pump power.

The power amplifier was constructed to avoid SBS using a co-pumped architecture and a single, 100-W, fiber-coupled diode at 976 nm. The fiber length was cut to 5.2 m in accordance with the modeled SBS threshold. The output power is shown in Fig. 22 after an aperture to remove power in the cladding. The amplifier required periodic maintenance to maintain alignment, which resulted in variations in maximum output power achieved. This power was monitored during testing and was noted between 42 W and 50 W.

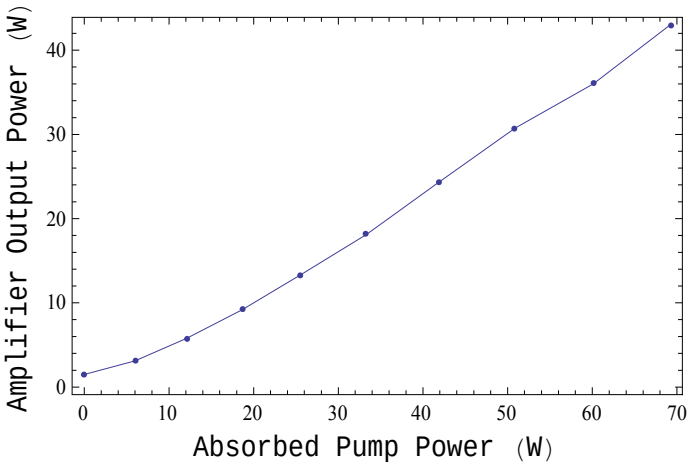

Fig. 22: 1064 nm amplifier output power as a function of absorbed pump power.

4.3.2. Erbium-Ytterbium Fiber Amplifiers

Fiber amplifiers from Nufern co-doped with erbium and ytterbium are used for amplification at 1550 nm wavelength.[149] Since ytterbium absorbs the pump power, the same diodes can be used for these amplifiers. The energy transfer of the excited energy state of ytterbium to the excited state of erbium is a non-radiative transition aided by the addition of phosphorus in the glass. Amplified spontaneous emission (ASE) and lasing of the ytterbium is a known problem with these fibers that must be overcome through proper fiber construction, high seed powers, and limited overall gain. Amplifiers have been constructed with gain higher than 20 dB,[150] but gain is typically limited to 15 dB by the onset of ASE around 1535 nm.[151] In addition, the large quantum defect between pump and signal wavelengths causes the efficiency of these amplifiers to be ~33%, less than half of a typical Yb-doped fiber. The thermal gradient along the length of the fiber is also higher. Due to these issues, SBS is less of a concern with Er-Yb fiber amplifiers, but still must be taken into account.

The SBS threshold was modeled in both single-mode and LMA fibers for the co-pumped orientation to find the minimum SBS threshold for a given length of fiber. The fiber characteristics are listed in Table 3. The SBS gain coefficients were determined using the NA-broadening equation (Eq. (2.58)) and an estimated peak gain coefficient of 3×10^{-11} m/W at low NA. Single-mode fiber is suitable for pre-amplifiers, and LMA fiber is needed for the high-power amplifiers. The SBS threshold as a function of fiber length for a single-mode amplifier is shown in Fig. 23, and the threshold power for an LMA fiber is shown in Fig. 24. With the pump power limited to 20 W and 100 W respectively in the pre-amplifier and high-power amplifiers, SBS threshold can easily be avoided.

Table 3: Er-Yb co-doped fiber characteristics.

	Single-mode	Large-mode-area
Core diameter (μm)	7	25
Core NA	0.17	0.10
Cladding diameter (μm)	130	300
Cladding Yb absorption (dB/m)	0.8 at 935 nm	2.0 at 976 nm
Fundamental mode $1/e^2$ diameter (μm)[a]	7.7	20
Seed power (W)	0.2	0.8
Slope efficiency (%)	32	32
SBS gain coefficient ($\times10^{-11}$ m/W)[b]	1.1	2.1

[a]Marcuse, D., *Loss analysis of single-mode fiber splices.* Bell Syst. Tech. J, 1977. 56(5): p. 703–718.
[b]This work

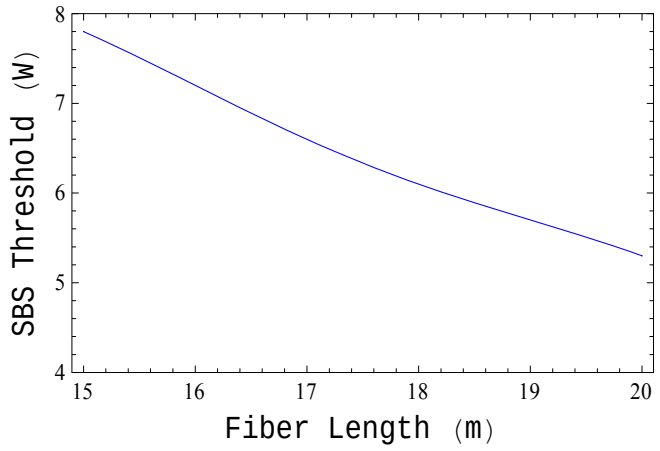

Fig. 23: SBS threshold of single-mode, Er-Yb fiber amplifier in co-pumped orientation.

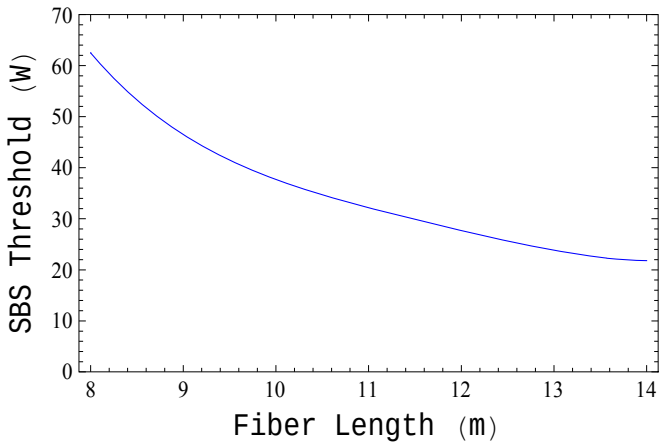

Fig. 24: SBS threshold of Er-Yb, LMA fiber amplifier in co-pumped orientation.

The seed used in the 1550 nm amplifier was a 10 mW New Focus Velocity laser, and was amplified up to 18 W through three fiber amplifiers. The apparatus diagram is shown in Fig. 25. The Velocity is an external-cavity diode laser with a nominal linewidth < 300 kHz. The Velocity laser output was sent through an optical isolator and an edge filter to prevent reflections and ASE from damaging the source laser. The edge filter was used because the isolators designed for 1550 nm may not suppress ASE at ~1060 nm.

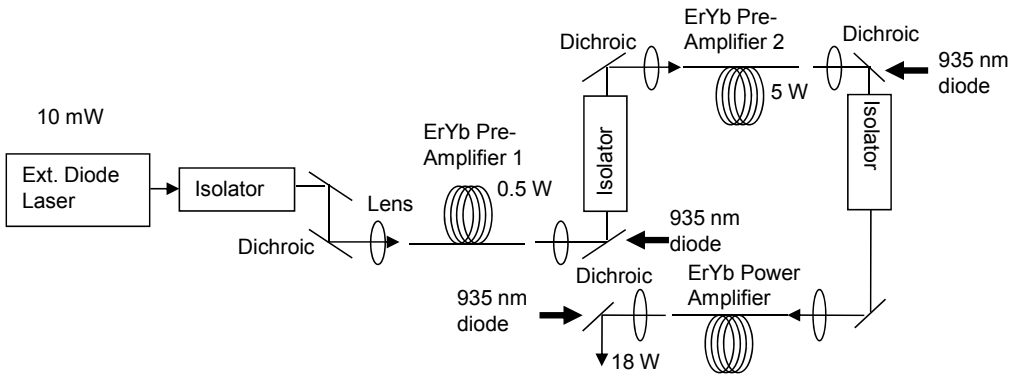

Fig. 25: MOPA constructed at a wavelength of 1550 nm.

The first stage amplifier consisted of 5 m of single-mode Er-Yb fiber, counter-pumped with a 20-W diode at 935 nm. The power limitation on the first stage amplifier was ASE in a 10 nm band around 1535 nm. With proper alignment, the first stage operates with > 95% linear polarization at 500 mW with ASE suppression better than -30 dB. ASE at 1060 nm was not present.

The second stage pre-amplifier consisted of 15 m of single-mode, Er-Yb fiber. The fiber was counter-pumped with a 20-W, fiber-coupled diode at 935 nm, and generated an output power of 3.38 W at 1550 nm (Fig. 28). The output power was

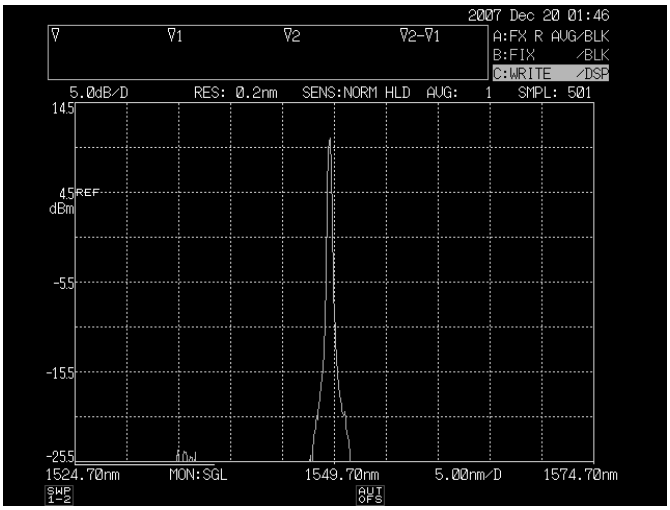

Fig. 26: Ando wavemeter image showing ASE suppression to -35 dB of the first stage Er-Yb amplifier. Output power was measured concurrently at 500 mW.

measured after the isolator, and therefore includes only a single polarization. The transmission through the isolators at 1550 nm was typically 95%. ASE near 1550 nm was suppressed to -25 dB (Fig. 27), while ASE at 1064 nm was measured at 263 mW from one end of the fiber. SBS threshold was not reached, as shown by the linear slope of the signal with pump power.

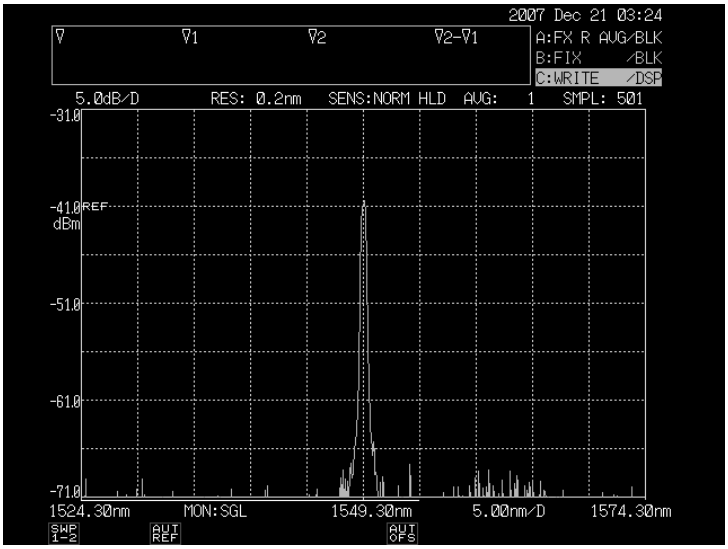

Fig. 27: Wavemeter showing low-ASE operation of 2nd stage amplifier at 1550 nm wavelength with 3 W output power.

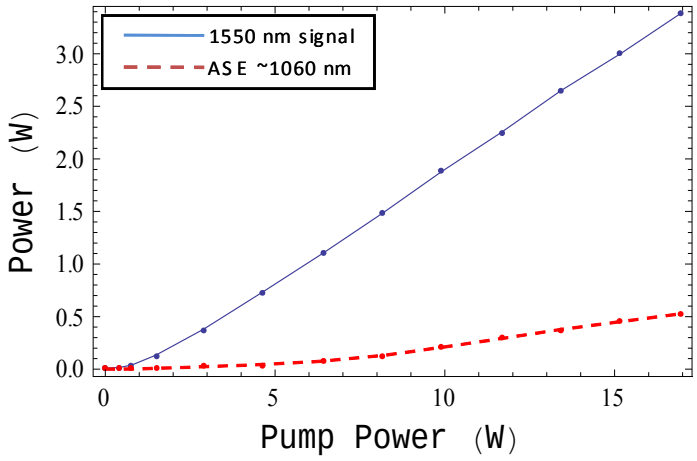

Fig. 28: Stage 2 amplifier at 1550 nm with ASE at 1060 nm.

Two dichroic mirrors were placed between the fiber and pump to protect the diode from the 1550 nm signal, and an additional dichroic was used to protect the diode from ASE at 1060 nm. In addition, a cladding-mode-stripper was added to the front end of the fiber. This consisted of a section of index-matching glue (Norland 61) applied directly to the cladding of the fiber. Preliminary tests were conducted on a fiber with a cladding diameter of 400 μm. With 4.5 cm of the cladding covered with glue, 95% of the power was removed from the cladding. This demonstrated that while the cladding-mode stripper was effective, the Norland 61 did not match the index of refraction of the cladding perfectly. From geometrical optics considerations, the effectiveness of the cladding-mode-stripper should increase with smaller cladding diameter, and also increase with higher NA. The cladding-mode-stripper removed all visible power guided by the cladding at a length of 2.8 cm on the 130-μm-diameter fiber.

The high-power amplifier at 1550 nm used a 125-W, fiber-coupled diode at 935 nm wavelength from Laserline. Due to the lower absorption at 935 nm, a fiber length of 18 m was used in a counter-pumped orientation. An output power of 18 W was observed with 90 W of pump power. A second test of this system is plotted in Fig. 29 and noted increasing ASE near ~1060 nm. SBS was not observed. In fact, for this fiber and orientation, the model predicts that for low enough seed power, SBS threshold cannot be reached. The large quantum defect causes a high thermal gradient along the length of fiber which suppresses SBS. With no pump power, SBS is expected at 28 W of seed from the Smith equation. As pump power is increased to 20 W, the threshold of SBS would no longer be exceeded with a 28 W seed, and the output power would have

increased to 33 W. Further increases in pump power cause a continual decline in SBS gain. For decreased seed powers below 25 W, SBS threshold would never be reached.

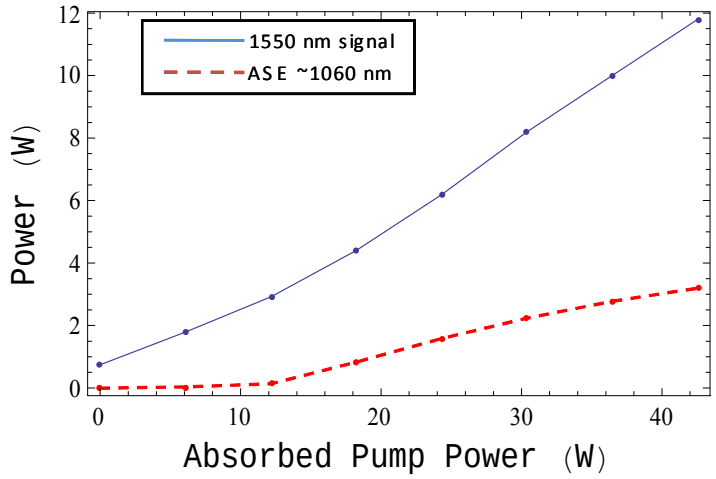

Fig. 29: 3rd stage amplifier at 1550 nm output power and ASE at ~1060 nm.

4.3.3. Tellurite Fiber Amplifier

Unlike the fiber amplifiers above, a tellurite glass fiber doped with ytterbium was designed and purchased from NP Photonics specifically to lower the SBS threshold. This amplifier was purchased as a candidate to produce phase conjugation instead of the previous amplifiers which were designed to amplify the seed. The manufacture of tellurite glass fiber is immature, and the fibers produced have an unpredictable scattering loss up to 3 dB/m. The goal was to overcome scattering losses by adding gain to the fiber. A multi-mode fiber was designed for a cladding absorption of 3+/-1 dB/m using Beers Law absorption and measurements of the absorption cross-section of Yb in tellurite glass.[116] The fiber had a core diameter of 25 μm and an NA of 0.22.

A cutback test was performed on the fiber to determine the effective pump absorption and scattering loss in the fiber at 1064 nm. The scattering loss was assumed

to be the same in both the core and cladding. Since the absorption of ytterbium is different for the core-launched signal at 1064 nm and the cladding-launched pump at 976 nm, the cutback test was analyzed using the fiber amplifier model to decouple the effects. The total attenuation of the signal was measured at $2.1 +/- 0.3$ dB/m, while the attenuation of the pump was $3.8 +/- 0.3$ dB/m. The signal power as a function of fiber length was modeled and shown in Fig. 30. With scattering and absorption losses as fit parameters in the model, the loss in the tellurite was determined to be $2.0 +/- 0.2$ dB/m with a pump absorption of $2.0 +/- 0.2$ dB/m.

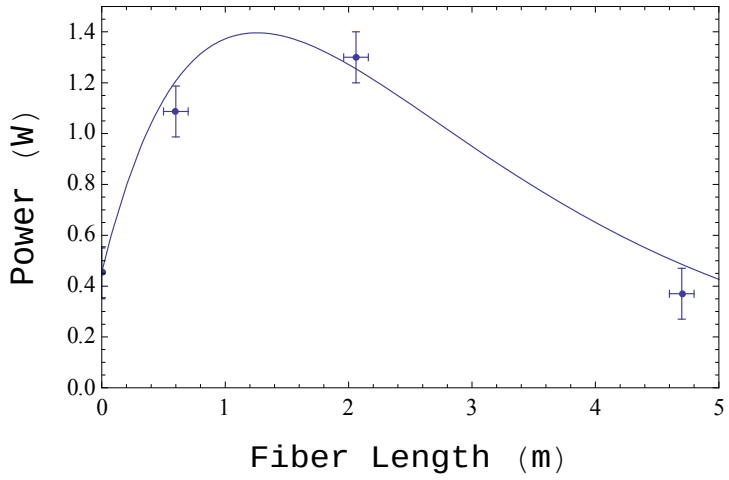

Fig. 30: Seed power as a function of length measured (data points) and modeled (solid curve) in a tellurite amplifier.

As discussed in Section 3.3.4, the Brillouin gain coefficient of tellurite has been measured several times by three different research groups. The SBS gain coefficient in tellurite fiber can be determined from these experiments as a function of the NA of the fiber. Using the measured SBS threshold power from the fiber experiments, the gain coefficient was determined from the SBS threshold model and plotted along with the expected gain broadening curve from Eq. (2.58) in Fig. 31. The curve yields a value for

the gain coefficient in bulk tellurite of ~0.95x10^{-9} m/W, which is similar to the value measured by Dubinskii *et al.*[152]

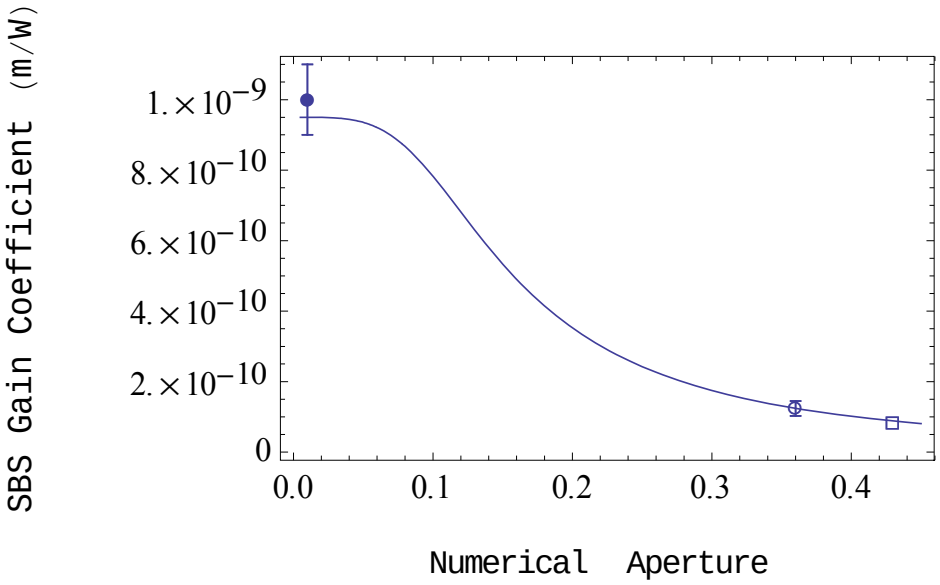

Fig. 31: SBS gain coefficient of tellurite plotted as a function of numerical aperture. Experimental measurements from Dubinskii (solid circle), Abedin (hollow circle), and Qin (square) are shown.

The model was used to calculate the SBS threshold of the tellurite amplifier. The SBS gain coefficient of the fiber is expected to be 3.0×10^{-10} m/W from the gain broadening curve in Fig. 31. The high scattering loss acts on both the signal and the pump to reduce the interaction length for SBS. In this case, the co-pumped orientation has a higher SBS threshold than dual-end pumping. The calculated SBS threshold for a tellurite amplifier that has a length of 5 m is plotted in Fig. 32. Due to the scattering loss, significant seed and pump powers must be launched into the fiber to achieve SBS threshold. For pump powers below ~40 W, the high scattering loss negates the amplification from the counter-pumping diode. For pump powers higher than 40 W, the signal power remains high in the fiber due to the amplification from the counter-pumped diode overcoming the scattering loss.

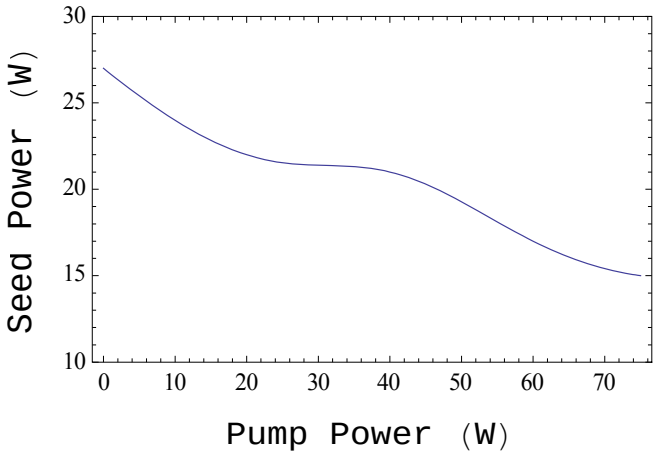

Fig. 32: Calculated SBS threshold of a dual-end-pumped tellurite amplifier.

4.4. Passive Fiber SBS Threshold

As shown above in Fig. 32, the fiber amplifier model with no pump power can be used to calculate the SBS threshold of a passive fiber. The SBS threshold was calculated for two different wavelengths for tellurite and chalcogenide fibers since these fibers exhibit significantly lower scattering losses near 1550 nm and beyond. In addition, the SBS threshold was measured and calculated for silicate fiber as a function of fiber length. The threshold model was used in this section to evaluate whether SBS threshold could be reached in these fibers using the amplifiers discussed above.

4.4.1. Silicate Fiber

Due to its availability, low cost, and low attenuation, the most common fiber used in phase conjugation experiments is commercial, silicate fiber. The Brillouin gain coefficient is an order of magnitude lower than tellurite. However, it has negligible scattering loss at the lengths important for phase conjugation and has a high damage threshold. With the fiber amplifier sources above, this work is limited to ~40 W of power

to generate SBS threshold. Phase conjugation requires a multimode fiber, but the SBS threshold increases with core area. The number of modes supported by a fiber increases with the normalized frequency parameter of the fiber, given by

$$V = \frac{2\pi}{\lambda} a(NA), \tag{4.9}$$

where a is the radius of the fiber core.[153] The number of modes can be increased by increasing the core radius, the NA, or decreasing the wavelength. By examination of Eq. (2.65), a fiber with a low NA is predicted to produce an equivalent phase conjugation fidelity as a shorter fiber of similar material with a higher NA. In addition, the SBS gain coefficient is expected to be lower in a fiber with a higher NA due to gain broadening.

With these factors, two commercially available fibers were chosen for further examination. Both of the fibers support a similar number of modes as shown in Table 4. Including the scattering losses, the predicted SBS threshold power is plotted as a function of fiber length in Fig. 35.

Table 4: Passive silicate fiber parameters at 1.064 µm wavelength.[153]

	0.13 NA fiber	0.06 NA fiber
Core diameter (µm)[a]	20	40
Core NA[a]	0.13	0.06
Core attenuation (dB/km)[a]	2	7
Cladding diameter (µm)[a]	125	400
V parameter	7.7	7.1
Fiber ~M^2 (V/2)	3.8	3.5
Supported modes[b]	34	30

[a] Manufacturer supplied, CorActive
[b] Adams, M.J., *An introduction to optical waveguides*. 1981: Chichester: Wiley.

The SBS threshold was measured for these two fibers each at a length of 100 m. The threshold of the fiber with an NA of 0.13 was measured three times at this length.

The fiber was polished at an 8º angle on both sides to eliminate Fresnel reflections from interfering with measurements of the Stokes power. A pickoff was used to measure the incident and reflected powers, and the power transmitted through the fiber was measured. The cladding of the fiber had a high attenuation such that only the core-coupled power was measured at the output. The coupling efficiency was measured below SBS threshold by measuring the transmitted power as a function of incident power and taking into account transmission loss and Fresnel reflections. This coupling efficiency was assumed to be constant as the SBS threshold was exceeded, and allowed the computation of coupled power throughout the test. The SBS threshold was then determined using linear regression of the Stokes power and is plotted in Fig. 33. The threshold was $4.66 +/- 0.51$ W, with the error given by the standard error of the linear fit, which corresponds to a Brillouin gain coefficient of $(1.47 +/- 0.17) \times 10^{-11}$ m/W .

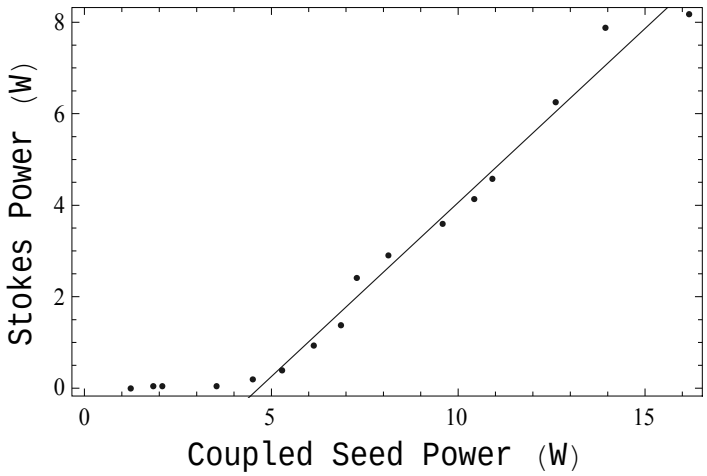

Fig. 33: Plot of Stokes power as a function of coupled power into a 100-m fiber with NA of 0.13.

Similar measurements were made with the 0.06-NA fiber at a length of 100 m as shown in Fig. 34. The SBS threshold was determined to be $6.9 +/- 1.4$ W , which yields

a Brillouin gain coefficient of $(4.33+/-0.88)\times10^{-11}$ m/W. Using these experimental measurements, the expected SBS threshold of the silicate fibers as a function of fiber length are shown in Fig. 35.

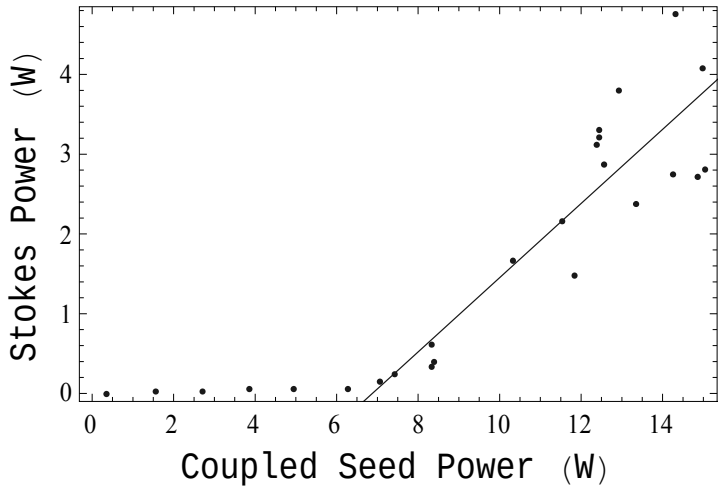

Fig. 34: Plot of Stokes power as a function of coupled-seed power in 100 m of 0.06-NA fiber.

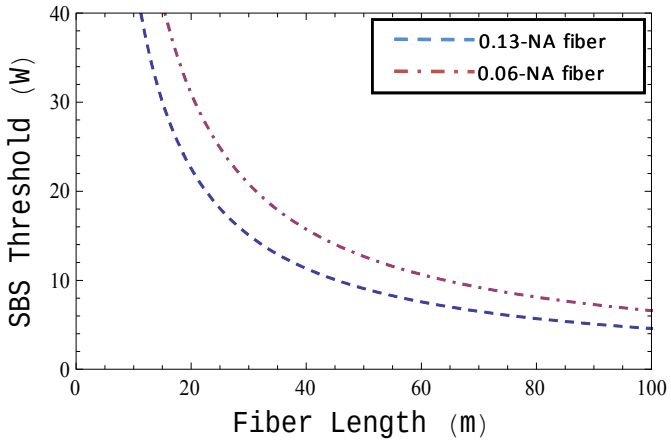

Fig. 35: Calculated SBS threshold as a function of fiber length for the two silicate fibers.

The Brillouin gain coefficient in optical fiber is expected to decrease with numerical aperture as discussed in Section 2.3. Equation (2.58) describes the broadening

of the Brillouin gain coefficient with fiber numerical aperture, and is plotted in Fig. 36 along with the measured values of the Brillouin gain coefficient in the 0.06-NA fiber and 0.13-NA fiber. Considering that the fibers were manufactured with different amounts of core dopants, a reasonable agreement with Eq. (2.58) was obtained.

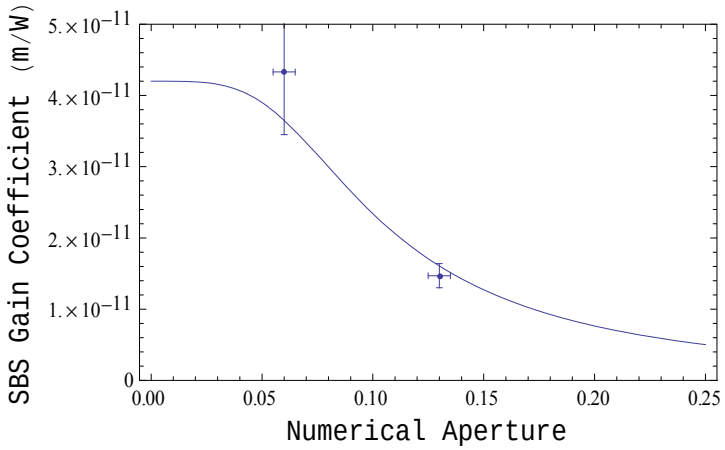

Fig. 36: Brillouin gain coefficients measured in 100-m silicate fiber plotted as a function of numerical aperture. The theoretical curve of the Brillouin gain coefficient of silicate fiber due to numerical aperture broadening is also shown.

4.4.2. Tellurite fiber

The SBS threshold was also modeled in undoped, tellurite fiber. The scattering loss was measured in a 15-m length of tellurite fiber to be ~0.7 dB/m at a wavelength of 1550 nm. The tellurite fiber has an NA of 0.22, and accepts an approximate beam quality of $M^2 \approx 5.6$. A scattering loss of 2.0 dB/m was also modeled to investigate the effects of scattering loss as measured in the Yb-doped, tellurite fiber at 1064-nm wavelength. At 0.7 dB/m of scattering loss, the difference between the model in this work and Smith's model are clearly visible as shown in Fig. 37. For scattering losses of 2 dB/m, the error in Smith's model is significant.

According to the manufacturer, the optical damage threshold of tellurite fiber is similar to silicate fiber.[154] During tests of the fiber, poor cleaves would result in

melting of the fiber tip. However, when the tip was properly prepared, the damage threshold was higher than 15.5 MW/cm^2 . The damage threshold in silicate fiber also depends on the surface quality and has been shown to exceed 100 MW/cm^2.[155]

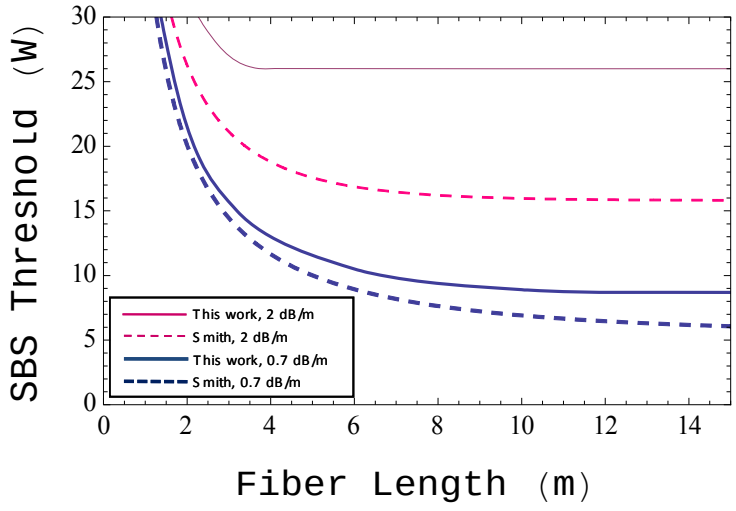

Fig. 37: Modeled SBS threshold of passive tellurite fiber as a function of fiber length for scattering loss of 2 dB/m and 0.7 dB/m. The Smith model prediction is also shown (dashed).

4.4.3. Chalcogenide Fiber

SBS threshold was reached in chalcogenide fiber by two different research groups as mentioned earlier. Abedin measured the threshold in single-mode fiber with a 0.18 NA with a length of 5 m. Two fibers were purchased from the same manufacturer as Abedin. The first was a single-mode fiber, 1.7 m long. The second was 24 m in length, and multimode for phase conjugation experiments. Both fibers had an NA of 0.18, but the multimode fiber had a 65 μm core diameter, while the single-mode fiber was 6 μm in diameter.

The single-mode chalcogenide fiber was tested for transmission loss and damage threshold at both 1064 and 1550 nm wavelengths. At 1064 nm, chalcogenide fiber has a very large attenuation of ~10 dB/m, and the damage threshold was less than 50 kW/cm^2.

At 1550 nm, the attenuation was $1.3+/-0.1$ dB/m, and the highest damage threshold observed was 400 kW/cm^2. The highest reported irradiance in a single-mode, chalcogenide fiber is 221 kW/cm^2.[25]

Using the experimental data from Abedin, the SBS gain coefficient was calculated using this work's model at 3.55×10^{-9} m/W for a fiber with an NA of 0.18. This is approximately two orders of magnitude higher than the gain coefficient of silicate fiber. At 1550 nm, the transmission loss of the multimode chalcogenide fiber was measured at 0.33 dB/m, and the damage threshold was found to be less than 50 kW/cm^2. The threshold power was calculated as a function of fiber length, and is shown in Fig. 38, along with the highest reported irradiance.

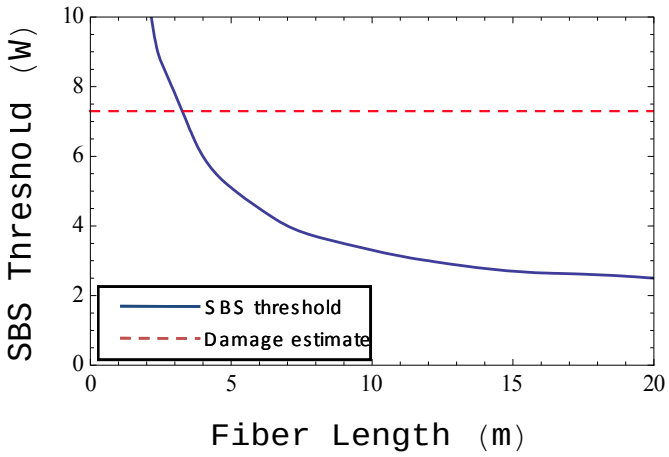

Fig. 38: Multimode chalcogenide fiber SBS threshold as a function of fiber length for a wavelength of 1550 nm with estimated damage irradiance (dashed).

4.5. Conclusion

The SBS threshold model aided in the design of source amplifiers while avoiding SBS and predicted achievable thresholds in fibers for phase conjugation research. Amplifiers were designed and built with the aid of this model to avoid SBS and generate up to 50 W in a single-frequency beam a 1064 nm and 18 W at 1550 nm. Without

approximations for low scattering losses, the accuracy of SBS threshold calculations was improved over the Smith model. In addition, the effects of scattering losses were observed to severely limit the effective length of high-loss materials: after a relatively short length of 10 – 20 m, longer lengths fail to reduce threshold. While novel fibers have one and two orders of magnitude higher Brillouin gain coefficients than silica, the scattering loss at a wavelength of 1064 nm prohibits reaching SBS threshold in chalcogenide fiber while raising the threshold power significantly in tellurite. Taking into account the lower efficiency amplifiers at 1550 nm, tellurite and chalcogenide fibers are not predicted to show a decline in phase conjugation fidelity with length as well as the silicate fibers at 1064 nm.

5. Fidelity Measurement Techniques

5.1. Overview

Phase conjugation fidelity is the fraction of the Stokes beam that is the phase conjugate of the seed or SBS pump. If the seed beam includes multiple transverse modes, then the perfect phase conjugate beam will include the same transverse modes propagating in the opposite direction. Phase conjugation is typically employed to recreate a single-mode beam at the diffraction limit. Therefore, divergence and beam quality measurements both before and after phase conjugation have been used as a measure of fidelity. Similarly, the beam quality has been measured by the power transmission through a pinhole aperture on portions of the beam. An improvement on this technique places the pinhole aperture in the main beam, and therefore verifies not only the maximum waist size of the Stokes beam, but also the direction of propagation. These methods provide a measure of fidelity that can be highly accurate in determining whether high-fidelity, phase conjugation has occurred, but the results are increasingly ambiguous as fidelity decreases. There can always be some transmission through a pinhole, even for very poor quality beams. If beam cleanup occurs instead of phase conjugation, the result is a low-order-mode beam, typically LP_{01}, which has excellent beam quality and low divergence. While high beam quality is the goal of many phase conjugate systems, coherent beam combining through phase conjugation requires a more rigorous approach.

In this chapter, a new measure of phase conjugation fidelity is devised and tested which is applicable to coherent beam combining by measuring the fringe visibility of interfered beams. The results of this method are compared to those achieved through other methods by using a long, graded-index fiber to generate the Stokes beam. In long, graded-index fiber, stimulated Brillouin scattering has been reported to produce continuous wave (CW) phase conjugation.[105, 156] Conversely, it is also reported to produce a pure fiber mode regardless of pump mode structure.[64, 65, 97, 157, 158] This process is referred to as beam cleanup. These results are contradictory, but can be attributed to the methods used to measure fidelity. In this work, the Stokes reflection from the graded-index fiber is shown to be beam cleanup, and the measurements of fidelity are compared using their ability to distinguish beam cleanup from phase conjugation.

5.2. Beam Quality Methods

Improving beam quality is the goal of many phase conjugation experiments. The earliest phase conjugation experiments set a standard for measuring phase conjugation by intentionally distorting the input beam.[53, 66] The input beam was spatially filtered or was otherwise near the diffraction limit before propagating through a piece of acid-etched glass or an imperfect amplifier. The distorted beam then reflected off the phase conjugate mirror back through the aberration (see Fig. 39). Measures of beam quality are made on the input beam both before (position A in Fig. 39) and after (position B in Fig. 39) the aberration to quantify the degree of distortion. After reflection from the phase conjugate mirror, the beam quality is sampled again both before (C) and after (D) the

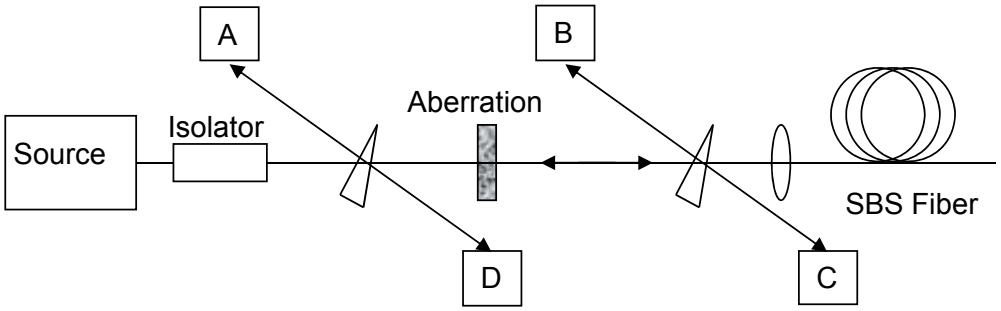

Fig. 39: Typical apparatus diagram for measuring fidelity of phase conjugation using beam quality techniques.

aberration to show improvement. Often, the phase conjugate mirror is replaced with a standard mirror to show the beam distortion induced by two passes through the aberration. The fidelity of phase conjugation is measured as a ratio of the initial beam quality at A to the final beam quality at D after the second pass through the aberration. As a variation of this approach, no external aberration is used, and the fiber where SBS is generated is considered the aberration itself. The beam quality measures used to compare the initial and final beams are beam divergence measurements, M^2 measurements, and pinhole transmission.

5.2.1. Divergence Measurements

As discussed in Chapter 3, Zel'dovich *et. al* used divergence measurements to verify phase conjugation in the earliest phase conjugation experiment.[53] A single pass through an aberration resulted in an increase in divergence from ~1 mrad to 3.5 mrad. The beam was restored to the initial divergence after the second pass through the aberration via SBS, but a second pass using a normal mirror resulted in a divergence of ~6 mrad.

This example shows that when fidelity is high and the induced aberrations are substantial, the divergence measurement is ample verification of phase conjugation fidelity. When fidelity declines, this measurement becomes more ambiguous. In the example above, for instance, the standard mirror could be claimed to generate a phase conjugation fidelity of 0.17. By varying the aberration induced on the incident beam, this "fidelity" could be increased further.

As the fidelity declines, the Stokes beam direction is no longer the exact opposite of the seed. The divergence technique ignores this distinction and makes no measure of propagation direction. Since the direction of propagation is different than the input beam, the distortion imparted to the beam by the aberration is not controlled. It is possible that the aberration induced on the reflection is different from that of the incident beam, which further reduces the accuracy of this method.

In the event of SBS beam cleanup, the Stokes beam can exist entirely in the fundamental mode regardless of the seed input, as in Fig. 40. In this example, the seed beam was wavefront split into two semicircular beams. The beams were then tiled together as shown in Fig. 40(a) before being coupled into a 2.5-km-long, multimode, graded-index fiber. The Stokes reflection is shown in Fig. 40(b) with a Gaussian-like irradiance pattern. The waist of the Stokes beam is determined by the fiber independently. If the induced aberration is low, and the coupling is carefully chosen to match that of the fundamental mode, the resulting beam would nearly match the divergence of the input and erroneously register a fidelity near one.

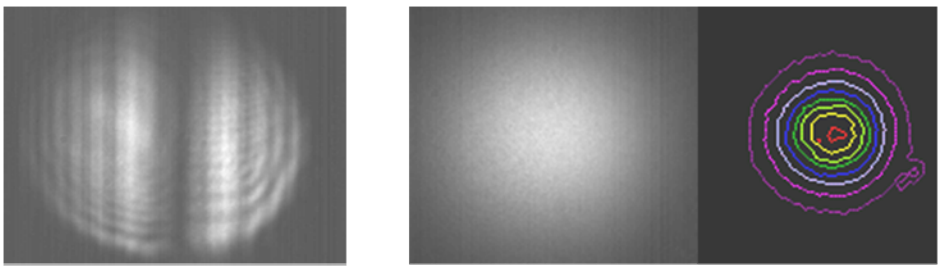

Fig. 40: Example of SBS beam cleanup. Irradiance images show (a) the incident beam comprised of two wavefront-split Gaussian beams and (b) the Stokes reflection from SBS in a graded-index fiber.

Perhaps the largest source of error is due to the beam quality of the Stokes reflection. Since SBS beam cleanup produces good beam quality regardless of seed beam quality (as in Fig. 40), the resulting beam has only been distorted once by the aberration. This can account for the improved beam quality of the Stokes reflection over that from a standard mirror as shown in Fig. 41(c) and (d). [100] In this experiment, a long, graded-index fiber was used to generate the SBS reflection and phase conjugation was claimed. However, these images alone are insufficient to prove phase conjugation. According to typical practices, Fig. 41(c) should be comparable to Fig. 41(a). The center lobe of (c) is similar to (a), but there is no measurement of the power in the sidelobes of (c). There is also no measure of the direction of propagation of the (c) as compared to the input beam, and therefore the aberration experienced by the reflection may be different from that of the incident beam. No image of a single pass through the aberration was provided to compare to (c). Instead, a double-pass through the aberration is given in (d), which exaggerates the effect.

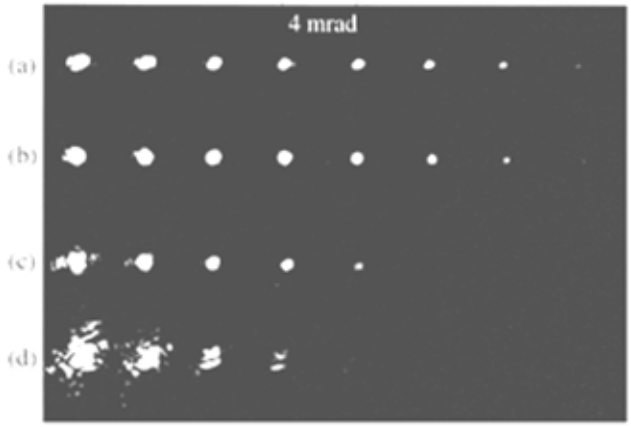

Fig. 41: Irradiance images at decreasing exposure levels of (a) the incident beam, (b) the Stokes reflection without distorting object, (c) the Stokes reflection with distorting object, and (d) the reflection from a standard mirror through the distorting object.[100]

5.2.2. M^2 Measurements

As a slight improvement on the divergence measurements, some researchers have measured the beam quality to determine the fidelity of phase conjugation.[105] Fidelity in this case was defined to be the improvement in M^2 due to the aberration acting on the Stokes beam divided by the decline in M^2 measured as the seed passes through the aberration. With reference to Fig. 39,[105]

$$F = \frac{M_C^2 - M_D^2}{M_B^2 - M_A^2}, \tag{5.1}$$

where M_A^2 represents the beam quality at position A of Fig. 39. However, if $M_D^2 \geq M_C^2$, the fidelity is defined as zero. Therefore, if the aberration fails to improve the beam quality of the Stokes beam, the fidelity is set to zero.

This method addresses the main issue raised in the previous section. It automatically negates a Stokes beam that is not improved in beam quality after passing through the aberration, which was a main problem with the divergence method. Beam

cleanup is seemingly elimated by this step. However, there is no measurement of the propagation direction of the Stokes beam. A phase conjugate beam would propagate in the opposite direction as the seed. As fidelity declines, the aberration affecting the Stokes beam may not be the same as the distortion on the incident beam.

In addition, the measurement of beam quality is susceptible to errors. An international standard describes the process for measuring the beam waist and divergence along two principal axes using a focusing optic and camera system.[159] As stated in the standard, "Noise in the wings of the power density distribution . . . may readily dominate the second order moment integral." The correct values of background noise reduction and cross-sectional integration limits must be chosen carefully to yield accurate results.

Using a long, graded-index fiber to generate SBS, Mocofanescu *et al.* measured a phase conjugation fidelity of 0.31 using this technique.[105] In a second trial with the same fiber, the measurements were set to zero due to beam cleanup. The measurements from the same fiber over the range of 0 to 0.31 in fidelity demonstrate the error in this technique.

5.2.3. Pinhole Transmission

The technique used by Eichler and described in Chapter 3 was referred to as a "power-in-the-bucket" technique. The fidelity is measured by first recording the transmission of the incident beam through a focusing lens and aperture on a pickoff from the main beam (see Fig. 10 and Chapter 3 for a more thorough description). The fiber itself is used as the aberration to the seed beam, and the Stokes beam transmission through the same or similar lens and aperture system is recorded. The fidelity is determined as the Stokes transmission divided by the incident beam transmission.

The fidelity measured using a pinhole measurement loses validity as the fidelity declines. Even a very poor quality beam will have some transmission through a pinhole, so the fidelity will never be zero. A Stokes beam generated through beam cleanup can increase this error. There is also no measure of the direction of propagation on the Stokes beam with relation to the incident beam. As a result, the pinhole can be aligned to maximize the transmission of the Stokes beam, further improving the fidelity measure in the event of beam cleanup. The method is also susceptible to small errors which can occur during the optimization of transmission through a pinhole.

Using this technique, the parameters of the seed beam and size of the pinhole becomes very important for distinguishing beam cleanup from phase conjugation. Consider the case that the parameters of the incident beam are set to match the beam diameter of the fiber fundamental mode. The pinhole would normally be chosen at 2 to 3 times the waist size to transmit 86% or 99% of the beam, assuming perfect beam quality and focusing optic. However, if beam cleanup occurs, nearly the same transmission would be achieved after optimizing the location of the pinhole on the Stokes beam pickoff. A fidelity of nearly one would be erroneously measured.

To minimize the errors in this approach, the beam must be coupled into the fiber at the highest accepted NA. The incident beam is therefore collimated at the largest diameter possible for the combination of fiber NA and coupling objective, and relates to the smallest diameter pinhole that can be used for a given lens. In the event of beam cleanup, the fundamental mode has a lower NA than the seed and a larger diameter at the fiber tip, which results in a larger beam diameter when imaged onto the pinhole. Low

measures of fidelity are still ambiguous, but beam cleanup can be eliminated from measurements of fidelity higher than a predictable value.

The technique can be improved by using an in-line pinhole as done by Kuzin *et al*.[60] and described in Chapter 3. The seed is focused through a pinhole before being coupled into the fiber where SBS is generated. This is the only technique discussed that provides a measurement of beam direction that is integral to the diagnostics system. Since the seed being coupled into the fiber passed through the pinhole, a perfect phase conjugate reflection would achieve 100% transmission back through the pinhole. This would be achieved regardless of exact fiber and pinhole alignment, provided perfect coupling efficiency into the fiber was maintained. In the event of beam cleanup, the measured transmission would vary with fiber alignment, with a maximum value set by the incident beam characteristics and pinhole size as discussed above. Low values of fidelity remain ambiguous, however.

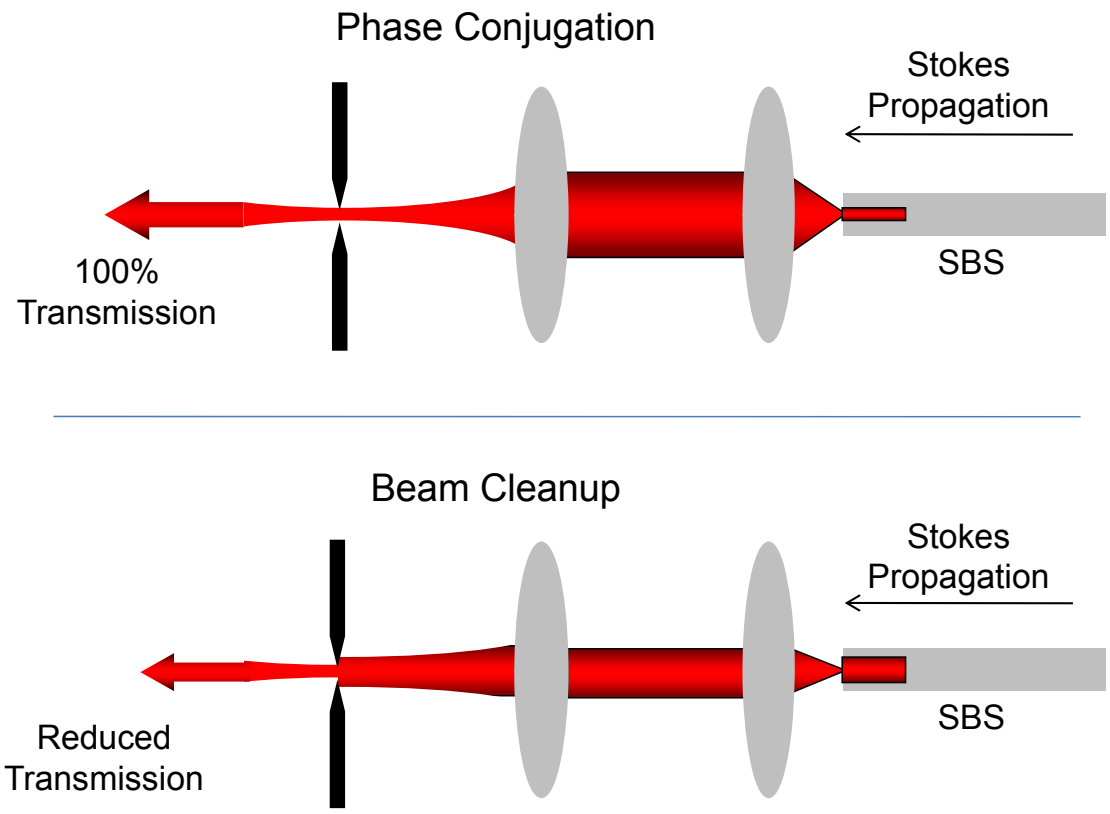

Fig. 42: Diagram depicting the distinction between phase conjugation and beam cleanup in pinhole transmission.[160]

An experiment was conducted to demonstrate the ability of the in-line pinhole to discriminate beam cleanup by generating SBS in a long, graded-index fiber with a core diameter of 50 μm and an NA of 0.21. The full beam was focused through a pinhole with 66% transmission before being coupled into the test fiber where SBS was generated, as shown in Fig. 43. Plano-convex lenses with focal lengths of 250 mm were used to focus the incident beam through the 300-μm-diameter pinhole and collimate the beam before coupling into the graded-index fiber. Wedged windows with one uncoated side were used to measure the power and to reflect a portion of the beam to a screen where the incident beam, the fiber transmission, and the Stokes beams could be simultaneously recorded. The fiber coupling lens was an asphere with a focal length of 6.2 mm.

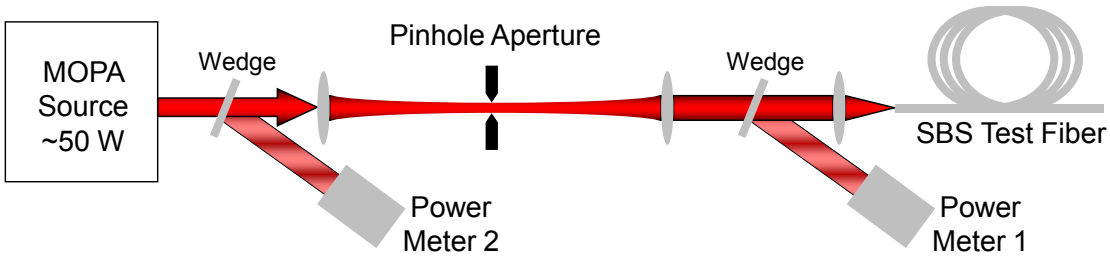

Fig. 43: Diagram of the experiment to distinguish phase conjugation from beam cleanup using an in-line pinhole.[160]

As a preliminary test, the fiber tip of the graded-index fiber was translated while maintaining good coupling efficiency. A perfect phase conjugate reflection would propagate along the direction opposite the seed regardless of small changes in fiber position. However, the Stokes reflection from the graded-index fiber visibly moved across the screen as the fiber tip was translated by 25 μm. Fig. 44 shows the displacement of the Stokes beam at the extremes of the fiber tip translation. The incident, Stokes, and fiber transmission images were collected simultaneously by imaging each beam as reflected off a screen. The screen reflection caused speckle in the images which was filtered out using 6-pixel averaging. Also apparent in the figure is the higher divergence of the Stokes beam as compared to the seed. In the upper right of each image, the transmission through the fiber is shown, and it is apparent from those images that many modes were exited in the fiber. The input signal in the upper left was clearly aberrated by propagation through the fiber.

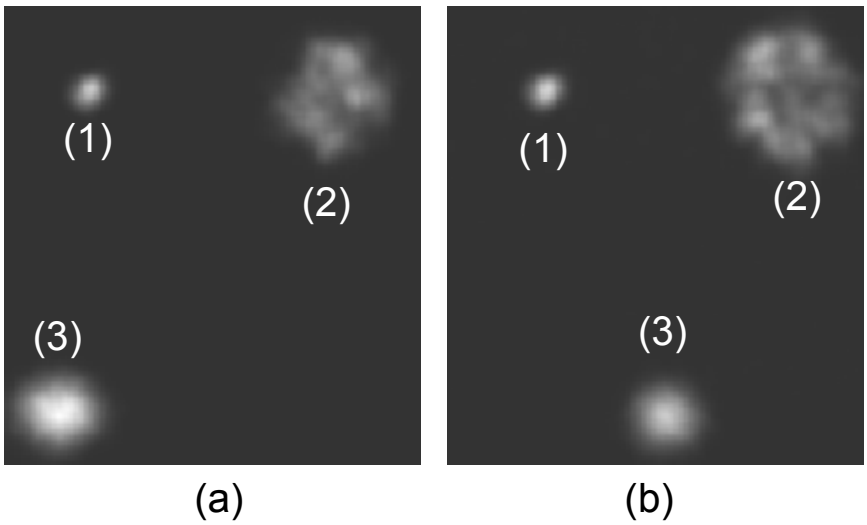

Fig. 44: Irradiance images of (1) the seed beam, (2) the beam transmitted through the test fiber, and (3) the Stokes beam using a long, graded-index fiber to generate SBS. The fiber tip was translated by 25 µm between image (a) and (b).

The transmission of the Stokes beam through the pinhole was measured to quantify this effect and show the distinction between phase conjugation and beam cleanup. The optics were chosen to image the pinhole onto the fiber tip with a magnification such that the pinhole image diameter was much less than the fiber core diameter. The pinhole image diameter on the fiber tip was calculated at 8.7 µm, limited by the test fiber NA. Using an approximation for the Gaussian beam diameter of the fundamental mode in a graded-index fiber,

$$\omega = a\left[\sqrt{\frac{2}{V}} + \frac{0.23}{V^{3/2}} + \frac{18.01}{V^{6}}\right], \tag{5.2}$$

the fundamental mode diameter of the fiber is calculated at 12.9 µm.[21] The transmission of such a Gaussian beam with diameter of 12.9 µm through a circular aperture with a diameter of 8.7 µm was calculated at 60% provided the beam is centered on the pinhole. An off-center beam would have lower transmission.

The fiber tip was once again translated a total displacement of 25 μm in increments of 2.5 μm. SBS was generated in the fiber, and the Stokes transmission through the pinhole was recorded as a function of fiber displacement. The pinhole transmission was measured as the ratio of Power Meter 2 to Power Meter 1 as shown in Fig. 43, calibrated by taking measurements with no pinhole in place. The data is plotted in Fig. 45. After the pinhole transmission was recorded, the fiber was cut to ~3 m and the fiber transmission was recorded over the same incremental displacements to measure the coupling efficiency. The coupling efficiency is also shown in Fig. 45. The pinhole transmission is shown to match the calculated pinhole transmission of a Gaussian approximation of the fundamental mode through the image of the pinhole aperture at the fiber tip, which is shown as a continuous curve. In the calculated transmission curve, the coaxial position was chosen at a displacement of 15 μm to match the experimental data.

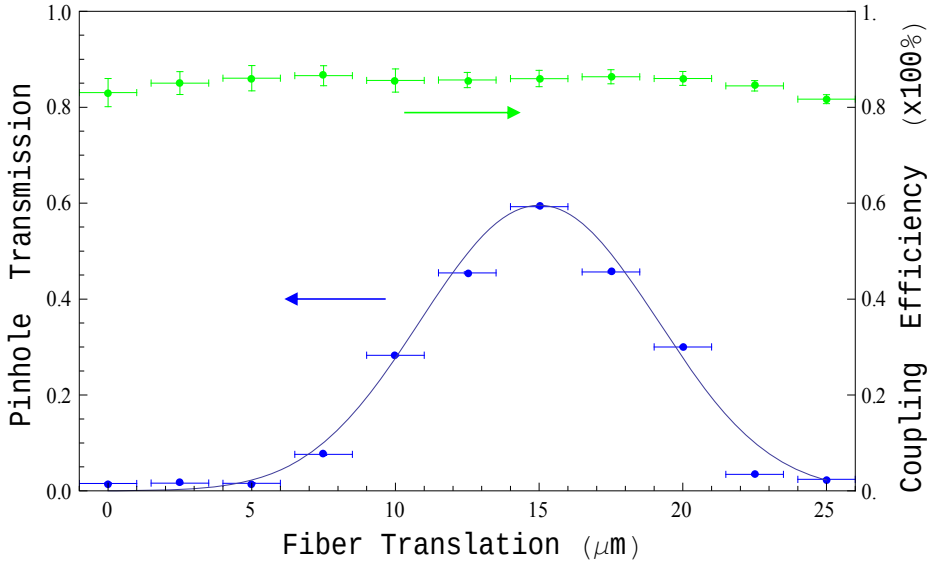

Fig. 45: Pinhole transmission of the Stokes beam and coupling efficiency of the seed are shown as a function of fiber tip translation. The calculated transmission of the fundamental mode of the fiber through a circular aperture is also shown.[160]

These results verify the ability of the in-line pinhole technique to distinguish beam cleanup from phase conjugation. Based on the fundamental mode diameter and the pinhole, a maximum transmission due to beam cleanup can be determined. Transmission higher than this value indicates phase conjugation, while pinhole transmission below this value remains ambiguous. The fundamental fiber mode in this experiment was limited to ~60% transmission, while a perfect phase conjugate of the seed would achieve up to 100% transmission. Furthermore, controversy remains over the ability of a graded-index fiber to generate a phase conjugate beam as discussed in Chapter 2. Viewed from this perspective, these results show that beam cleanup occurs in a long, graded-index fiber and not phase conjugation.

5.3. Interference Method

For laser systems where improving the far-field irradiance is the goal, the previous methods of measuring fidelity are accurate. When an improvement in beam quality is desired, using beam quality as a diagnostic is adequate. However, coherent beam combination via SBS requires the spatial coherence among multiple beams, and a new measure of fidelity is warranted.[161] In this section, a new method of measuring fidelity using the visibility of interference fringes is described and tested. In this case, the ambiguity which arises from beam quality techniques is removed.

In this work, a seed beam was split into two paths before both beams were coupled into the same graded-index fiber. Phase locking between two beams via SBS beam cleanup was directly measured using lateral shearing interferometers (LSIs) immediately after the Stokes reflection exits the fiber. Another LSI was used to measure the coherence after the Stokes beam travels back through the two beam paths. The

degree of coherence at this LSI is a more accurate measure of fidelity which extricates the measurement of phase conjugation from calculations of beam quality. Although the use of LSIs to measure beam phasing is not unique to this experiment, this is the first time it is used to determine the relative phase characteristics of two tiled beams at locations critical to both beam cleanup and the fidelity of phase conjugation. This measurement directly determines the relative phase of the two beams without the added complexity of a beam quality measurement. From this data, a clear determination of spatial coherence, fidelity of phase conjugation, and beam phasing can be made.

5.3.1. Apparatus

The apparatus is shown in Fig. 46. The MOPA source laser was described in Chapter 4, and is summarized here. It consisted of an external cavity diode laser operating at 10 mW (1550 nm) followed by a 2-stage fiber amplifier. The first fiber amplifier was 5 m of Nufern's Er-Yb, co-doped 7/130 polarization maintaining fiber counter-pumped with a 20 W LIMO fiber-coupled diode at 935 nm. The output of the first stage was ~500 mW with ASE suppressed to -36 dB. The second stage was 15 m of the same fiber, co-pumped with another 20-W LIMO fiber-coupled diode at 935 nm. Free space coupling was used and the fiber ends were polished at 8°. The 2-stage amplifier produced an output power of up to 5 W.

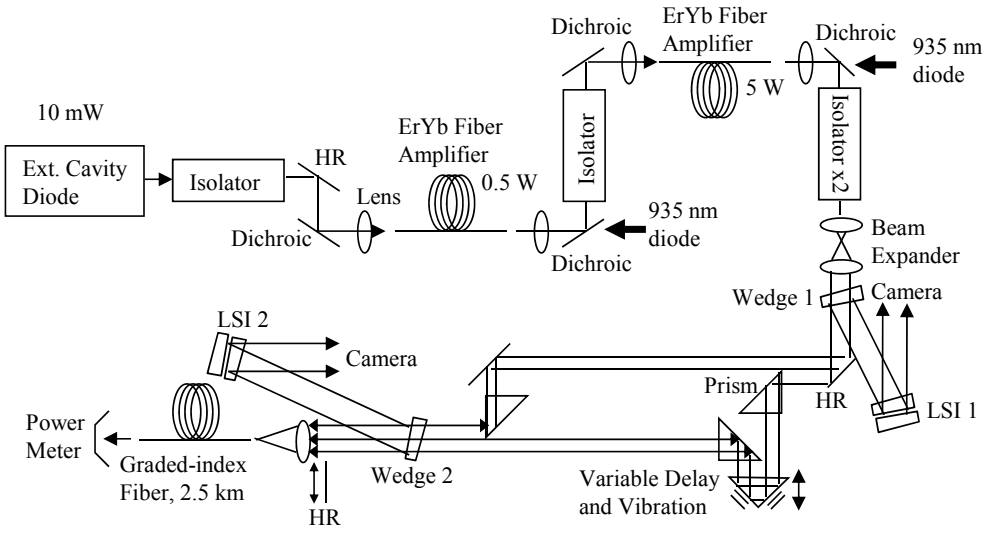

Fig. 46: Apparatus diagram for measuring fidelity of phase conjugation using an interference method. LSI: Lateral shearing interferometer, HR: High reflecting mirror.

After isolation, the beam was expanded to 10 mm diameter and wavefront split with an uncoated right angle prism into two beams with semicircular cross sections. The beams then propagated through different paths. One of the paths was equipped with an optical trombone to test the ability of the fiber to compensate for path length variations. The optical trombone consisted of a 180° turning prism on a longitudinal translation stage which could be controlled with a piezo-electric transducer for rapid oscillations. The two beams were tiled side-by-side with a prism and coupled into 2.5 km of 50-μm core, 0.21-NA, graded-index fiber. As shown in Fig. 46, a lateral shearing interferometer (LSI) on each beam pickoff was used to analyze the SBS reflection from the graded-index fiber immediately after reflecting from the fiber (LSI 2) and after recombination (LSI 1). The beam emitted by the single mode amplifiers before being split into two channels is shown in Fig. 47. A prism was placed in the beam to reflect half of the beam through a different optical path. This resulted in two truncated, semicircular beams. After

propagating through two separate paths, the beams were then tiled side-by-side using another right angle prism (Fig. 48).

5.3.2. Mirror Reflection Example

To contrast the unique properties of the Stokes reflection and to characterize the phase properties of the incident beams, interference images were taken of the beams as reflected by a highly reflective (HR) planar mirror. The mirror was placed in front of the fiber coupling lens to reflect the collimated incident beams back toward the source. A wedge sent a portion of the beam to LSI 2. The LSI produced an interference pattern of the two beams. The LSI is made from two wedged windows separated by ~ 1 cm, and each window had one side AR-coated. The two uncoated faces create reflections laterally

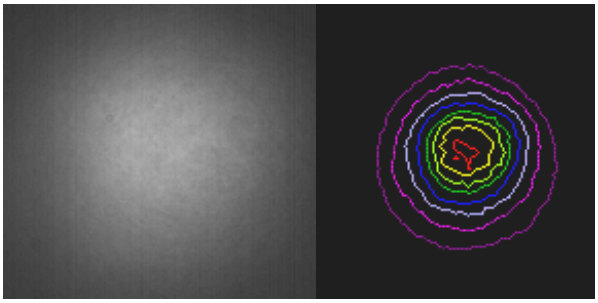

Fig. 47: Irradiance image and contour plot of the MOPA output beam.

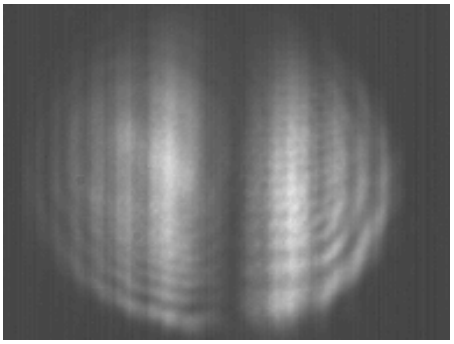

Fig. 48: Tiled beam profile after propagation through separate paths.

shifted relative to each other. In the resulting interference pattern, there are three zones of interest. As shown in Fig. 49(b), zone one is the left semicircular beam interfering with itself, while zone 3 is the right beam interfering with itself. As long as the two wedges are stable and much closer than the coherence length of the individual beams, these self-interference zones will produce stable fringes regardless of fluctuations in the phase of the incident beams. This contrasts with zone two, which is the mutual interference between the left and right beams. In this region, the position of the fringes depends on the relative phase between the left and right beams. High contrast fringes indicate spatial coherence across the two semicircular beams. If the beams are both coherent and have the same phase, the maxima of the high-contrast fringes will line up across all 3 zones. If the beams are not coherent with each other, there will be no fringes visible in zone 2. Lastly, if the beams are coherent but have a phase offset, the fringes in zone 2 will be visible but discontinuous between the zones.

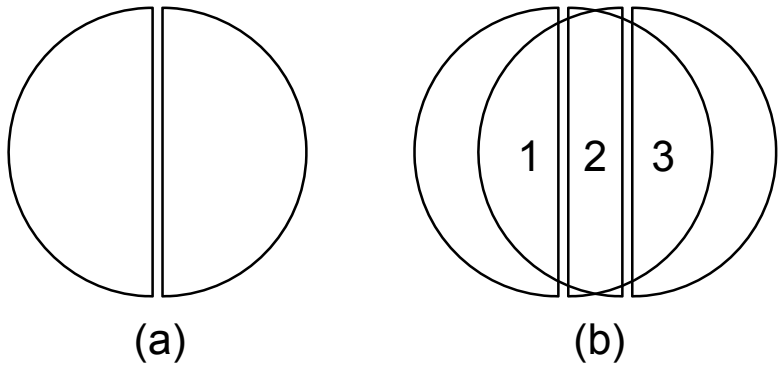

Fig. 49: Schematic of the beam profiles (a) after reflecting from the HR mirror and (b) after reflecting off the LSI. The three interference zones of the LSI are numbered in (b) to clarify self-interference (1 and 3) and mutual interference (2) zones.

With the path length held constant, Fig. 50(a) was collected. Each image in this work is an average of 10 images taken successively at the camera frame rate of 30 Hz. Interference fringes with good visibility in zone 2 show that the beams are spatially coherent, but the discontinuity on each side of zone 2 shows that the beams are not in phase after propagating through different paths. In fact, the fringes in zone 2 shift rapidly with any translation of the path delay prism, while the fringes in zones 1 and 3 remain stable.

The transducer on the path delay prism was activated to demonstrate the loss of spatial coherence between the two reflected beams from the HR mirror. The vibration was chosen in the form of a triangle wave with a 5.5 Hz oscillation frequency to avoid resonance with the camera. The full range of travel was 0.2 mm. As shown in Fig. 50(b), the self-interference fringes in zones 1 and 3 remain visible. Since the transducer imparted a rapidly changing relative phase difference between the two beams, it resulted in a dramatic loss of visibility in zone 2.

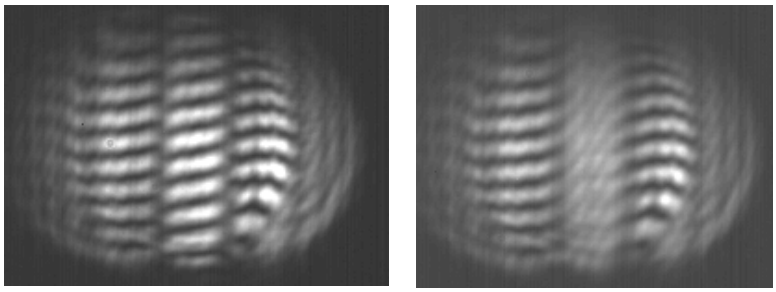

Fig. 50: Interference images of the two beams at LSI 2 after one pass through separate paths and reflected by a standard HR mirror with vibration (a) off and (b) on.

The fringe visibility in zone 2 of Fig. 50(b) was higher than expected since there was no mutual coherence at this point. Further inspection of the self-interference images show that the remaining fringes in zone 2 are not due to mutual coherence. The self-interference was viewed from each channel independently with the other channel was blocked. The images are shown in Fig. 51. The fringes visible in zone 2 of Fig. 50(b) are visible in the self-interference images and are not due to mutual coherence. Diffraction at the wavefront-splitting prism caused the semicircular beam to spread into zone 2 and interfere.

Similar images were taken at LSI 1 with the HR mirror in place (Fig. 52). A lens was used to image the point of recombination at the right angle prism onto the camera. Fig. 52(a) shows the interference pattern with both beam paths held constant. Again, the fringe discontinuity between the three zones indicates that the beams were not phased. This was emphasized by activating the vibration and noting the loss of fringe visibility in zone 2 in Fig. 52(b). As expected, the results of Fig. 50 and Fig. 52 indicate that the beams are not in phase after traversing separate optical paths, nor after being reflected by an HR mirror back through the system.

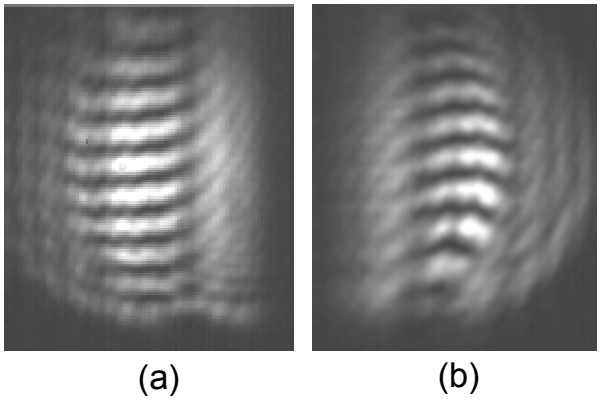

Fig. 51: Self-interference images at LSI 2, each taken with one path blocked. The self-interference shows the fringes extending into zone 2 are not due to mutual coherence.

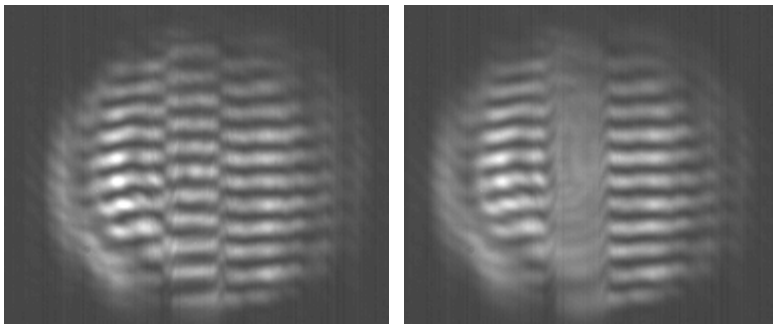

Fig. 52: Interference images of the two beams at LSI 1 as reflected back through the respective beam paths by a standard HR mirror with vibration (a) off and (b) on.

5.3.3. SBS Reflection Results

The SBS reflection was characterized in the same manner, but with remarkably different results. After the HR mirror was removed, the beams were coupled into a 2.5 km length of 50/250 graded-index fiber with a core numerical aperture of 0.21. The coupling efficiency to the fiber was 80+/-5%. Care was taken to ensure that both beams had an equivalent coupling efficiency into the fiber. The high coupling efficiency indicates that the fiber did not significantly spatially filter the input beams. To verify that the coupled light was not single mode, images of the beams transmitted through the fiber were collected and are shown in Fig. 53. The transmission through the fiber was clearly multimode and slowly varied over time.

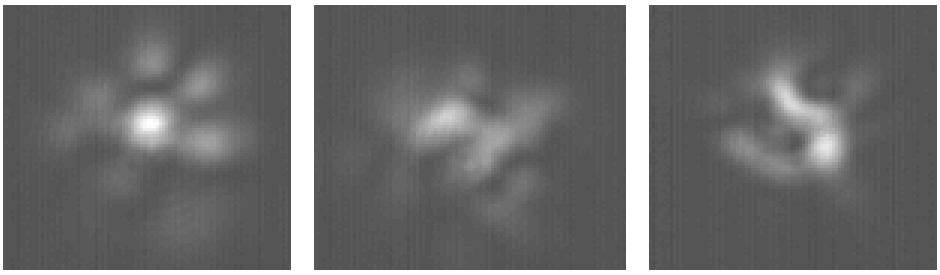

Fig. 53: Sample irradiance images of the transmission through the graded-index fiber.

SBS threshold was reached in the fiber at 0.4+/-0.1 W of transmitted power. The typical Stokes beam is shown in Fig. 54. The Stokes beam would periodically form the double-lobed mode shown in Fig. 55, but this mode was very sensitive to minute changes to fiber alignment and the path delay prism. The single lobe pattern of Fig. 54 was much more common. The generation of the fundamental and low-order modes in the Stokes beam is expected from SBS beam cleanup.

A lens was placed after wedge 2 (Fig. 46) to image the beams and measure the interference pattern as it would be at the location where the two optical paths come back together. The interference pattern of the Stokes beam immediately after reflection from the graded-index fiber was measured by LSI 2. Whether the vibration is off (Fig. 56(a)) or on (Fig. 56(b)), the Stokes beam remains unchanged. An image of the 2-lobed Stokes beam was collected from the interferometer (Fig. 57). In the null region between the two

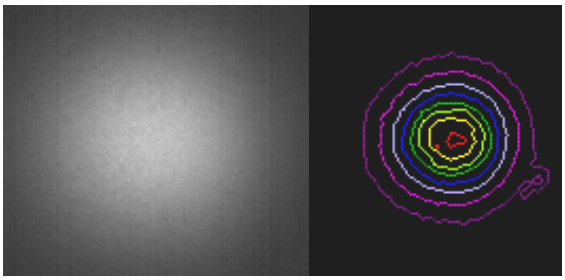

Fig. 54: Stokes beam irradiance pattern. The same image is shown as a contour plot for clarity.

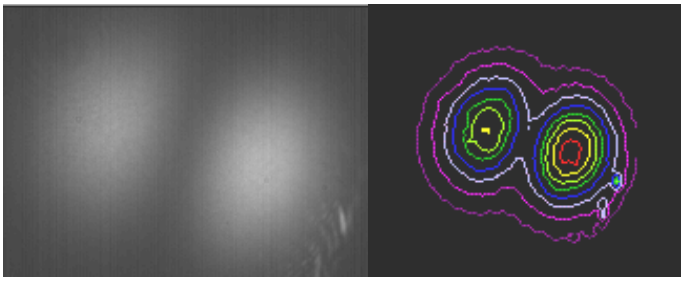

Fig. 55: A two-lobed fiber mode resulting from SBS in a graded-index fiber.

lobes, the fringes lose contrast as the irradiance drops, and it appears that the two lobes are phase-shifted by π as would be expected from an LP_{11} mode. When vibration was activated, the careful conditions required to observe the two lobed pattern are lost and the interference pattern recorded was identical to Fig. 56(b). This shows that a single, spatially-coherent Stokes beam is generated in the fiber via SBS, as expected from beam cleanup. However, a phase conjugate beam immediately after reflection from the fiber would not be coherent at this point. A perfect phase-conjugate beam would have the coherence of the incident beam, which was shown to be incoherent at this point after a single pass through separate paths. To measure the phase conjugation fidelity, the coherence at LSI 1 must be analyzed.

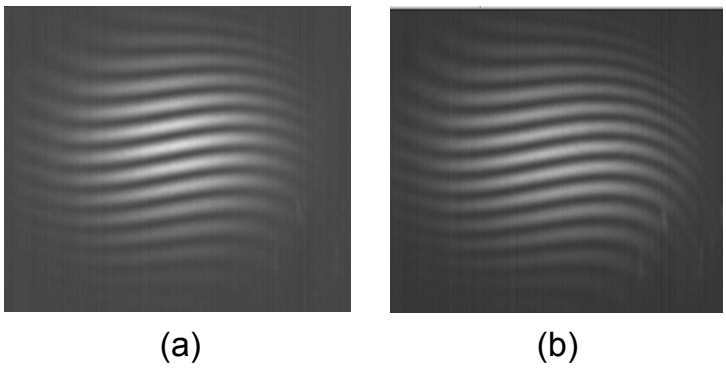

Fig. 56: Images of the Stokes beam at LSI 2 with vibration (a) off and (b) on.

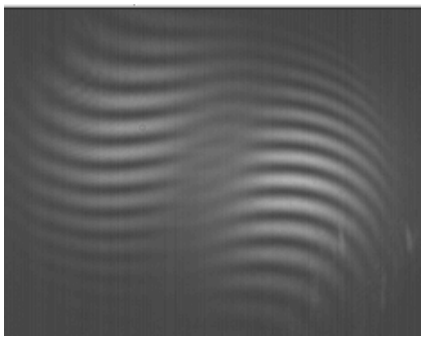

Fig. 57: Interference image of the double-lobed Stokes beam at LSI 2.

The Stokes reflection viewed using LSI 1 showed that the beams were not phased after propagating back through the separate paths (Fig. 58). Fig. 58(a) shows the beams without interference as collected from only one of the two wedges in the LSI. Fig. 58(b) shows a discontinuous fringe pattern produced in zone 2 where mutual interference occurs. When the vibration was activated as shown in Fig. 58(c), the self-interference zones remained stable, but the mutual interference fringe visibility dropped as the fringe pattern rapidly oscillated. The low-contrast fringes remaining in zone 2 of Fig. 58(c) appear to be self-interference since the fringes do not extend throughout the entire region and are at a different angle than the fringes shown in Fig. 58(b). This indicates that the relative phases were not locked after propagation back through the optical paths.

As discussed above, a phase conjugate reflection would not be phased at LSI 2. The fringe results should mimic those from the HR mirror. The reflection should also have an irradiance pattern that closely mimics that of the incident beams. At LSI 1, however, the phase conjugate reflection should be spatially coherent. Because of the

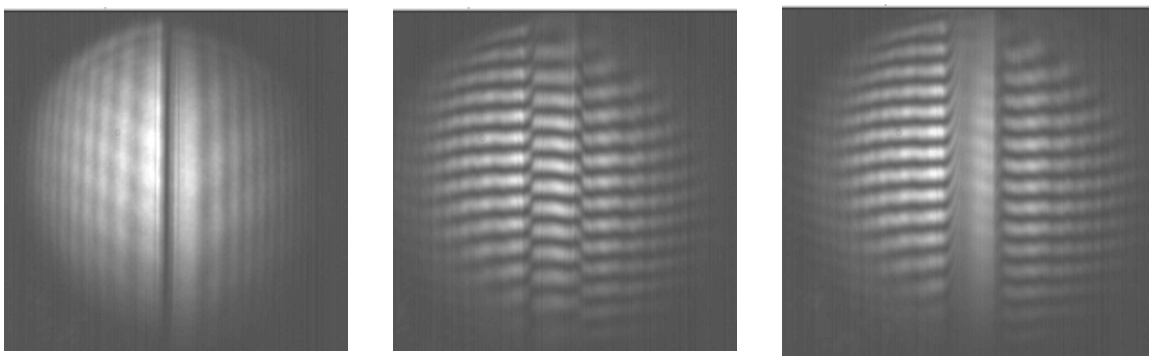

Fig. 58: Stokes beam from the graded-index fiber after propagating back through the two paths. The beams are shown at LSI 1 after recombination (a) without interference, (b) with interference and still prism, and (c) with interference and prism vibration.

wavelength shift induced by SBS, the two Stokes beams may not be phased after propagation back through the individual paths. The dephasing of the two beams would be $\Delta\phi = 2\pi\left(\nu_p - \nu_s\right)\Delta l/c$, where ν_p (ν_s) is the pump (Stokes) frequency, and Δl is the difference between the two beam paths.[55] Given the small Stokes shifts in optical fiber (~11 GHz), this function varies slowly relative to a wavelength. The relative phase shifts by 2π when $\Delta l \approx 27$ mm. Given that one path includes the optical trombone, the two beam paths vary by more than 27 mm. It is therefore expected that a phase conjugate beam would only coincidentally be phased after propagation back through the two paths, which would generate continuous fringes in Fig. 58(b). More importantly however, an additional 0.4 mm change in optical path length caused by vibration of the path in the optical trombone would have a negligible effect on the relative phase ($\Delta\phi_{vib} \approx 0.1$). Therefore, a phase conjugate reflection would be characterized by visible fringes in zone two of the LSI fringe pattern even with the vibration stage turned on. Furthermore, if the power in each channel was equivalent, a fringe visibility of one would result, which is the fidelity of the perfect phase-conjugate beam.

Beam cleanup would have remarkably different characteristics. Since the beam exits the fiber in a pure fiber mode, it would be spatially coherent across its transverse dimension immediately after exiting the fiber. Once it is split into two independent beams which propagate through time dependent path lengths and are finally tiled together, the spatial coherence of the beam is lost.

The two paths act as a beam distortion in the traditional fidelity measurements discussed above. The divergence of the Stokes beams after recombination at LSI 1 matches that of the incident beam quite well despite the double-semicircular pattern of

the beam (Fig. 58(a)). Using the divergence method of fidelity, the conclusion would be a high phase conjugation fidelity. Similar results would be expected from power-in-the-bucket measurements, while the alignment of the Stokes reflection would cause an in-line pinhole technique to measure a varied transmission similar to the experiment plotted in Fig. 45. Since the reflected beam shown in Fig. 54 has better beam quality than the input double-semicircular pattern of Fig. 48, the M^2 technique would accurately assign a fidelity of zero to this situation.

However, the occurrence of beam cleanup to the LP_{11} mode shown in Fig. 55 presents some ambiguity to these methods. The double-lobed structure of Fig. 55 could certainly be interpreted as a phase conjugate replica of the pump with decreased fidelity due to the high spatial frequency components being filtered out. Interpreting the Stokes reflection as a phase conjugate is not consistent with the highly sensitive nature of the spatial characteristics of the reflection to variations in the coupled beam. Additionally, the SBS reflection required precise angle alignment of the fiber tip in order to propagate back through the system on-axis. This adjustment would not have been necessary if a phase conjugate beam had been generated, since a phase-conjugate reflection should remain stable with small perturbations to the coupling characteristics. However, the fringe pattern at LSI 1 observed when the phase of one beam is rapidly varied (Fig. 56(b)) demonstrated clearly that the beams lack coherence at this point. Therefore, this double-lobed structure does not introduce error into the measurement of fidelity through the interference method.

Using the interference method, fidelity near zero was determined and clearly indicated beam cleanup, but not phase conjugation. The beam cleanup conclusion is

supported by the LSI measurements which indicate that the reflected Stokes beam immediately after the SBS generating fiber is spatially coherent. This is verified even with significant and variable phase error between different components of the input beam. But, the fact that the two legs of the Stokes beam after propagation back through separate beam paths do not produce a spatially coherent beam as measured by LSI 1 eliminates the possibility that this type of reflection could be interpreted as a phase conjugate replica of the pump.

The image was analyzed by reading it into Mathematica. The pixel values were used to determine the maximum and minimum values of the fringes along vertical lines through the image. The fringe visibility was then determined according to[162]

$$V(q) = \frac{I_{\max} - I_{\min}}{I_{\max} + I_{\min}}, \tag{5.3}$$

where $V(q)$ is the visibility in the vicinity of point q, and I_{max} and I_{min} are the maximum and minimum irradiances near point q. When the average irradiance from the two beams is equivalent, the visibility represents the degree of coherence. When the beams are unequal, the more general form of the equation must be used to determine the degree of coherence $|\gamma_{12}(\tau)|$ for a given path difference τ such that[162]

$$|\gamma_{12}(\tau)| = V(q)\frac{I_1(q) + I_2(q)}{2\sqrt{I_1(q)I_2(q)}}. \tag{5.4}$$

The pixel columns were grouped by interference zone and averaged together. While the peak of the mean irradiance in zones 1 and 3 was found to differ by $29 +/- 2\%$, the mean fringe visibility was comparable within these zones at $75.6 +/- 3.1\%$ and $77.3 +/- 2.7\%$. The fringe visibility in zone 2 was measured at 9.6+/-3.1%, while the mean visibility in zones 1 and 3 was 76.8+/-2.7%. Since the

irradiance was not equal between the two paths, the degree of coherence was computed using Eq. (5.4) at 9.7+/-3.1% in zone 2.

A significant error in zone 2 is the residual fringes. These fringes can be attributed to residual self-interference occurring through diffraction from the beams in zones 1 and 3. The fringes are not as significant as those seen in zone 2 of Fig. 50 and Fig. 51, but exhibit the same characteristics. This leads to the conclusion that the residual fringes are not indicative of mutual-coherence. For instance, the fringes do not span zone 2 as do the fringes shown in Fig. 58(b). The fringes are also at a different angle than those in zone 2 without vibration, again shown in Fig. 58(b). The appearance of these fringes may be minimized through better imaging of the prism near LSI 1 in Fig. 46 where the beams were recombined.

As a result of these measurements, the fidelity measured using this method was $0.097 +/- 0.031$. The measurement deviated from zero on average due to the error of self-interference fringes in zone 2.

5.4. Conclusion

Measurements of fidelity using beam quality methods were shown to be fairly accurate for applications demonstrating fidelity near one. However, the occurrence of beam cleanup and other applications where fidelity declines cause additional error in these methods. A more precise measure of fidelity was found using interference fringes, which is more applicable to beam combining applications.

6. CW Phase Conjugation

6.1. Overview

As discussed in Chapter 2, fiber optic waveguides provide a long interaction length which lowers the threshold of SBS to power levels easily achievable by CW laser sources. Since the Stokes wave experiences a small Doppler shift, the longitudinal propagation constants of the modes excited by the Stokes wave differ slightly from those excited by the seed. The SBS reflection becomes out of phase with a theoretical perfect phase conjugate reflection over many meters of fiber. As a result, the fidelity of phase conjugation from SBS in step-index fibers decreases with increasing fiber length. While longer fibers are preferred in order to reach threshold at a lower power, shorter fibers are needed to generate a high fidelity phase conjugate beam.

CW phase conjugation in step-index fibers had not been achieved prior to this work. Typically only pulsed lasers could generate the irradiance necessary to exceed SBS threshold in fiber short enough to generate phase conjugation. At the start of this work, existing theory predicted fiber lengths shorter than a few meters were needed to generate phase conjugation. In Chapter 3, there are a handful of examples of fiber lengths longer than a couple meters generating phase conjugation using pulsed laser sources. Kuzin *et al.* compared phase conjugation characteristics from 7 m and 130 m fibers. While the 7-m fiber produced conjugation better than ~80%, they noted that ~50% depolarization occurred in the Stokes beam for the 130 m fiber.[60] Vasil'ev *et al.* employed a 25-m fiber as a phase conjugate mirror to effectively remove amplifier-

induced aberrations.[61] Fiber amplifiers up to 10 m in length have been used as well to generate high fidelity SBS phase conjugation with pulsed lasers to seed SBS.[106]

In order to design efficient CW laser systems using SBS phase conjugation for coherent beam combination, the length of fiber that can be used to generate a high fidelity phase conjugate reflection was explored further. In this work, the phase conjugate fidelity was measured as a function of fiber length during cutback tests on two silicate, step-index fibers. Fidelity was lower at longer lengths of fiber. As the fibers were cut back, the fidelity increased to ~0.80 using a 40-m length of a 40-μm core diameter, 0.06-NA fiber (CorActive Ge740).[123] Similar fidelity was achieved from 15 m of 20-μm core, 0.13-NA fiber (CorActive MM-20/125).[123] This work inspired Spring's numerical model described in Chapter 3. Along with modeling results for these two fibers plus an additional one, the fidelity obtained was related to a scaled length parameter which showed a correlation among the different fibers.[123] SBS beam cleanup in step-index fibers was observed at longer fiber lengths, as well as the transition from beam cleanup to phase conjugation.

6.2. Phase Conjugation Experiment

The apparatus is shown in Fig. 59.[123] It consisted of a 1064-nm, narrow-linewidth laser (NPRO) operating at 700 mW and a 2-stage fiber amplifier as described in Chapter 4. The first fiber amplifier is 10.3 m of Nufern's Yb-doped 20/400 (core diameter/clad diameter in microns) PLMA fiber, counter-pumped with a fiber-coupled diode from LIMO which generated up to 20 W through a dichroic mirror. The output of the first stage was 5.5 W. The second stage was also a 20/400 PLMA fiber with a length of 5.2 m. The second stage was co-pumped with a 100-W, fiber-coupled diode. Co-

pumping was chosen to prevent damage to the diodes, and the fiber length was reduced to prevent the onset of SBS in the amplifier as discussed in Chapter 4. The shortened length reduced the pump absorption in the fiber by approximately 20%. The 2-stage amplifier produced an output power of 50 W.

Free space coupling was used throughout the experiment, and each fiber tip including the test fiber was polished at 8° to prevent cavity effects and Fresnel reflection noise in the data. The output of the first stage amplifier was over 95% linearly polarized. To bypass polarization control on the high power amplifier, each polarization of the signal beam after the second-stage amplifier was separately isolated and recombined.

The method employed to measure fidelity was the in-line pinhole method similar to Kuzin *et al.* [60] and described in Chapter 5. While the interference approach was shown to be more accurate in distinguishing beam cleanup, the implementation would have required test fibers that support many more modes for efficient coupling of two tiled beams into the test fiber. The larger test fiber would have required additional seed power

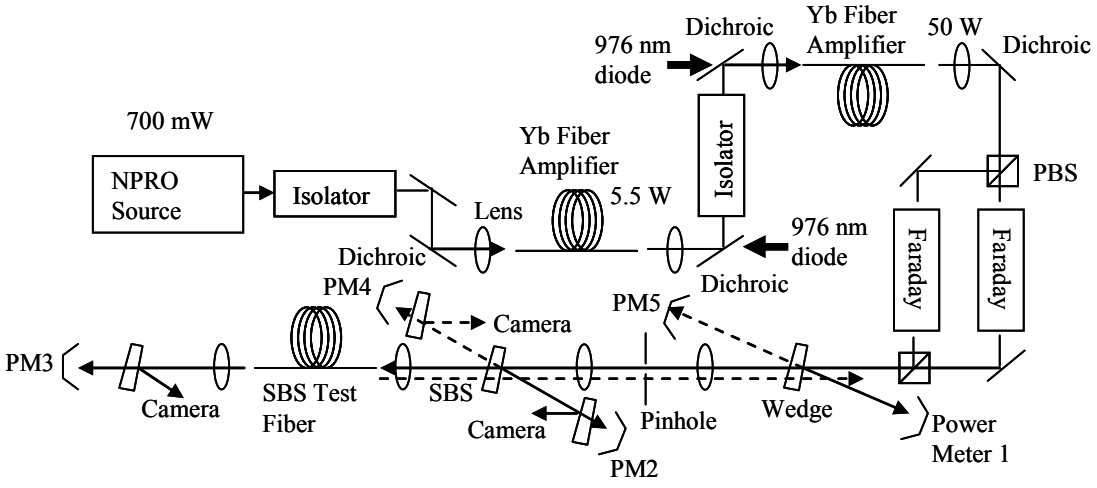

Fig. 59: Apparatus used to test phase conjugation fidelity of silicate fibers at 1064 nm wavelength.

which was not available to generate SBS in the short lengths of fiber necessary for phase conjugation. An alternative to higher power is to use a fiber such as chalcogenide which has a much larger SBS gain coefficient as described in Chapter 4. The higher gain coefficient allows chalcogenide fiber to support more modes while reducing the SBS threshold power. The use of a chalcogenide fiber for this purpose is described in the next chapter.

The full signal beam was focused through a pinhole with a diameter of 300 μm before propagating to the test fiber. The pinhole was imaged onto the fiber tip such that the pinhole image diameter was less than half of the core diameter of the fiber. The pinhole image size was chosen as small as possible and ultimately limited by the NA of the test fiber to maintain coupling efficiency. Since the entire incident beam passed through the pinhole, a perfect phase-conjugate Stokes beam would have complete transmission back through the pinhole. The pinhole transmission of the Stokes beam was the measure of fidelity.

This fidelity measurement technique can distinguish between phase conjugation and SBS beam cleanup to the fundamental mode as described in Chapter 5. Since the pinhole has a smaller image diameter than the fundamental fiber mode, it was calculated that less than 66% pinhole transmission would be achieved in the event that the Stokes reflection propagates in the fundamental mode. The coupling parameters for each fiber are shown in Table 5. The maximum transmission would be observed provided the pinhole image was centered on the fiber tip. To further reduce this error, the signal was coupled off-center into the test fiber by $7.2 +/- 1.2\ \mu$m for the 0.13-NA fiber. The expected transmission from the fundamental mode was reduced in this case to 17+/-7%.

Similarly, the expected transmission of a flat-top beam would be less than 25%, which was computed using a ratio of the area of the pinhole image to the core area of the fiber. The coupling efficiency with the 0.06-NA fiber was more sensitive to position, which prohibited significant off-center coupling. The fiber was centered within a few microns to maximize coupling efficiency. With this coupling, pinhole transmission of 63% or less using the 0.06-NA fiber could be the result of beam cleanup, and a flat-top Stokes beam would be expected to have a transmission of 21%. As with all spatial measurements of phase conjugation fidelity, low-fidelity measurements are ambiguous.

Wedged windows with anti-reflection coating on one side were used to measure the power before and after the pinhole. Additional beam pickoffs were used to reflect portions of the beam to a screen where a Cohu, solid-state camera simultaneously recorded the beam irradiance cross-section incident on the test fiber, the transmission through the test fiber, and the Stokes beam.

Table 5: Fiber and coupling characteristics for phase conjugation experiments.

	0.13 NA fiber	0.06 NA fiber
Core diameter (μm)	20	40
Core NA	0.13	0.06
Fiber M^2 (V/2)	3.8	3.5
Fundamental mode $1/e^2$ diameter (μm)*	14.5	29.4
Pinhole image diameter at fiber tip (μm)	9.6	18.5
Incident beam diameter at fiber tip (μm)	5.5+/-0.3	11.3+/-0.6
Coupling NA	0.119+/-0.006	0.057+/-0.004
Coupling efficiency (%)	79+/-5	84+/-5

*Marcuse, D., *Loss analysis of single-mode fiber splices.* Bell Syst. Tech. J, 1977. 56(5): p. 703–718.

6.2.1. Data Collection and Analysis

The fiber was cut back in set intervals, polished, and tested at its new length without disturbing the input end of the test fiber. This enabled the measurement of fidelity as a function of fiber length. To measure fidelity, the power meters labeled PM4 and PM5 in Fig. 59 were connected to an oscilloscope. The powers were measured simultaneously by the oscilloscope and the ratio of PM5 to PM4 provided the raw fidelity data. To avoid large errors caused by dividing by voltages near zero, all data corresponding to reflected powers less than 600 mW was discarded. A single measurement consists of the average of all calibrated data after SBS threshold is exceeded giving a Stokes reflection greater than 600 mW. Multiple measurements were taken at each length whenever possible.

By taking the data with the oscilloscope, the number of data points per trial was typically ~500 or more. It was observed that connecting the power meters to an oscilloscope for data collection bypassed the internal calibration algorithms of the individual meters. Since the response and zero of each uncalibrated meter was slightly different, the calibration was a function of power. To calibrate the measurements, an HR mirror was placed in front of the fiber and aligned to reflect the incident beam back through the pinhole towards the amplifiers. The pinhole was then removed, and calibration data consisted of the ratio of PM5/PM4 as a function of the PM4 power, shown in Fig. 60. This accounted for differences in the power meters as well as for small losses from each optic between PM4 and PM5.

The calibration data was separated into groups (bins) defined by the reflected power, and a span of 200 mW of reflected power per bin was chosen. The mean and

standard deviation of the ratio of PM5/PM4 was taken of each bin. The standard deviation of the reflected power in the bin was also calculated, and this data was plotted as a function of the center of each bin as shown in Fig. 61.

During the experiments, the seed power was increased to generate SBS in the test fiber. The oscilloscope simultaneously read the seed power both incident and transmitting the fiber, and the Stokes power both incident (PM4) and transmitting (PM5)

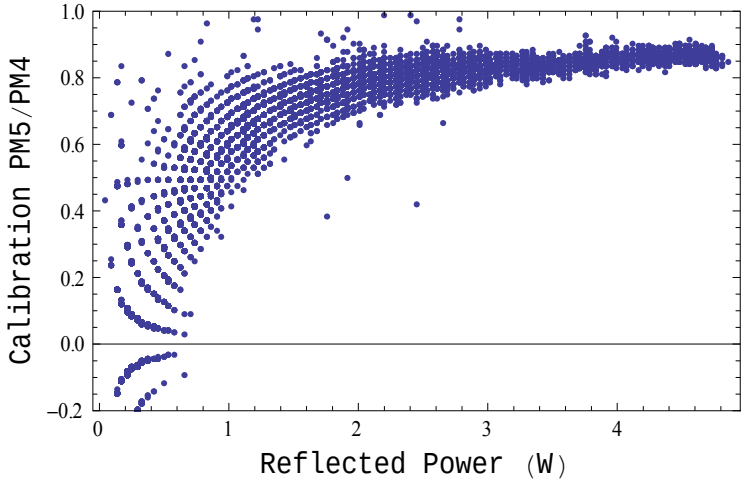

Fig. 60: PM5/PM4 calibration data as a function of reflected power.

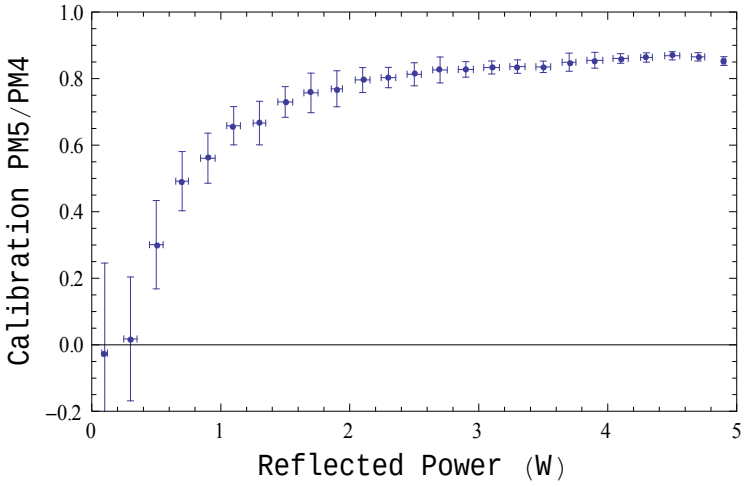

Fig. 61: Error bar plot showing the mean and standard deviation of the calibration data in 200-mW bins of reflected power.

the pinhole aperture. The oscilloscope also took the ratio of PM5/PM4, and this ratio was plotted as a function of Stokes power as shown in Fig. 62 taken from a 20-m length of 0.13-NA fiber.

The raw pinhole transmission data was then calibrated by Stokes-power bin using the calibration data in Fig. 61. For each bin *i* of the raw data, the mean $\mu_r^{(i)}$ and standard deviation $\sigma_r^{(i)}$ was computed, where *r* denotes "raw data." The calibrated mean $\mu^{(i)}$ and standard deviation $\sigma^{(i)}$ was then computed for each bin using the calibration data for that bin, where the mean $\mu_c^{(i)}$ and standard deviation $\sigma_c^{(i)}$ are denoted by the subscript *c* for "calibration." The mean was computed as $\mu^{(i)} = \mu_r^{(i)} / \mu_c^{(i)}$ for each bin, and the standard deviation was determined using[163]

$$\sigma^{(i)} = \sqrt{(\mu^{(i)})^2 \left[\left(\frac{\sigma_r^{(i)}}{\mu_r^{(i)}} \right)^2 + \left(\frac{\sigma_c^{(i)}}{\mu_c^{(i)}} \right)^2 \right]}. \tag{6.1}$$

The calibrated data for this trial is shown in Fig. 63.

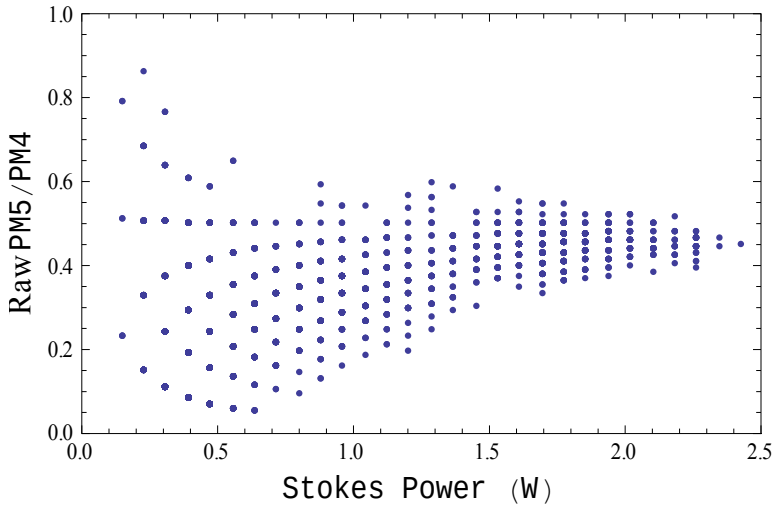

Fig. 62: Uncalibrated pinhole transmission by the Stokes beam measured as a function of Stokes power reflected by a test fiber with 0.13 NA and length of 20 m.

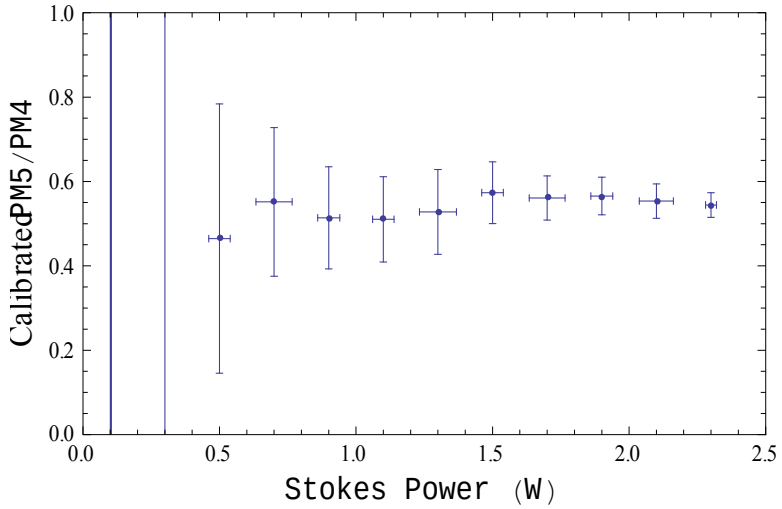

Fig. 63: Calibrated mean and standard deviation of the pinhole transmission as a function of Stokes power.

To determine the fidelity of the Stokes reflection for this experiment, the data in the bins was averaged for all Stokes-power bins above 0.6 W. The mean was determined using the formula:[163]

$$\mu = \sum_i \frac{N^{(i)}\mu^{(i)}}{(\sigma^{(i)})^2} \Bigg/ \sum_i \frac{N^{(i)}}{(\sigma^{(i)})^2}, \tag{6.2}$$

and the standard deviation was calculated as

$$\sigma = \left(\sum_i \frac{N^{(i)}}{(\sigma^{(i)})^2} \right)^{-\frac{1}{2}}. \tag{6.3}$$

For the sample fiber shown above, the resulting fidelity was $0.552 +/- 0.002$.

6.2.3. Results

The results of the cutback test show a distinct increase in phase conjugation fidelity as each fiber is shortened as shown in Fig. 64.[123] The blue dots with error bars are the experimental results of this work, while the blue line represents modeling results

obtained by Spring.[63] The red, dashed line represents fidelity as a function of length given by Eq. (2.65). With a 40-m long fiber, the fidelity was ~0.40. A fidelity of 0.791+/-0.004 was achieved with a fiber length of 15 m for the 20-μm core, 0.13-NA fiber. While the input coupling was not adjusted during testing, small changes in coupling due to thermal effects in the amplifiers and optics change the modes excited in the test fiber. While this was not noticeable within an individual trial, these small coupling changes are probably responsible for the variation in measured fidelity between trials at the same fiber length.

A fidelity of 0.837+/-0.008 was obtained from a 40-m length of the 0.06-NA, 40-μm core fiber (Fig. 65), which was increased from a fidelity of ~0.65 at a length of 100 m.

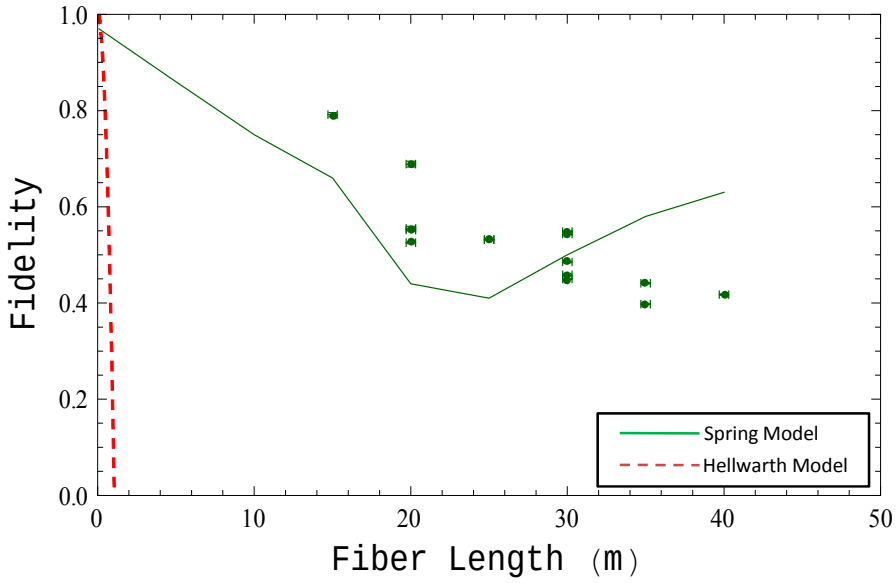

Fig. 64: Phase conjugation fidelity as a function of fiber length for the 0.13-NA fiber. The experimental data is compared to Spring's model and Hellwarth's model.

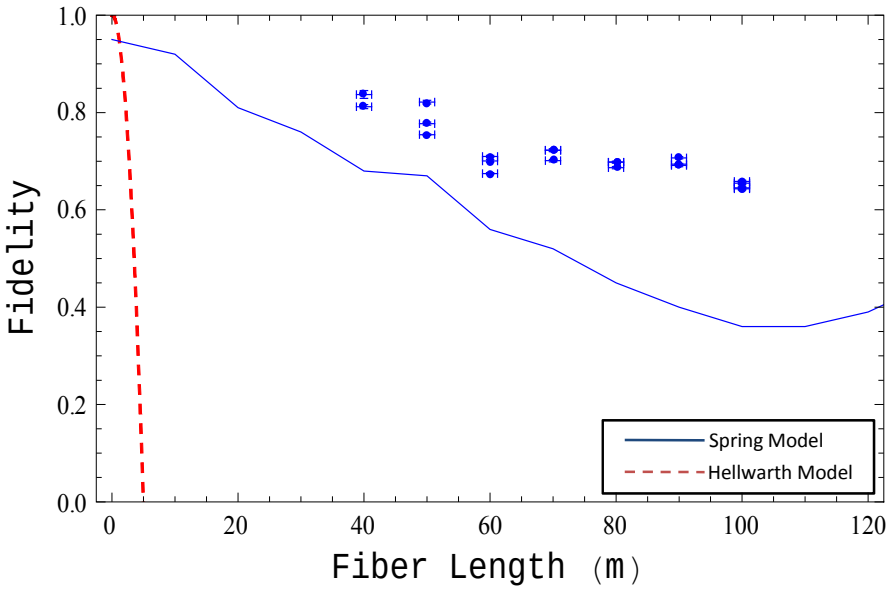

Fig. 65: Phase conjugation fidelity as a function of fiber length for the 0.06-NA fiber. The experimental data is plotted along with Spring's model and Hellwarth's model.

These sets of data document the first time CW phase conjugation via SBS has been achieved in step-index fiber. It is also the first time that the deterioration of phase conjugation fidelity with fiber length has been traced experimentally.

Images were taken during testing of both of these fibers to show the beam incident on the test fiber, after fiber transmission, and the Stokes reflection. The beams were reflected from wedged windows placed in front of PM2 (incident), PM3 (transmitted), and PM4 (Stokes) shown in Fig. 59, and each beam was propagated to a screen and imaged simultaneously. The images are shown in Fig. 66 and Fig. 67 to show general beam shape and relative divergence. In each image, the incident beam is shown in the upper left of the frame, the transmitted beam is in the upper right, and the Stokes beam is shown in the lower portion of the frame. The images were smoothed using 6-pixel averaging to remove speckle induced by reflection from the screen. The

transmission through the test fiber is multimode in each image, and the Stokes beam is single-lobed for all lengths tested using the 0.06-NA fiber (Fig. 66). Coupling conditions were varied prior to the cutback test which occasionally resulted in an LP_{11} Stokes beam using a 100-m length of fiber.

For the 0.13-NA fiber, the images show the Stokes beam in the LP_{11} mode at 40 m and a progression toward single mode as the fiber is shortened. While the front of the fiber was not disturbed throughout the cutback tests, the back end had a new 8° polish and slight differences in location after each cut. These changes in the back end of the test fiber caused the beam to move relative to the camera image. The incident beam was coupled off-center, which was the most-likely cause of the LP_{11} mode in the Stokes beam at longer fiber lengths where phase conjugation fidelity declines. As the fiber length was shortened, the phase conjugation fidelity improved and the LP_{11} mode was gradually replaced by a phase conjugate of the incident beam. Spring's model predicts the occurrence of beam cleanup in step-index fibers when the test fiber is too long for good fidelity phase conjugation beginning at fiber lengths as short as 20 m as seen in this work.[63]

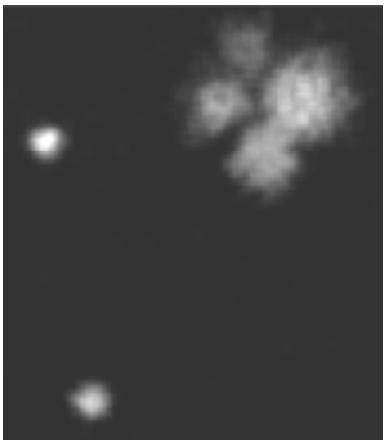

Fig. 66: Clockwise from top left: incident beam, test fiber transmitted beam, and Stokes reflection from the 0.06-NA fiber with a length of 40 m.

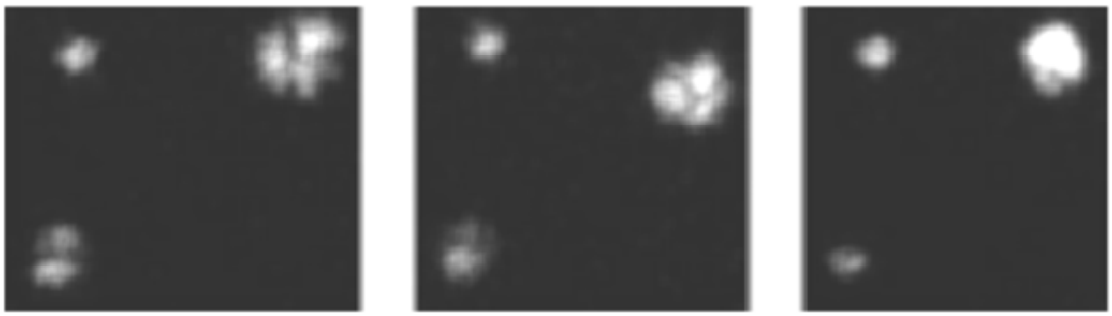

(a) (b) (c)

Fig. 67: Clockwise from top left in each frame: incident beam, fiber transmission, and Stokes beam from the 0.13-NA fiber with lengths of (a) 40 m, (b) 30 m, and (c) 15 m.

6.2.4. Discussion

The experiment shows high-fidelity phase conjugation is generated by lengths of fiber approximately an order of magnitude longer than had been calculated before the start of this work. The model of Hellwarth is shown in Fig. 64 and Fig. 65 for each fiber. It predicts a very rapid decline in fidelity that reaches zero at ~ 1 m for the 0.13-NA fiber

in Fig. 64 and at ~5 m for the 0.06-NA fiber in Fig. 65. For longer lengths of fiber, the Hellwarth model predicts negative fidelity values which are undefined.

The fidelity predicted using the Spring model is more accurate than previous models. The Spring model predicts high fidelity from much longer lengths of fiber as verified by this work, and it also accurately predicts the occurrence of beam cleanup in step-index fibers. However, the predicted fidelity was typically ~20% lower than the experimental results as the fidelity decreases from one and levels off at a low fidelity level. The Spring model also predicted an increase in fidelity as the fiber is lengthened further which was not supported by the experiment. The main approximation in Spring's model is that all pump modes and, separately, all Stokes modes vary equally with power as a function of length. The common mode amplitude growth and decay rate used in the model prevents the relative power between modes from evolving along the length of the fiber, which may be responsible for this resonance effect in the model. This indicates that the deviation between experiment and model may be explained through the highly-coupled analysis of modal interactions and varied gain or depletion among modes. Differences in coupling could also cause discrepancies between the model and the experiment.

The fidelity achieved with the 0.06-NA fiber in both modeling and experiment decreased with length at a much slower rate than the fiber with 0.13 NA. Although the calculations of Zel'dovich (Eq. (2.66)) and Hellwarth (Eq. (2.65)) lose validity as the non-conjugated fraction becomes large, both of their models include an analytic solution for the interaction length that is inversely proportional to the NA^2 of the fiber.

Specifically, the length of fiber that was calculated to produce a given phase conjugation fidelity was given by:[59]

$$L \le \frac{6\sqrt{(1-F)}c}{NA^2\Omega_B} \tag{6.4}$$

Russell demonstrated a similar dependence as a function of maximum phase error, $\Delta\phi$, such that[55]

$$L = \frac{2nc\Delta\phi}{\Omega_B NA^2} \tag{6.5}$$

The relationship between phase error and fidelity is not known, but the models of Hellwarth and Zel'dovich suggest $\Delta\phi \propto \sqrt{1-F}$. Regardless of this exact relationship, the fidelity is expected to decrease as the phase difference increases, since it is this phase mismatch that theoretically causes the length limitations. Therefore, the fibers in this experiment and model were compared based on the physical length of the fiber, the Stokes shift, and the square of the fiber core NA. This scaled length parameter has units of meter·GHz and is given by

$$L_s \equiv L\Omega_B NA^2 . \tag{6.6}$$

The maximum phase difference as defined in Eq.(6.5) differs from this parameter by a set of constants

$$\Delta\phi = \frac{L_s}{2nc} . \tag{6.7}$$

From inspection of Eq. (6.4) and Eq.(6.7), L_s may be a constant for a given phase conjugation fidelity.[123] In Fig. 68, the fidelity achieved experimentally with the two fibers as a function of fiber length is plotted for the experimental results in this work and Spring's model. In addition, a third fiber was modeled and included in this plot. The

additional fiber had an NA of 0.20 and a core diameter of 20 μm. In Fig. 69, these results are plotted against the scaled length parameter. As expected the data from the model and experiment are well correlated using this relationship. Also included in Fig. 69 is the plot of Eq. (6.4).

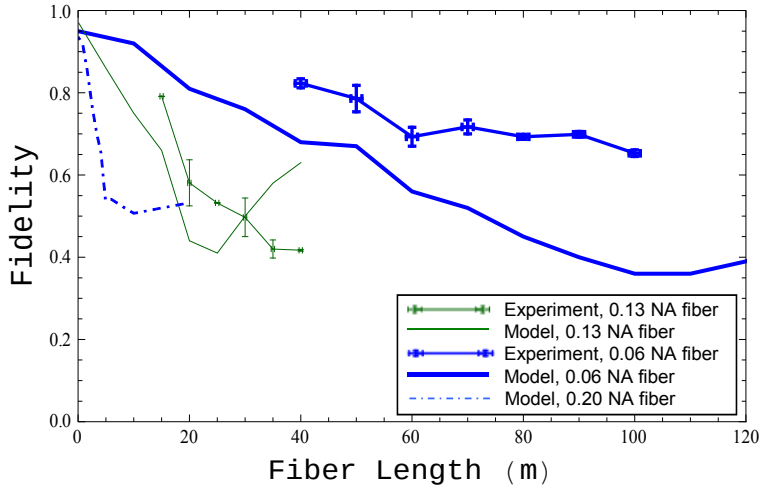

Fig. 68: Measured fidelity is plotted as a function of fiber length for two step-index fibers. Results from Spring's model are also shown.

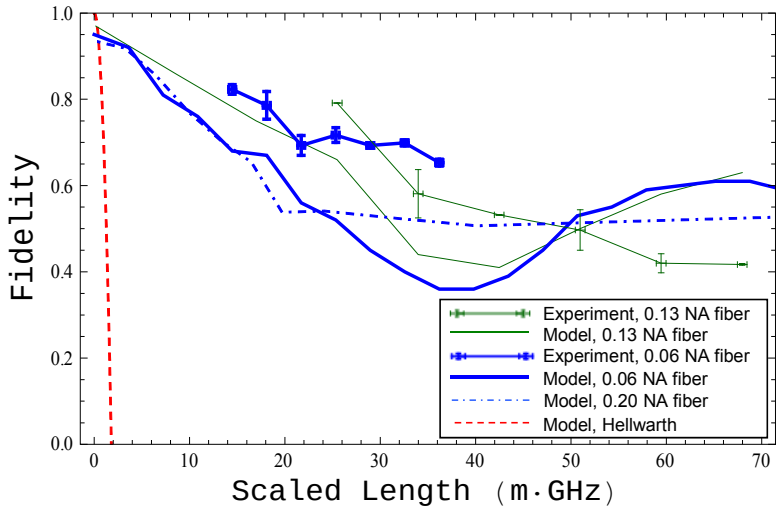

Fig. 69: Fidelity plotted as a function of scaled length.

Using the correlation between fidelity and the scaled length parameter, the SBS threshold power was approximated as a function of the quality of the beam that could be conjugated by a given fiber. The SBS threshold for a given multimode fiber is approximately given by[19]

$$P_{th} \approx \frac{21A}{g_I L}, \tag{6.8}$$

where the core area, A, has been substituted for A_{eff}, and the fiber was approximated as lossless. Solving Eq. (6.6) for L and substituting into Eq. (6.8) gives an expression for the SBS threshold power P_{th} as a function of the fiber parameters, SBS parameters, and scaled length parameter:

$$P_{th} = \frac{21A\Omega_B (NA)^2}{g_I L_s}, \tag{6.9}$$

where Ω_B must be given in units of GHz. The fiber parameters dictate the beam quality of the incident beam which can be accepted by the fiber. According to ISO 11146[159], the beam quality parameter M^2 is defined as

$$M^2 = \frac{\pi}{\lambda}\frac{d_o \theta}{4}, \tag{6.10}$$

where d_o is the diameter of the beam waist and θ is the full beam divergence. To determine the beam quality a fiber could accept, let $\theta = 2NA$ and $d_o = 2a$. Since the fiber core cross-sectional area is $A = \pi a^2$, the beam quality acceptance of the fiber, $M^2 \approx \pi aNA / \lambda$, was substituted into equation (6.9) such that

$$P_{th} \approx \frac{21\Omega_B \lambda^2 M^4}{g_I \pi L_s}, \tag{6.11}$$

where Ω_B is in units of GHz for this equation.

Extrapolating the results of this work yielded a relationship between L_s and the fidelity of phase conjugation. From the method of measuring fidelity, it is expected that the measured fidelity will approach a constant as the fiber length increases beyond the lengths necessary for phase conjugation. For example, a flat-top beam would be expected to achieve a pinhole transmission of 0.22. At very long fiber lengths, the Spring model achieved rapidly oscillating values with an average of ~0.4. Using an exponential fit to the experimental data, the best fit curve approached 0.46. A simple fit to the experimental data was constructed using a Gaussian exponential function $c_1 + (1-c_1)Exp[-kL_s^2]$ such that the function returns perfect fidelity at $L_s = 0$ and a constant as L_s increases to infinity. Using Mathematica's "FindFit" function, a fit to the experimental data was determined,

$$F \approx 0.4585 + 0.5415 Exp[-0.001093 L_s{}^2], \tag{6.12}$$

where the constant in the exponential has the units of $(\text{m}\cdot\text{GHz})^{-2}$. This function is plotted against the combined experimental results in Fig. 70.

Solving Eq. (6.12) for L_s and substituting the result into Eq. (6.11) yields an expression for SBS threshold that is a function of beam quality accepted by the fiber and fidelity. The specific core area, length, and NA of the fiber have been replaced by beam quality acceptance and fidelity. Fig. 71 shows three curves of the SBS threshold power as a function of the maximum M^2 accepted by the fiber which is expected to yield fidelity in a range of values (0.95, 0.90, and 0.80), with $g_I \approx 3\times10^{-11}$ m/W, $\lambda = 1064$ nm, and $\Delta\lambda \approx 0.1$ nm.

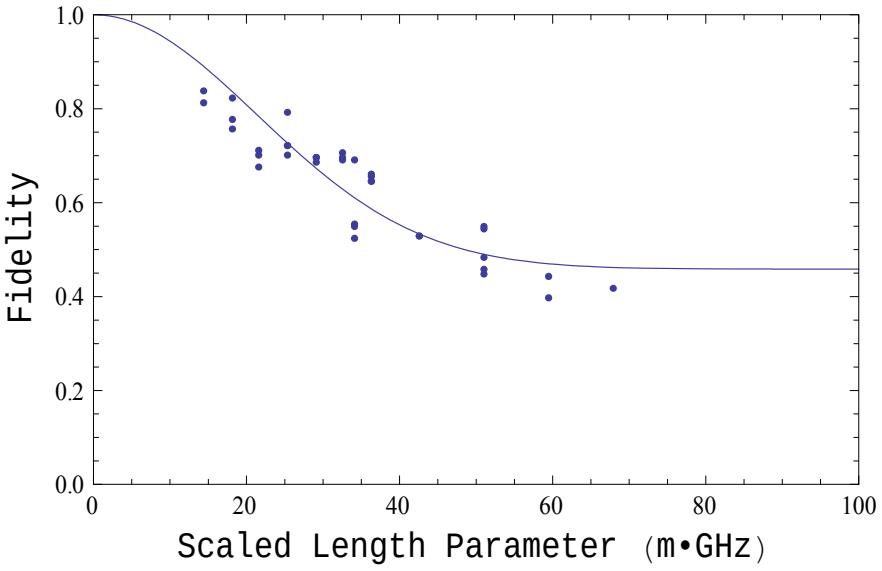

Fig. 70: Curve fit to experimental measurements of fidelity as a function of the scaled length parameter.

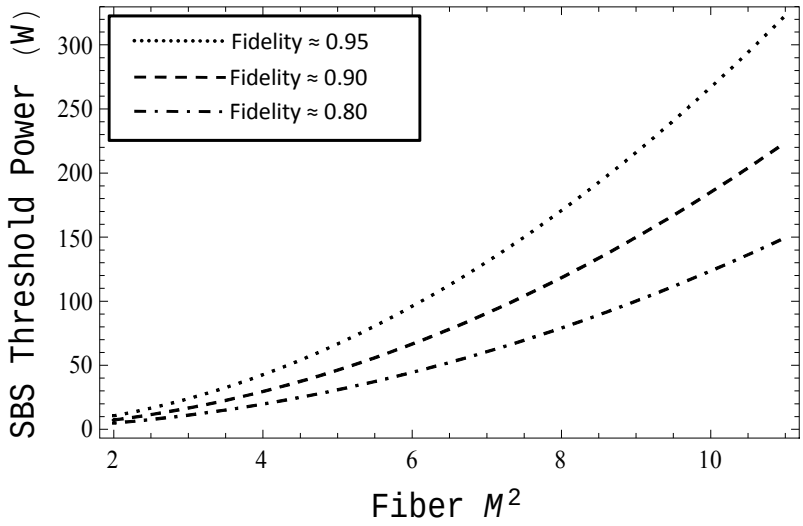

Fig. 71: SBS threshold power of silicate fiber for a given fidelity of phase conjugation as a function of the beam quality accepted by the fiber.

A reduced irradiance at an equivalent fidelity of phase conjugation can be realized when a fiber is chosen with the lowest NA possible that accepts the beam quality required. For the same M^2 value, a lower NA fiber requires a larger core area, but a

longer interaction length can be used to generate the same fidelity. The SBS threshold power is approximately equal, and the power is spread over a larger core area in the low NA fiber.

For example, the test fibers in this work were chosen to be multimode with a low SBS threshold. At 40-m length, the 0.06 NA fiber reached SBS threshold at ~14.5 W, while the 0.13 NA fiber reached threshold at ~16 W for a 15 m length. Both fibers achieved ~0.80 fidelity at these respective lengths, but the irradiance on the 0.06 NA fiber was reduced by a factor of four. Other fiber characteristics that effect the SBS gain coefficient such as the concentration of core dopants[164] and the SBS gain coefficient broadening are expected to have a secondary impact that was not included in this analysis.

To extend this analysis to fibers other than silica, the scaled length parameter was used to solve for the maximum phase difference as a function of fidelity from Eq. (6.7). The maximum phase difference was then assumed to be a constant for a given fidelity across all fiber materials such that $\Delta\phi^{(ch)}(F) = \Delta\phi^{(s)}(F)$ and

$$L_s^{(ch)}(F) = \frac{n^{(ch)}}{n^{(s)}} L_s^{(s)}(F), \tag{6.13}$$

where the scaled length parameter is shown explicitly as a function of fidelity, the superscript (s) denotes silica, and (ch) denotes chalcogenide or other fiber material of interest. The index of refraction of chalcogenide is ~2.8,[25] and that of tellurite is ~2.0.[165] Therefore, the scaled length parameter was determined to be a factor of ~1.9 longer for chalcogenide and ~1.3 for tellurite for a given fidelity of phase conjugation. This effect further reduces the threshold power necessary for a desired fidelity value in these fibers compared to silicate fiber. A plot of the SBS threshold power as a function

of beam quality acceptance is shown in Fig. 72 for three different fiber materials and a predicted fidelity of 0.9. The silicate fiber was assumed to be lossless, while the calculations for chalcogenide and tellurite fiber each include a low scattering loss estimate of 0.33 dB/m. Inclusion of the scattering loss required some loss of generality in this model due to the length-dependent loss. The NA of the tellurite and chalcogenide fibers was fixed at 0.22 and 0.18, respectively, and the beam quality acceptance varied with fiber core area only. For the purpose of comparing fiber materials shown in Fig. 72, these approximations are reasonable, but specific threshold calculations are necessary for fibers with non-negligible attenuation.

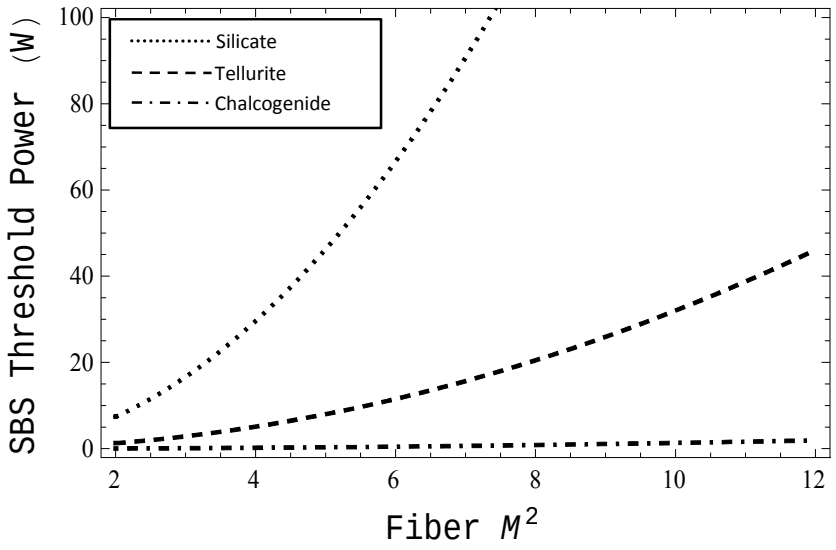

Fig. 72: Comparison of three different fiber materials showing the approximate SBS threshold power needed to generate a phase conjugate beam with fidelity of ~0.9, shown as a function of beam quality accepted by the fiber.

6.3. Effect of Fidelity on SBS Threshold

By analyzing the SBS threshold power measured during the cutback tests on the two silicate fibers, it was discovered that the effective Brillouin gain coefficient in

multimode fiber increases with phase conjugation fidelity. This effect lowers the SBS threshold below that expected using the Smith model as the fiber length decreases and phase conjugation is achieved. In fact, analysis of the SBS threshold as the fibers were shortened reinforces the phase conjugation fidelity measurements described in the previous section.

The experimental trials of Section 6.2 were analyzed to determine the SBS threshold of each trial as the two fibers were reduced in length. To determine threshold, the fiber transmission was plotted against Stokes power for each trial. When SBS threshold was reached, the Stokes power would rapidly increase while the power transmitting the fiber would remain relatively constant. Using the bin technique developed earler, the mean and standard deviation of the transmitted power was recorded for the Stokes power bin comprising all data points between 0.6 W and 1.0 W. An example of this technique is shown in Fig. 73. The transmitted power was then used to calculate the initial power coupled into the fiber. This was done first by assuming a Fresnel reflection of 4% at fiber exit face. The attenuation of the fiber was used to determine the coupled power just inside the entrance face of the fiber. The attenuation used in the calculation was the value provided by the manufacturer but verified using the cutback data.

The resulting threshold data was plotted as a function of fiber length for each of the two fibers. The Smith model, Eq. (2.53), with L_{eff} from Eq. (2.52), was plotted against the threshold data in these figures using the Brillouin gain coefficient as a fit parameter. The 0.13-NA fiber threshold data is shown in Fig. 74, and the 0.06-NA fiber is shown in Fig. 75. The standard deviation of the data to the fit was calculated at 1.4 W

for the data taken with the 0.13-NA fiber, considering deviations for the threshold power only, and 1.6 W for the 0.06-NA fiber.

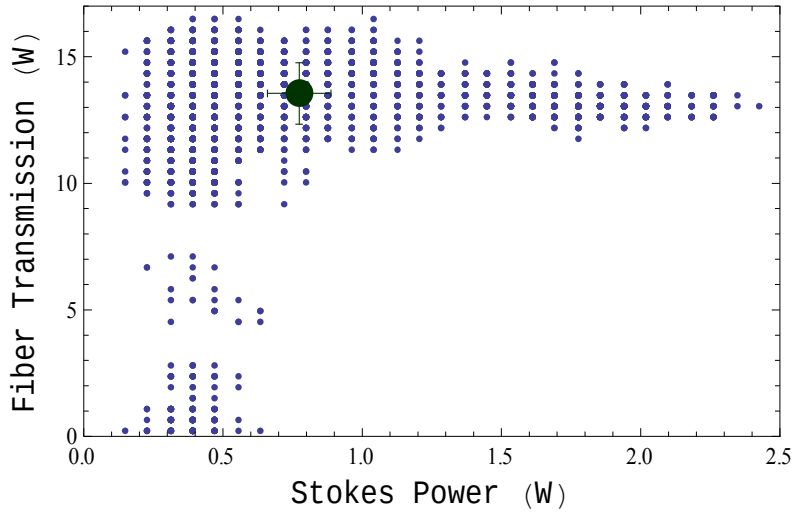

Fig. 73: Power transmitted through the test fiber plotted as a function of Stokes power to calculate SBS threshold.

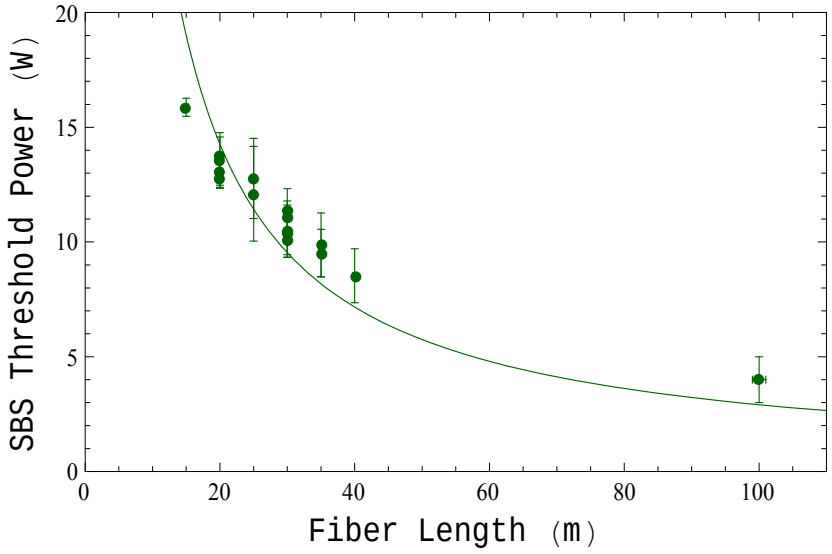

Fig. 74: SBS threshold measurements are plotted as a function of fiber length for the 0.13-NA fiber. The solid curve is the Smith model fit to the data.

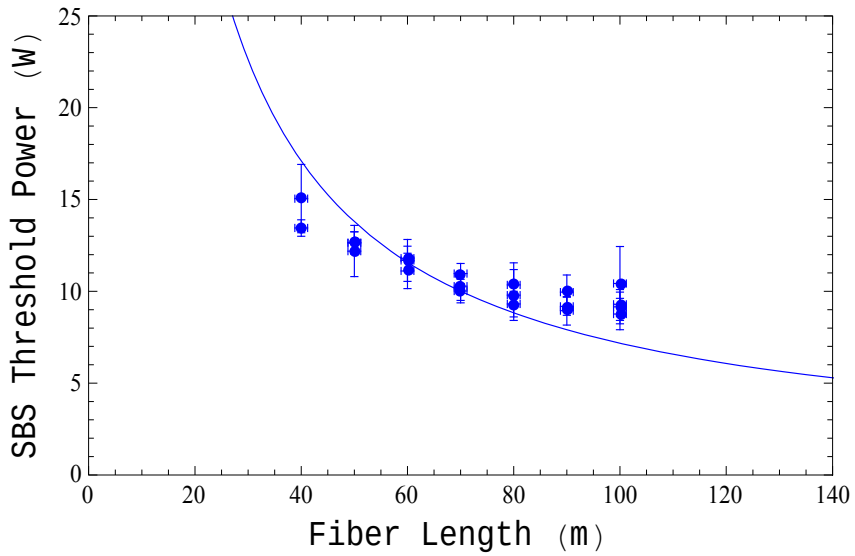

Fig. 75: The SBS threshold measured using the 0.06-NA fiber is plotted as a function of fiber length, as well as the Smith model fit to the data.

While SBS threshold has been examined at very short fiber lengths using pulsed lasers and km-length fibers using both pulsed and cw lasers, this work represents the first time the intermediate region has been examined. For single lengths of fiber, matching the Smith model to the data is a matter of solving for the Brillouin gain coefficient. However, taken as a set, the SBS threshold measured during the cutback tests did not increase as rapidly as predicted by the Smith model as the fiber was shortened.

Examination of Eq.(2.63) presented an improvement to the Smith model in this region, and the equation is shown again here

$$g_{eff}(z) = g_I \frac{\int G(r_\perp) I_s(r_\perp, z) I_b(r_\perp, z) dr_\perp}{P_s(z) P_b(z)}. \tag{6.14}$$

This equation predicts that the effective Brillouin gain coefficient increases with the overlap between signal and Stokes beams in the fiber. The phase conjugation fidelity also results from this overlap. While the exact overlap at long lengths of fiber is not

known, it does not drop to zero since both beams remain guided. The fidelity as measured by the in-line pinhole technique in this work was therefore used as an estimate of the overlap between the signal and Stokes beams as a function of fiber length. The Smith model was modified by multiplying the Brillouin gain coefficient by the fidelity of phase conjugation in Eq. (6.12) such that

$$P_{th} \approx \frac{21A}{F(L)g_1 L_{eff}}, \tag{6.15}$$

where *F(L)* is the fidelity generated by a given length of fiber, *L*. In Fig. 76 and Fig. 77, Eq. (6.15) is plotted against the threshold data for the 0.13-NA and 0.06-NA fibers, respectively. In these calculations, g_1 was used as a fit parameter and was set to 4.1×10^{-11} m/W for the 0.13-NA fiber and 5.3×10^{-11} m/W for the 0.06-NA fiber. The standard deviation of the fit was reduced to 0.5 W in both data sets.

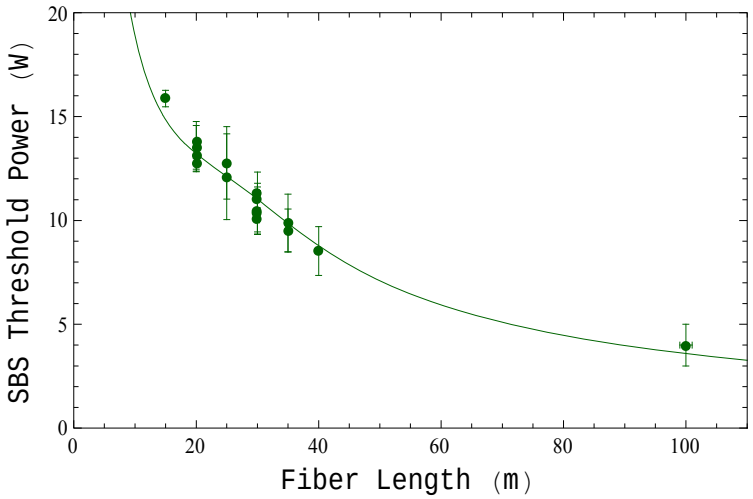

Fig. 76: The threshold data for the 0.13-NA fiber is shown with the threshold model from this work.

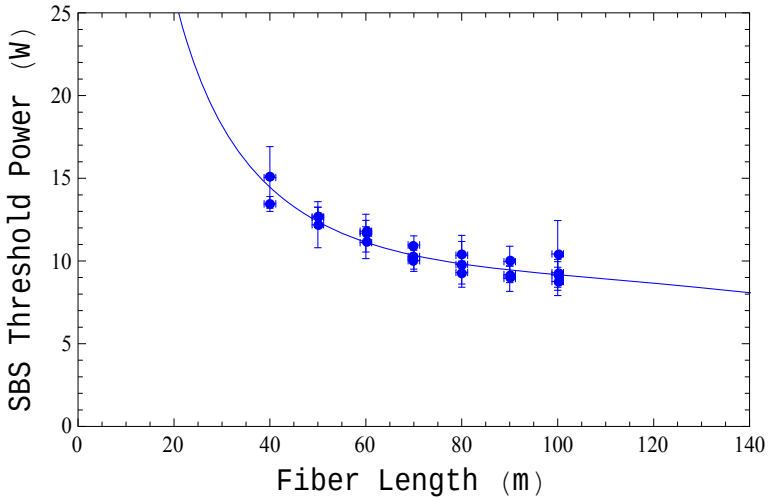

Fig. 77: The SBS threshold measurements for the 0.06-NA fiber are shown with a fit using this work's model.

The increase in the effective Brillouin gain coefficient resulting from increased phase-conjugation fidelity has not previously been documented. However, the same physics underlies both effects. For example, perfect phase conjugation results in a maximum fidelity value, and, by definition, results in a maximum value for the overlap integral in Eq. (6.14). In this way, the analysis of SBS threshold in the multimode fiber provided a secondary measure of the fidelity of phase conjugation.

6.4. Beam Combination in Chalcogenide Fiber

Using the results of this work, an apparatus was built to phase-lock two amplifier channels together using chalcogenide fiber and single-frequency amplifiers at a wavelength of 1550 nm. The apparatus is shown in Fig. 78. The pre-amplifiers were described in Chapter 4 which generated over 3 W of power in a narrow-linewidth, single-polarization, single-mode beam after isolation. The apparatus was identical to Fig. 46 except for the addition of fiber amplifiers in each leg. Each fiber amplifier was made

from a Nufern prototype Er-Yb co-doped fiber provided to AFIT by AFRL/RDLO. The fiber characteristics are shown in Table 6. The fiber amplifiers were each 7.5 m long and pumped with LIMO fiber-coupled diodes generating up to 100 W at 976 nm.

As shown in Table 6, the fiber supports 20 modes through a calculation of the V-parameter of the fiber. However, for this application, the number of modes must be reduced significantly for good coupling efficiency into the test fiber. One method to achieve this is by coupling into the fundamental mode of the fiber.[166] Since the beam

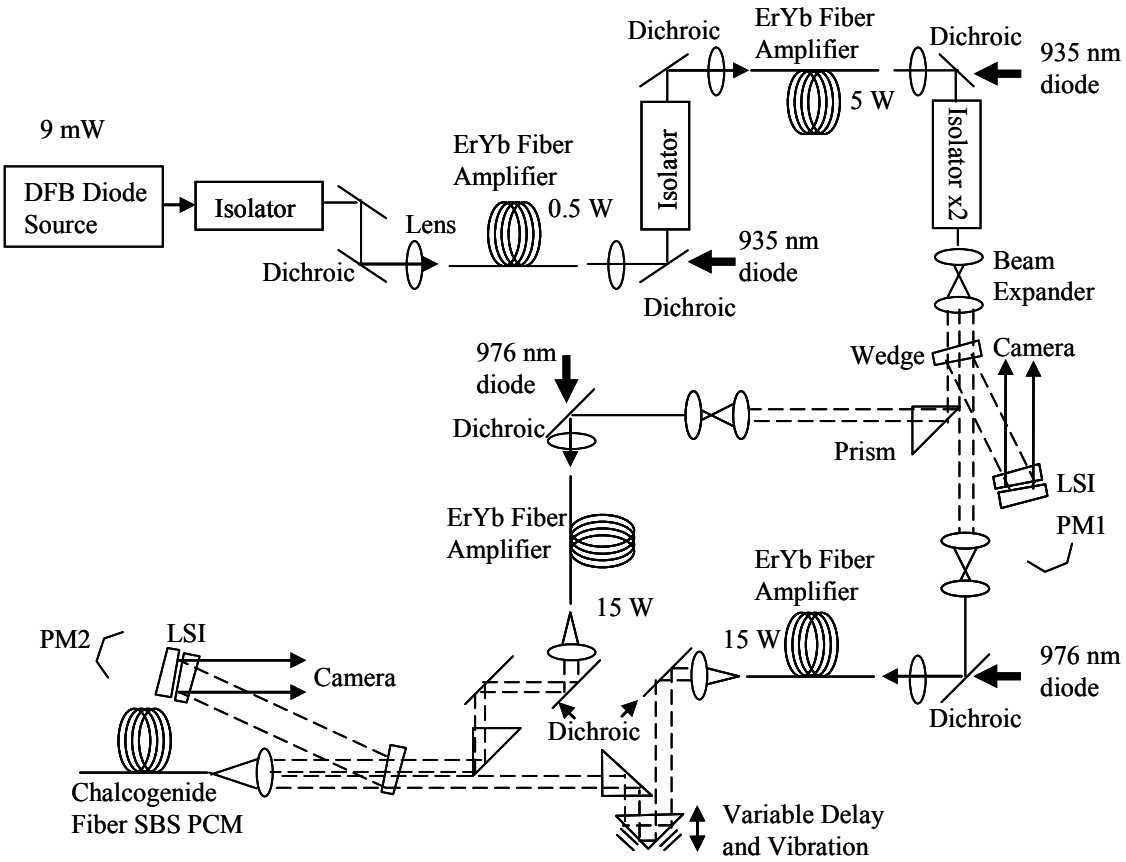

Fig. 78: Apparatus for beam-combination experiments via SBS phase conjugation in chalcogenide fiber at 1550-nm wavelength.

was wavefront-split by necessity, many high-order spatial frequencies existed in the seed which prevented efficient coupling to the fundamental mode of the fiber. The method implemented was to introduce significant bend-loss through coiling.[167] The low-order modes experience less attenuation than the higher-order modes when the fiber is bent. With a coil diameter of 10 cm, the divergence of the beam exiting the fiber was measured at 0.20 rad, full-width, at e^{-2} power, which is over twice the diffraction limit of 0.095 rad. In addition, the beam was clearly multi-mode. When coiled at a diameter of 1.6 cm, the divergence was reduced to 0.11 rad. With fine adjustment of the input coupling, a single-lobed beam could be maintained at this divergence.

The amplifiers were tested at low power to verify their performance relative to previous amplifier systems discussed in Chapter 4. The amplifier in channel 1 is shown in Fig. 79. The slope efficiency as a function of total pump power was 14%, and the ASE is significant in the region of 1060 nm with a 3% slope. Similarly, the amplifier in channel 2 is shown in Fig. 80. The slope efficiency at 1550 nm was 10% as a function of total pump power, and the ASE at 1060 nm had a slope of 3%. ASE in the vicinity of 1550 nm was suppressed below 30 dB during the tests. Since ASE at 1060 nm could damage the chalcogenide, two dichroic mirrors were used in the beam path between the

Table 6: Characteristics of Er-Yb co-doped fibers used in two-beam combination experiment.

	Er-Yb Fiber
Core diameter (μm)[a]	25
Core NA[a]	0.11
Cladding absorption ~975 nm (dB/m)[a]	2.1
Cladding diameter (μm)[a]	300
V parameter	5.6
Supported modes[b]	20

[a] Manufacturer supplied, Nufern
[b] Adams, M.J., *An introduction to optical waveguides*. 1981: Chichester: Wiley.

amplifiers and the test fiber to eliminate 99% of the power near 1060 nm wavelength. From these tests, it was estimated that the total power that could be generated from these amplifiers is approximately 20 W at full pump power.

A chalcogenide fiber was used for generating SBS, and the specifications are listed in Table 7. To determine the fidelity of phase conjugation expected from this fiber,

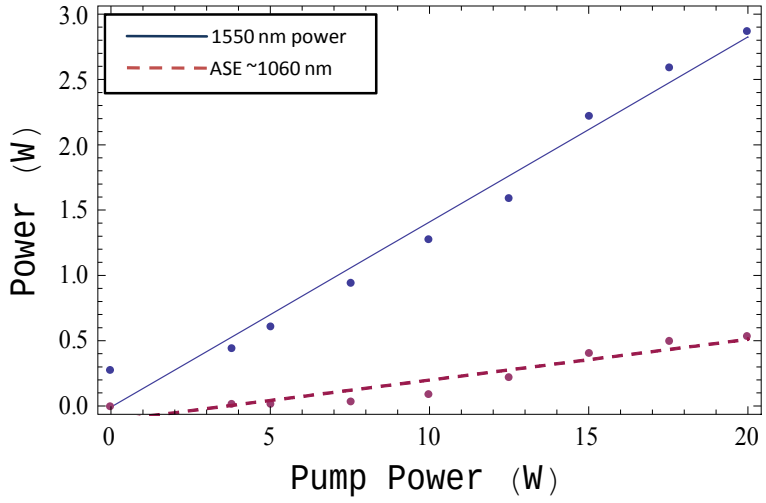

Fig. 79: Channel 1 Er-Yb fiber amplifier performance and ASE ~1060 nm as a function of pump power.

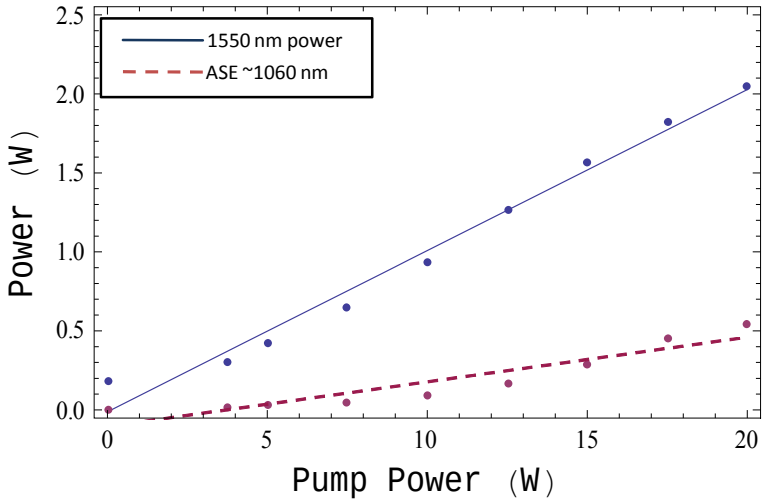

Fig. 80: Channel 2 Er-Yb fiber amplifier performance and ASE ~1060 nm as a function of pump power.

the scaled length parameter was compared to that of silicate fiber using Eq. (6.13). The approximate fidelity was then computed to be 0.85 by using Eq. (6.12). The SBS threshold of the fiber was computed at 2.5 W of coupled power using the measured attenuation and the threshold model described in Chapter 4. Due to the high index of refraction of ~2.8, the Fresnel reflection is calculated to be 22%. Both ends of the fiber were polished at 4º to divert the Fresnel reflections.

Coupling to the fiber was first attempted using a surrogate to test the coupling efficiency. A silicate fiber with a core diameter of 50 μm and an NA of 0.21 was inserted into the beam. The fiber was only a few meters long for the purpose of measuring coupled power, and a coupling efficiency of ~66% was achieved. The chalcogenide fiber supports more modes than the silicate fiber, but coupling into the chalcogenide fiber was slightly worse at $61+/-5\%$. This value was determined by using an aperture on the output end of the fiber to eliminate the cladding modes, and comparing that value to the total transmission including the cladding modes. This method assumes the cladding to be equally transmissive as the core. The surface quality of the chalcogenide fiber was not as

Table 7: Chalcogenide fiber characteristics.

	Chalcogenide Fiber
Core diameter (μm)[a]	65
Core NA[a]	0.18
Core attenuation ~1550 nm (dB/m)	0.33
V parameter	23.7
Fiber ~M^2 (V/2)	11.9
Length (m)	20
Stokes shift (GHz)[b]	8
Scaled Length Parameter (m·GHz)	32.6

[a] Manufacturer supplied, CorActive
[b] Abedin, K.S., *Single-frequency Brillouin lasing using single-mode As2Se3 chalcogenide fiber.* Optics Express, 2006. **14**(9): p. 4037-4042.

good as the polish obtained using silicate fiber, which may have been the cause of the decreased coupling efficiency. With this coupling efficiency and the Fresnel reflection of 22%, it was calculated that the incident power required to achieve SBS threshold was 5.3 W.

Four tests were conducted, and SBS threshold was not achieved. The transmission efficiency of the fiber decreased with increasing power as shown in Fig. 81. At low seed powers, the transmission efficiency exceeded 9% including fiber attenuation and Fresnel reflections. As power was increased, the transmission efficiency dropped to less than 4%. The decrease was reversible when power was decreased. For example, test 3 was conducted without material failure. Test 4 was conducted minutes later and exhibited the higher efficiency transmission at low powers before eventually failing at 3.5 W of seed power. Two forms of failure were observed: test 1 and 2 failed when the fiber tip ignited, but test 4 failed from the fiber softening and bending at the edge of the mount for the fiber tip. However, along with each failure, a segment of fiber approximately 1-m long was permanently damaged and required removal before polishing.

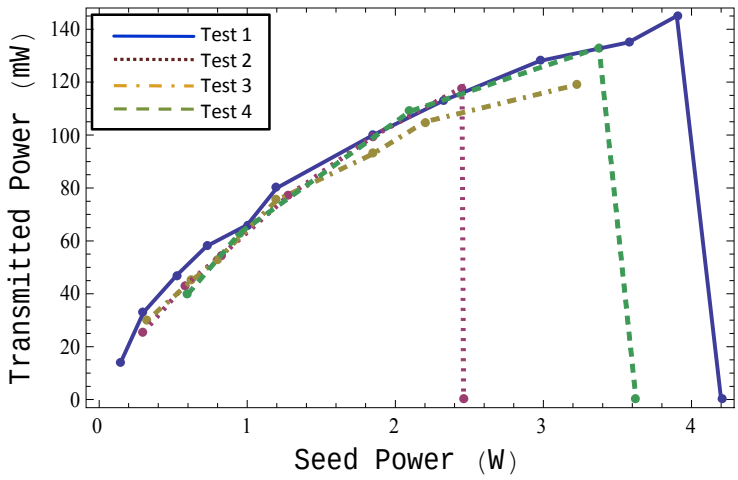

Fig. 81: Chalcogenide fiber transmission as a function of seed power. Zero power was recorded to indicate material failure.

The highest reported irradiance on chalcogenide fiber was $221\,kW/cm^2$ using a single-mode fiber.[25] This is approximately 3 times higher than the irradiance at failure during these tests. The decrease in transmission efficiency is believed to be a precursor to material failure. In this case, the increased attenuation shortens the effective length of the fiber as power is increased, which increases the SBS threshold accordingly.

6.5. Conclusions

High-fidelity, cw phase conjugation in step-index fiber was achieved for the first time, and is achievable with longer lengths of fiber than previously calculated. The increased fiber length reduces the SBS threshold and results in higher conversion efficiency from pump to Stokes for a set seed power. For the same beam quality supported by the fiber, a larger core area and lower NA is preferred to generate a high fidelity phase conjugate with lower pump irradiance. This mitigates damage concerns in phase conjugate laser systems.

The specific length of fiber that can be used to generate a given phase conjugate fidelity is inversely proportional to the square of the numerical aperture of the fiber as discussed in previous works. A relationship was established between the fidelity of phase conjugation and a scaled length parameter which is linearly related to the maximum phase difference among fiber modes. The fidelity of phase conjugation can be predicted from fiber parameters and material characteristics, and the SBS threshold power needed to achieve a desired fidelity can be approximated based on this work.

Through an analysis of the SBS threshold power, a new application of existing theory was discovered. Specifically, increases in fidelity represent improved overlap

between the signal and Stokes beams. This increase in the overlap reduces the predicted SBS threshold for lengths of fiber where phase conjugation occurs.

Using the results of this work, a beam-combination experiment using SBS in chalcogenide fiber was designed and experimentally tested. A degree of coherence of ~85% was expected from SBS in a multimode, chalcogenide fiber, but the fiber material failure limit was reached before SBS threshold. High power laser systems designed to use SBS beam combining must greatly exceed SBS threshold for efficient operation. Therefore, chalcogenide fiber must be used in pulsed systems only to avoid the thermal effects encountered in these experiments. Due to the scattering loss in the fiber, the interaction length is limited to approximately 20 m. This removes the possibility of using a fiber with a larger core, lower NA, and longer length to generate the phase conjugate beam with lower irradiance. Tellurite and silicate fiber provide a higher damage threshold to SBS threshold ratio for cw operation.

7. Conclusion

The objective of this work was to demonstrate the path to cw beam combination through SBS phase conjugation in optical fiber. One of the obstacles to cw phase conjugation was the high powers required to reach SBS threshold in the short, step-index fibers required to generate high fidelity phase conjugation according to the existing theories on phase conjugation fidelity and SBS threshold. Due to the high powers required, phase conjugation had only been achieved using pulsed laser systems and fibers of only a couple meters. Reports of phase conjugation in fibers longer than 10 m were rarely reported and often limited in effective length by the coherence length of the laser system. By contrast, phase conjugation using cw lasers had only been attempted using km-length fibers. While some researchers claimed cw phase conjugation had been achieved using long, graded-index fibers, additional experiments by other research groups and in this work negated these results.

The approach used in this work was to study cw, SBS, phase-conjugation fidelity achieved using intermediate lengths of multimode silicate fiber between 10 m and 100 m in length. A secondary approach was to study phase conjugation from more immature materials of tellurite and chalcogenide fibers which were recently reported to have much higher Brillouin gain coefficients, but much higher scattering losses as well. To accomplish this, an experiment was designed and implemented to generate a high-power, narrow-linewidth seed at 1064-nm wavelength and measure the fidelity of phase conjugation from SBS as the fibers were shortened. A second, narrow-linewidth laser was constructed at 1550-nm wavelength, and the material properties of chalcogenide and tellurite fibers were analyzed at both wavelengths. A model of SBS threshold was

adapted from existing work to include scattering losses and the flexible end-pumping configurations of fiber amplifiers. The model was used to design and build the amplifier systems at both wavelengths to avoid SBS, and it was used to ensure SBS threshold could be reached in the test fibers during phase conjugation experiments. The measurement of fidelity was also studied with particular attention paid to distinguishing beam cleanup from phase conjugation. Lastly, cw, beam combination via SBS phase conjugation was attempted using chalcogenide fiber at 1550-nm wavelength.

7.1. Significant Accomplishments

The model of SBS threshold in fiber amplifiers showed that co-pumping a fiber amplifier reduced the SBS threshold significantly over counter-pumping. When both ends are pumped, the SBS threshold is between the extreme cases of co-pumping and counter-pumping.

The SBS threshold model also showed the effect of scattering loss on SBS threshold is much more significant than predicted by the Smith model. The SBS threshold is higher than predicted by the Smith model as the level of scattering loss increases. This deviation was found to be significant for fibers with scattering losses exceeding 0.5 dB/m.

The fidelity study showed discrepancies in the fidelity measurements used in the literature when beam cleanup is a possibility. The in-line pinhole technique was shown to distinguish beam cleanup from phase conjugation, and this was confirmed in an experiment which generated SBS in a long, graded-index fiber. A more accurate measure of fidelity was developed and demonstrated using interference techniques.

CW phase conjugation was achieved for the first time. The increase in fidelity was measured as the fiber was shortened, and fidelity over 0.8 was measured using lengths of fiber approximately an order of magnitude longer than previously-existing models indicated. A correlation between the experimental data and modeling of three step-index fibers was shown based on a scaled length parameter. The scaled length parameter was related to the maximum phase difference between pump and Stokes modes in a fiber. The fidelity and threshold powers were then calculated based on fiber parameters for silicate fibers and other fiber materials, independent of exact fiber dimensions. Materials with a higher index of refraction and lower Stokes shift than silicate fiber of the same NA were predicted to achieve higher fidelity phase conjugation at longer lengths.

The phase conjugation fidelity was found to increase the effective Brillouin gain coefficient by increasing the overlap between seed and Stokes modes. As fidelity increased, the SBS threshold was measured lower than predicted by existing models. This work represents the first time this effect has been documented or predicted, even though the effect can be derived directly from the basic differential equations describing SBS.

7.2. Conclusions

For fiber amplifiers, the co-pumped configuration is the most-favored geometry due to engineering constraints. The diodes are protected from the amplified signal in this configuration. Pump combiners which fuse multiple pump-delivery fibers to the cladding of a single fiber amplifier may not work in the reverse direction, forcing a co-pumped configuration when the highest pump power can be delivered. When single-frequency

amplifiers are being constructed, the lower SBS threshold of the co-pumped geometry must be balanced with the other design constraints. Shortening the fiber amplifier, and applying a higher dopant concentration of active elements in a large mode area fiber are perhaps the simplest ways to avoid SBS threshold under these conditions. The shorter fiber presents less of an effective length for SBS, and the higher dopant concentration introduces a larger thermal gradient along the fiber, which mitigates SBS. In addition, when passive fibers with a high scattering loss (above 0.5 dB/m) are being used, the Smith model provides a lower bound to SBS threshold calculations since the approximations used in that model lose validity.

Graded-index fibers produce SBS beam cleanup, not phase conjugation, and this can be deceiving when measuring fidelity through methods common in the literature. For beam combining purposes, the interference technique should be used to measure fidelity, as spatial measures can be ambiguous.

The threshold power needed to achieve high-fidelity phase conjugation is approximately an order of magnitude lower than previously calculated. The irradiance required can be reduced further through the use of low-NA fibers. As the fidelity of phase conjugation increases, the effective Brillouin gain coefficient increases proportionately due to the increased overlap between the seed and Stokes beams. The increase in fidelity lowers the SBS threshold even further than calculated by the Smith model in short, step-index fibers. The lower threshold reduces the damage risk associated with such systems and increases the efficiency of cw beam combining using this technique by an order of magnitude over previous models.

This work demonstrates that beam combining via SBS phase conjugation in optical fiber is achievable. Using the results presented here, a laser system can be designed for high power and beam quality which takes into account the amplifier power, the SBS fiber characteristics, and the damage threshold of the materials. In such a system, the use of a different material as the phase conjugate mirror would avoid seeding the SBS process in the amplifiers. However, this effect should not degrade the coherence between the amplifier channels provided a spatial phase conjugate beam is generated in the SBS fiber.

7.3. Future Work

One such system would use a multimode tellurite fiber to conjugate two silicate fiber amplifiers. The apparatus is similar to Fig. 78, with two major differences. First, it should be constructed at 1064 nm wavelength to take advantage of the additional amplifier efficiency for the demonstration. Second, a 80/20, non-polarizing beam splitter should be inserted after the isolators but before the split into multiple channels. The 80/20 beam splitter should transmit only 20% and will serve as the output coupler for the laser system. A high-power pre-amplifier should be used to generate ~20 W before the splitter to enable sufficient power coupled to each amplifier for efficient seeding. The amplifiers should each be pumped with up to 200 W to generate at least 100 W of output power per channel.

To generate SBS, a low-loss tellurite fiber (0.33 dB/m or better) should be procured. The same dimensions of this work's chalcogenide fiber should be sufficient for ample coupling efficiency, since the number of modes supported by the fiber is increased with the switch to the shorter wavelength of 1064 nm. The 65-μm core fiber with an NA

of 0.18 is calculated to generate fidelity of 0.9 with a physical length of 7.7 m. The SBS gain coefficient is calculated to be $\sim 2.7\times10^{-10}$ m/W , and SBS threshold is calculated to be ~50 W for this length of fiber for an irradiance of 1.5 MW/cm^2. Longer lengths should be attempted first for testing purposes. If a coupling efficiency of 80% can be achieved into the tellurite fiber, threshold can be exceeded by a factor of 4, and each amplifier should be seeded on the return path with ~40 W at full power through SBS phase conjugation. After the second pass through the amplifiers, up to 200 W would be incident on the 80/20 beam splitter, and up to 160 W would be generated in two, mutually-coherent beams. The system efficiency in this prototype would be low, but would be scaled with the number of channels combined. Six channels could be combined using the "Gatlin-gun" combiner developed by Grime *et al*.[99] for coupling into the tellurite fiber.

An experiment should be conducted to verify the fidelity of phase conjugation predicted from non-silicate fibers. The maximum phase shift was used as a constant as a function of fidelity to compare different fibers, which adds the index of refraction into the computations of the scaled length parameter. Also, it is unknown whether the scattering loss in a fiber will cause an effective scaled length parameter shorter than calculated in this work. If so, the fidelity achieved should be higher than predicted. Two lengths of multimode tellurite fiber should be tested. The fibers should have the same geometry but different levels of scattering. A cutback test similar to this work should be conducted using an in-line pinhole to measure the fidelity. The results should be examined with particular attention to the effects of scattering loss and the relation between fidelity and maximum phase difference.

Hollow-core waveguides are commercially available with core diameter of 20 μm and an NA of 0.13 for use at 1550 nm.[168] Combined with the very small Stokes shift of methane or xenon of approximately 0.6 GHz at 1550 nm, a hollow-core guide filled with one of these gases could produce a phase conjugate beam with fidelity of 0.9 at lengths of ~140 m.[16, 169] The Brillouin gain coefficient of these gases at 10 atm is approximately 1×10^{-11} m/W , which increases to 44×10^{-11} m/W (65×10^{-11} m/W for CH_4) at 39 atm. Even at the lower pressure of 10 atm, the SBS threshold is calculated at 4.7 W with fidelity of 0.9. As a result of this work, the Brillouin gain coefficient alone is not the deciding metric on a material. In the case of these gases, the small Stokes shift enables much longer waveguide lengths and comparable reduction in threshold. A custom, large core waveguide should be used to increase the acceptance of the fiber. This technique would include the added benefits of hollow-core waveguides by eliminating damage concerns and significant Fresnel reflections at the fiber surface.

Glossary of Symbols

a	radius of the fiber core
A_{eff}	area of the confined power in a waveguide
$A^f(z)$	field amplitude of fiber mode f as a function of z
$\mathbf{B}$	magnetic induction
b	radius of the fiber cladding
C_δ	coefficient of the change in bandwidth with temperature
C_f	coefficient of the change in Brillouin frequency shift with temperature
$\mathbf{D}$	electric displacement
$\mathbf{E}$	electric field
$\mathbf{E}_\omega$	electric field at monochromatic frequency ω
$\hat{\mathbf{E}}_\omega$	electric field amplitude and polarization at frequency ω
$\hat{E}_\omega$	electric field amplitude at frequency ω
$\hat{\mathbf{e}}$	unit vector in direction of electric field polarization
F	fidelity, ratio of power that is in the phase conjugate mode to total power
F_o	room temperature Brillouin frequency shift
F_c	frequency parameter of the NA-broadened Brillouin gain coefficient
F_v	Stokes beam frequency
g	laser or amplifier gain
g_o	peak Brillouin gain coefficient
$g_B(\Omega)$	homogeneously broadened Brillouin gain coefficient
$g_b(z,F)$	temperature broadened Brillouin gain coefficient
g_{eff}	effective Brillouin gain due to radial integral of pump and Stokes beams
$g_I(\Omega)$	inhomogeneously broadened Brillouin gain coefficient
G_B	total Brillouin gain
$G(r_\perp)$	radially dependent Brillouin gain factor
G_L	total laser gain
G_s	total scattering loss
$\mathbf{H}$	magnetic field
h	fiber convective coefficient
$\hbar$	Planck's constant divided by 2π
I	intensity, power per unit area
K	numerical factor representing frequency permutations and factors of 1/2
K_g	polarization factor used with Brillouin gain coefficient
$\boldsymbol{k}$	wave vector
$\mathbf{K_B}$	Brillouin acoustic wave wave vector
l	path length
L	fiber length, also L_{fiber}
L_{eff}	effective length of the SBS interaction
L_{coh}^s	coherence length of the signal laser

L_s	scaled length parameter equal to $L\Omega_B NA^2$
M	scalar term related to irradiance pattern of SBS pump
M^2	beam quality as defined by ISO 11146
N	molecular density
n	index of refraction
NA	numerical aperture or acceptance half-angle
N_w	number of excited waveguide modes
$\mathbf{P}$	electric polarization, dipole moment per unit volume
$\mathbf{P^{(n)}}$	electric polarization, dipole moment per unit volume, nth-order
$\mathbf{P_\omega}$	electric polarization at frequency ω
P	power (Watts)
P_{st}	saturation power
p_{st}	strictive pressure
P_s	signal power
P_B	Stokes power
P_p	pump power
$P_{pf(b)}$	pump power incident from the front (back) of the fiber
R	reflectivity
T	temperature
u	potential energy per unit volume
V	normalized frequency parameter of a fiber
$V(q)$	visibility of fringes in vicinity of point q
W	work
w_o	beam waist
z	longitudinal position
α	loss or attenuation coefficient, s=scattering, Yb=Ytterbium absorption
β^f	propagation constant of mode f
Γ_{fg}	linewidth of photon transition
Γ_B	Brillouin resonance natural linewidth
γ	pump power to laser gain conversion coefficient
$\lvert\gamma_{12}(\tau)\rvert$	degree of coherence due to pathlength difference τ
γ_e	electrostrictive constant
δ	phase error or piston error in radians
ε	electric permittivity
ε_o	permittivity of free space
ϕ	phase factor of electric field
η	quantum defect
η_{sl}	slope efficiency of amplifier above threshold
θ	angle between signal and Stokes beams
$\theta_{1/2}$	acceptance half-angle of a fiber
$\kappa(z)$	field amplitude longitudinal dependence for all modes
Λ	acoustic wavelength
λ	wavelength
μ	magnetic permeability

μ	statistical mean
v_a	acoustic frequency
$v_{p(s)}$	electric field frequency of the pump (Stokes) beams
ρ	material density
σ	standard deviation
τ	pathlength difference equal to
$\chi^{(n)}$	susceptibility tensor, nth order
$\psi^f(r_\perp)$	electric field radial and azimuthal dependence for mode f
Ω	difference in angular frequency between signal and Stokes beams
Ω_B	acoustic wave frequency due to SBS interaction
Ω_{Bo}	acoustic wave frequency from SBS directly backscattered
Ω_{fg}	phonon transition frequency, homogeneously broadened
ω	angular frequency (rad/s)
ω_b	Stokes frequency
ω_s	signal frequency
ω_σ	sum frequency

Bibliography

1. R. Wall, "Run-up to war," Aviation Week and Space Technology **158**, 44-49 (2003).

2. MDALink, "Advanced Discriminating Ladar Technology," (Missile Defense Agency, 2007), www.mda.mil/mdalink/html/asptadlt.html, Accessed 13 April 2007.

3. F. Liégeois, C. Vercambre, Y. Hernandez, M. Salhi, and D. Giannone, "Pulsed high-peak-power and single-frequency fibre laser design for LIDAR aircraft safety application," Proceedings of SPIE **6367**, 63670H (2006).

4. H. Stephens, "Toward a new laser era," Journal of the Air Force Association **89**, 1-8 (2006).

5. R. Q. Fugate, "The Starfire Optical Range 3.5-m adaptive optical telescope," Proceedings of SPIE **4837**, 934-943 (2003).

6. D. M. Pepper, "Nonlinear optical phase conjugation," Optical Engineering **21**, 156-183 (1982).

7. H. Bruesselbach, D. C. Jones, D. A. Rockwell, R. C. Lind, and G. Vogel, "Real-time atmospheric compensation by stimulated Brillouin-scattering phase conjugation," J. Opt. Soc. Am. B **12**, 1434-1447 (1995).

8. V. P. Gapontsev, "New Milestones in the development of super high power fiber lasers," Photonics West, OE/LASE, 21-26 (2006).

9. A. Galvanauskas, "High Power Fiber Lasers," Optics and Photonics News **15**, 42-47 (2004).

10. T. Y. Fan, "Laser beam combining for high-power, high-radiance sources," Selected Topics in Quantum Electronics, IEEE Journal of **11**, 567-577 (2005).

11. Y. Jeong, D. B. S. Soh, C. A. Codemard, P. Dupriez, C. Farrell, V. Philippov, J. K. Sahu, D. J. Richardson, J. Nilsson, and D. J. Payne, "State of the art of cw fibre lasers," (2005).

12. Y. Jeong, J. Nilsson, J. K. Sahu, D. N. Payne, R. Horley, L. M. B. Hickey, and P. W. Turner, "Power scaling of single-frequency ytterbium-doped fiber master-oscillator power-amplifier sources up to 500W," IEEE J. Sel. Top. Quantum Electron. **13**, 546-551 (2007).

13. D. M. Pepper, "Applications of optical phase conjugation," Scientific American **254**, 74-83 (1986).

14. J. D. Jackson 3rd, *Classical Electrodynamics, 3rd edn, 671* (Wiley & Sons, New York, 1998).

15. P. N. Butcher, and D. Cotter, *The Elements of Nonlinear Optics* (Cambridge University Press, 1990).

16. R. W. Boyd, *Nonlinear Optics* (Academic Press, 2003).

17. W. Demtröder, *Laser Spectroscopy: Basic Concepts and Instrumentation* (Springer, 2002).

18. A. Yariv, and P. Yeh, *Optical Waves in Crystals* (Wiley New York, 2003).

19. R. G. Smith, "Optical power handling capacity of low loss optical fibers as determined by stimulated Raman and Brillouin scattering," Applied Optics **11**, 2489-2494 (1972).

20. R. H. Stolen, "Nonlinearity in fiber transmission," Proceedings of the IEEE **68**, 1232-1236 (1980).

21. D. Marcuse, "Loss analysis of single-mode fiber splices," Bell Syst. Tech. J **56**, 703–718 (1977).

22. A. Mocofanescu, L. Wang, R. Jain, K. Shaw, A. Gavrielides, P. Peterson, and M. Sharma, "SBS threshold for single mode and multimode GRIN fibers in an all fiber configuration," Optics Express **13**, 2019-2024 (2005).

23. M. O. van Deventer, and A. J. Boot, "Polarization properties of stimulated Brillouin scattering in single-mode fibers," Journal of Lightwave Technology **12**, 585-590 (1994).

24. R. H. Stolen, "Polarization Effects in Fiber Raman and Brillouin Lasers," IEEE JOURNAL OF QUANTUM ELECTRONICS **15**, 1157 (1979).

25. K. S. Abedin, "Observation of strong stimulated Brillouin scattering in single-mode As2Se3 chalcogenide fiber," Optics Express **13**, 10266-10271 (2005).

26. K. S. Abedin, "Stimulated Brillouin scattering in single-mode tellurite glass fiber," Opt. Express **11**, 2641-2645 (2003).

27. J. S. Sanghera, C. M. Florea, L. B. Shaw, P. Pureza, V. Q. Nguyen, M. Bashkansky, Z. Dutton, and I. D. Aggarwal, "Non-linear properties of chalcogenide glasses and fibers," Journal of Non-Crystalline Solids **354**, 462-467 (2008).

28. J. B. Spring, T. H. Russell, T. M. Shay, R. W. Berdine, A. D. Sanchez, B. G. Ward, and W. B. Roh, "Comparison of stimulated Brillouin scattering thresholds

and spectra in nonpolarization-maintaining and polarization-maintaining passive fibers," Proceedings of SPIE **5709**, 147 (2005).

29. R. W. Hellwarth, "Theory of phase conjugation by stimulated scattering in a waveguide," Journal of the Optical Society of America **68**, 1050 (1978).

30. V. I. Kovalev, and R. G. Harrison, "Waveguide-induced inhomogeneous spectral broadening of stimulated Brillouin scattering in optical fiber," Optics Letters **27**, 2022 (2002).

31. Y. Imai, and N. Shimada, "Dependence of stimulated Brillouin scattering on temperaturedistribution in polarization-maintaining fibers," Photonics Technology Letters, IEEE **5**, 1335-1337 (1993).

32. Y. Li, F. Zhang, and T. Yoshino, "Wide-Range Temperature Dependence of Brillouin Shift in a Dispersion-Shifted Fiber and Its Annealing Effect," JOURNAL OF LIGHTWAVE TECHNOLOGY **21**, 1663 (2003).

33. Q. Yu, X. Bao, and L. Chen, "Temperature dependence of Brillouin frequency, power, and bandwidth in panda, bow-tie, and tiger polarization-maintainingfibers," Optics Letters **29**, 17-19 (2004).

34. J. Hansryd, F. Dross, M. Westlund, P. A. Andrekson, and S. N. Knudsen, "Increase of the SBS threshold in a short highly nonlinear fiber byapplying a temperature distribution," Lightwave Technology, Journal of **19**, 1691-1697 (2001).

35. K. Shiraki, M. Ohashi, and M. Tateda, "SBS threshold of a fiber with a Brillouin frequency shift distribution," Lightwave Technology, Journal of **14**, 50-57 (1996).

36. X. P. Mao, R. W. Tkach, A. R. Chraplyvy, R. M. Jopson, and R. M. Derosier, "Stimulated Brillouin threshold dependence on fiber type and uniformity," IEEE Photonics Technology Letters **4**, 66-69 (1992).

37. C. C. Lee, and S. Chi, "Measurement of stimulated-Brillouin-scattering threshold forvarious types of fibers using Brillouin optical-time-domain reflectometer," Photonics Technology Letters, IEEE **12**, 672-674 (2000).

38. A. Liem, J. Limpert, H. Zellmer, and A. Tünnermann, "100-W single-frequency master-oscillator fiber power amplifier," Optics Letters **28**, 1537-1539 (2003).

39. Y. Jeong, J. K. Sahu, S. Baek, C. Alegria, C. A. Codemard, D. B. S. Soh, V. Philippov, R. B. Williams, K. Furusawa, and D. J. Richardson, "The rising power of fibre lasers," in *IEEE/LEOS Annual Meeting*(Tuscon, AZ, 2003).

40. N. A. Brilliant, "Stimulated Brillouin scattering in a dual-clad fiber amplifier," Journal of the Optical Society of America B **19**, 2551-2557 (2002).

41. C. N. Pannell, P. S. J. Russell, and T. P. Newson, "Stimulated Brillouin scattering in optical fibers: the effects of optical amplification," J. Opt. Soc. Amer. B **10**, 684–690 (1993).

42. A. Heuer, C. Haenisch, and R. Menzel, "New concept for low-threshold optical phase conjugation via SBS in a fiber amplifier," Proceedings of SPIE **4972**, 151 (2003).

43. B. Y. Zel'dovich, Y. E. Kapitskii, V. A. Krivoshchenkov, A. N. Pilipetskii, N. F. Pilipetskii, and V. V. Shkunov, "Stimulated Brillouin scattering in a fiber waveguide with linear amplification," Quantum Electronics **17**, 1604-1607 (1987).

44. D. C. Brown, H. J. Hoffman, A. L. Syst, and P. A. Brackney, "Thermal, stress, and thermo-optic effects in high average power double-clad silica fiber lasers," Quantum Electronics, IEEE Journal of **37**, 207-217 (2001).

45. V. I. Kovalev, and R. G. Harrison, "Suppression of stimulated Brillouin scattering in high-power single-frequency fiber amplifiers," Optics Letters **31**, 161-163 (2006).

46. D. A. Rockwell, "A review of phase-conjugate solid-state lasers," Quantum Electronics, IEEE Journal of **24**, 1124-1140 (1988).

47. "3.5-Meter Telescope," (United States Air Force, 2001), Accessed 15 May, 2008.

48. X. Levecq, "Adaptive Optics: Optical fuse protects intracavity laser components," in *Laser Focus World*(2008).

49. D. L. Fried, "Branch point problem in adaptive optics," **15**, 2759-2768 (1998).

50. F. A. Starikov, G. G. Kochemasov, S. M. Kulikov, A. N. Manachinsky, N. V. Maslov, A. V. Ogorodnikov, S. A. Sukharev, V. P. Aksenov, I. V. Izmailov, and F. Y. Kanev, "Wavefront reconstruction of an optical vortex by a Hartmann-Shack sensor," **32**, 2291-2293 (2007).

51. K. L. Baker, E. A. Stappaerts, S. C. Wilks, P. E. Young, D. T. Gavel, J. W. Tucker, D. A. Silva, and S. S. Olivier, "Open-and closed-loop aberration correction by use of a quadrature interferometric wave-front sensor," **29**, 47-49 (2004).

52. T. M. Venema, and J. D. Schmidt, "Optical phase unwrapping in the presence of branch points," **16**, 6985-6998 (2008).

53. B. Y. Zel'Dovich, V. I. Popovichev, V. V. Ragul'Skii, and F. S. Faizullov, "Connection between the wave fronts of the reflected and exciting light in stimulated Mandel'shtem-Brillouin scattering," Journal of Experimental and Theoretical Physics Letters **15**, 109 (1972).

54. G. P. Agrawal, *Nonlinear Fiber Optics* (Academic Press, 2001).

55. T. H. Russell, B. W. Grime, T. G. Alley, and W. B. Roh, "Stimulated Brillouin scattering beam cleanup and combining in optical fiber," in *Nonlinear Optics and Applications*, H. A. Abdeldayem, and D. O. Frazier, eds. (Research Signpost, Kerala, India, 2007), pp. 179-206.

56. T. H. Russell, "Step-index fiber irradiance pattern," (Air Force Institute of Technology, Wright-Patterson AFB, 2007).

57. B. Y. Zel'dovich, V.V. Shkunov, Soviet Journal of Quantum Electronics **4**, 610–615 (1977).

58. D. Gloge, "Weakly guiding fibers," Appl. Opt **10**, 2252-2258 (1971).

59. M. Gower, and D. Proch, *Optical Phase Conjugation* (Springer, 1994).

60. E. A. Kuzin, M. P. Petrov, and B. E. Davydenko, "Phase conjugation in an optical fibre," Optical and Quantum Electronics **17**, 393-397 (1985).

61. Y. P. Vasil'ev, P. S. Razenshtein, and E. I. Shklovskii, "Stimulated Brillouin scattering mirror in the form of a multimode optical fiber in a four-pass neodymium phosphate glass laser amplifier," Quantum Electronics **15**, 1417-1418 (1985).

62. H. J. Eichler, J. Kunde, and B. Liu, "Quartz fibre phase conjugators with high fidelity and reflectivity," Optics Communications **139**, 327-334 (1997).

63. J. Spring, "Modeling of SBS Phase Conjugation in Multimode Step Index Fibers," in *Dept of Engineering Physics*(Air Force Institute of Technology, Air University, 2008), pp. 40-89.

64. L. Lombard, A. Brignon, J. P. Huignard, E. Lallier, and P. Georges, "Beam cleanup in a self-aligned gradient-index Brillouin cavity for high-power multimode fiber amplifiers," Optics Letters **31**, 158-160 (2006).

65. B. C. Rodgers, T. H. Russell, and W. B. Roh, "Laser beam combining and cleanup by stimulated Brillouin scattering in a multimode optical fiber," Opt. Lett **24**, 1124-1126 (1999).

66. O. Y. Nosach, V. I. Popovichev, V. V. Ragul'Skii, and F. S. Faizullov, "Cancellation of phase distortions in an amplifying medium with a" Brillouin mirror"," Journal of Experimental and Theoretical Physics Letters **16**, 435 (1972).

67. V. Wang, and C. R. Giuliano, "Correction of phase aberrations via stimulated Brillouin scattering," Optics Letters **2** (1978).

68. V. I. Kovalev, V. I. Popovichev, V. V. Ragul'skii, and F. S. Faizullov, "Gain and line width in stimulated Brillouin scattering in gases," Quantum Electronics **2**, 69-71 (1972).

69. D. Pohl, and W. Kaiser, "Time-resolved investigations of stimulated Brillouin scattering in transparent and absorbing media: determination of phonon lifetimes," Physical Review B **1**, 31-43 (1970).

70. E. P. Ippen, and R. H. Stolen, "Stimulated Brillouin scattering in optical fiber," Applied Physics Letters **21**, 539-541 (1972).

71. H. J. Eichler, A. Haase, and R. Menzel, "100-watt average output power 1.2 diffraction limited beam frompulsed neodymium single-rod amplifier with SBS phase conjugation," Quantum Electronics, IEEE Journal of **31**, 1265-1269 (1995).

72. W. Koechner, *Solid-State Laser Engineering* (Springer, 1999).

73. H. L. Offerhaus, and H. P. Godfried, "All solid-state diode pumped Nd: Yag MOPA with stimulated Brillouin phase conjugate mirror," Lasers and Electro-optics Europe, 1996. CLEO/Europe., Conference on, 6-6 (1996).

74. C. B. Dane, L. E. Zapata, W. A. Neuman, M. A. Norton, and L. A. Hackel, "Design and operation of a 150 W near diffraction-limited laser amplifier with SBS wavefront correction," Quantum Electronics, IEEE Journal of **31**, 148-163 (1995).

75. S. Amano, and T. Mochizuki, "High average and high peak brightness slab laser," Quantum Electronics, IEEE Journal of **37**, 296-303 (2001).

76. G. J. Crofts, M. J. Damzen, and R. A. Lamb, "Experimental and theoretical investigation of two-cell stimulated-Brillouin-scattering systems," J. Opt. Soc. Am. B **8**, 2282-2288 (1991).

77. J. Munch, R. Wuerker, and M. Lefebvre, "Interaction length for optical phase conjugation by stimulated Brillouin scattering- An experimental investigation," Applied Optics **28**, 3099-3105 (1989).

78. M. T. Duignan, B. J. Feldman, and W. T. Whitney, "Threshold reduction for stimulated Brillouin scattering using a multipass Herriott cell," J. Opt. Soc. Am. B **9**, 548-559 (1992).

79. A. M. Scott, and W. T. Whitney, "Characteristics of a Brillouin ring resonator used for phase conjugation at 2.1 mm," J. Opt. Soc. Am.(B) **12**, 1634-1641 (1995).

80. H. Meng, and H. J. Eichler, "Nd: YAG laser with a phase-conjugating mirror based on stimulated Brillouin scattering in SF6 gas," Opt. Lett **16**, 569-571 (1991).

81. H. S. Kim, S. H. Kim, D. K. Ko, G. Lim, B. H. Cha, and J. Lee, "Threshold reduction of stimulated Brillouin scattering by the enhanced Stokes noise initiation," Applied Physics Letters **74**, 1358 (1999).

82. L. P. Schelonka, and C. M. Clayton, "Effect of focal intensity on stimulated-Brillouin-scattering reflectivity and fidelity," Opt. Lett **13**, 42–44 (1988).

83. N. G. Basov, V. F. Efimkov, I. G. Zubarev, A. V. Kotov, A. B. Mironov, S. I. Mikhailov, and M. G. Smirnov, "Influence of certain radiation parameters on wavefront reversal of a pump wave in a Brillouin mirror," Quantum Electronics **9**, 455-458 (1979).

84. M. S. M. D. Crispin Jones, D.A. Rockwell, "A stimulated Brillouin scattering phase-conjugate mirror having a peak-power threshold <100W," Optics Communications **123**, 175-181 (1996).

85. V. R. Belan, A. G. Lazarenko, V. M. Nikitin, and A. V. Polyakov, "Stimulated Brillouin scattering mirrors made of capillary waveguides," Quantum Electronics **17**, 122-124 (1987).

86. P. Shalev, S. M. Jackel, R. Lallouz, and A. Bornstein, "Low-threshold phase conjugate mirrors based on position-insensitive tapered waveguides," Optical Engineering **33**, 278 (1994).

87. V. Pashinin, V. Sturm, V. Tumorin, and R. Noll, "Stimulated Brillouin scattering of Q-switched laser pulses in large-core optical fibres," Optics and Laser Technology **33**, 617-622 (2001).

88. H. Yoshida, H. Fujita, and M. Nakatsuka, "Optical damage threshold due to stimulated Brillouin scattering reflection with multimode optical fiber," Jpn. J. Appl. Phys **42**, 2735-2736 (2003).

89. H. J. Eichler, A. Mocofanescu, T. Riesbeck, E. Risse, and D. Bedau, "Stimulated Brillouin scattering in multimode fibers for optical phase conjugation," Optics Communications **208**, 427-431 (2002).

90. H. J. Eichler, J. Kunde, and B. Liu, "Fiber phase conjugators at 1064-nm, 532-nm, and 355-nm wavelengths," Optics Letters **22**, 495-497 (1997).

91. T. Riesbeck, E. Risse, and H. J. Eichler, "Pulsed solid state laser systems with high brightness by fiber phase conjugation," Proceedings of SPIE **5120**, 494-499 (2002).

92. T. Riesbeck, E. Risse, and H. J. Eichler, "Pulsed solid-state laser system with fiber phase conjugation and 315 W average output power," Applied Physics B: Lasers and Optics **73**, 847-849 (2001).

93. A. Heuer, and R. Menzel, "Phase-conjugating stimulated Brillouin scattering mirror for low powers and reflectivities above 90% in an internally tapered optical fiber," Opt. Lett **23**, 834-836 (1998).

94. M. Dämmig, G. Zinner, F. Mitschke, and H. Welling, "Stimulated Brillouin scattering in fibers with and without external feedback," Physical Review A **48**, 3301-3309 (1993).

95. V. I. Kovalev, and I. R. G. Harrison, "Temporally stable CW phase conjugation via stimulated Brillouin scattering in optical fiber with cavity feedback," Optics Letters **30**, 1375-1377 (2004).

96. C. Hänisch, A. Heuer, and R. Menzel, "Threshold reduction of stimulated Brillouin scattering (SBS) using fiber loop schemes," Applied Physics B: Lasers and Optics **73**, 851-854 (2001).

97. H. Bruesselbach, "Beam cleanup using stimulated Brillouin scattering in multimode fibers," in *Conference on Lasers and Electro-Optics*(Optical Society of America, 1993), pp. 424-426.

98. T. H. Russell, "Laser intensity scaling through stimulated scattering in optical fibers," in *Department of Engineering Physics*(Air University, AFIT, Wright-Patterson AFB, 2001).

99. B. W. Grime, "Multiple channel laser beam combination and phasing using stimulated Brillouin scattering in optical fibers," in *Department of Engineering Physics*(Air University, AFIT, Wright-Patterson AFB, 2005).

100. R. G. Harrison, and V. I. Kovalev, "SBS self-phase conjugation of CW Nd: YAG laser radiation in an optical fibre," Lasers and Electro-Optics, 1999. CLEO'99. Summaries of Papers Presented at the Conference on, 275-276 (1999).

101. V. I. Kovalev, and R. G. Harrison, "The build up of stimulated Brillouin scattering excited by pulsed pump radiation in a long optical fibre," in *Lasers and Electro-Optics Europe* (2000), p. 1.

102. V. I. Kovalev, and R. G. Harrison, "CW phase conjugation in optical fibres," in *Lasers and Electro-Optics Europe*(2005), p. 176.

103. V. I. Kovalev, R. G. Harrison, and A. M. Scott, "300 W quasi-continuous-wave diffraction-limited output from a diode-pumped Nd: YAG master oscillator power amplifier with fiber phase-conjugate stimulated Brillouin scattering mirror," Optics Letters **30**, 3386-3388 (2005).

104. V. I. Kovalev, R. G. Harrison, J. K. Sahu, and J. Nilsson, "Continuous-wave all-fiber MOPA with SBS phase conjugate mirror," Proceedings of SPIE **5335**, 46 (2004).

105. A. Mocofanescu, and K. D. Shaw, "Stimulated Brillouin scattering phase conjugating properties of long multimode optical fibers," Optics communications **266**, 307-316 (2006).

106. A. Heuer, C. Hänisch, and R. Menzel, "Low-power phase conjugation based on stimulated Brillouin scattering in fiber amplifiers," Optics Letters **28**, 34-36 (2003).

107. R. E. Slusher, G. Lenz, J. Hodelin, J. Sanghera, L. B. Shaw, and I. D. Aggarwal, "Large Raman gain and nonlinear phase shifts in high-purity As 2 Se 3 chalcogenide fibers," J. Opt. Soc. Am. B **21**, 1146-1155 (2004).

108. R. Mossadegh, J. S. Sanghera, D. Schaafsma, B. J. Cole, V. Q. Nguyen, R. E. Miklos, and I. D. Aggarwal, "Fabrication of single-mode chalcogenide optical fiber," Lightwave Technology, Journal of **16**, 214-217 (1998).

109. C. Florea, M. Bashkansky, Z. Dutton, J. Sanghera, P. Pureza, and I. Aggarwal, "Stimulated Brillouin scattering in single-mode As2S3 and As2Se3 chalcogenide fibers," Optics Express **14**, 12063-12070 (2006).

110. A. Mori, H. Masuda, K. Shikano, K. Oikawa, K. Kato, and M. Shimizu, "Ultra-wideband tellurite-based Raman fibre amplifier," Electronics Letters **37**, 1442-1443 (2001).

111. A. Mori, K. Kobayashi, M. Yamada, T. Kanamori, K. Oikawa, Y. Nishida, and Y. Ohishi, "Low noise broadband tellurite-based Er 3-doped fibre amplifiers," Electronics Letters **34**, 887-888 (1998).

112. Y. Ohishi, A. Mori, M. Yamada, H. Ono, Y. Nishida, and K. Oikawa, "Gain characteristics of tellurite-based erbium-doped fiber amplifiers for 1.5 μm broadband amplification," Opt. Lett **23**, 274-276 (1998).

113. A. Mori, T. Sakamoto, K. Kobayashi, K. Shikano, K. Oikawa, K. Hoshino, T. Kanamori, Y. Ohishi, and M. Shimizu, "1.58-μm broad-band erbium-doped tellurite fiber amplifier," Lightwave Technology, Journal of **20**, 822-827 (2002).

114. J. D. Minelly, "New materials for fiber optic amplifiers," Lasers and Electro-Optics Society 1999 12th Annual Meeting. LEOS'99. IEEE **2** (1999).

115. J. S. Wang, E. M. Vogel, and E. Snitzer, "Tellurite glass: a new candidate for fiber devices," Optical materials(Amsterdam) **3**, 187-203 (1994).

116. T. Luo, "Ultra-broadband Er3+ doped tellurite glass fiber amplifier," D. T. R. Agency, ed. (DTIC, 2003).

117. A. Mori, H. Masuda, K. Shikano, and M. Shimizu, "Ultra-wide-band tellurite-based fiber Raman amplifier," Lightwave Technology, Journal of **21**, 1300-1306 (2003).

118. V. G. Plotnichenko, V. O. Sokolov, V. V. Koltashev, E. M. Dianov, I. A. Grishin, and M. F. Churbanov, "Raman band intensities of tellurite glasses," Optics Letters **30**, 1156-1158 (2005).

119. G. S. Murugan, T. Suzuki, and Y. Ohishi, "Tellurite glasses for ultrabroadband fiber Raman amplifiers," Applied Physics Letters **86**, 161109 (2005).

120. G. Qin, A. Mori, and Y. Ohishi, "Brillouin lasing in a single-mode tellurite fiber," **32**, 2179-2181 (2007).

121. G. Qin, H. Sotobayashi, M. Tsuchiya, A. Mori, T. Suzuki, and Y. Ohishi, "Stimulated Brillouin Scattering in a Single-Mode Tellurite Fiber for Amplification, Lasing, and Slow Light Generation," **26**, 492-498 (2008).

122. R. H. Lehmberg, "Numerical study of phase conjugation in stimulated Brillouin scattering from an optical waveguide," (NRL-MR-4985, Naval Research Lab., Washington, DC (USA), 1982).

123. S. M. Massey, J. B. Spring, and T. H. Russell, "Stimulated Brillouin scattering continuous wave phase conjugation in step-index fiber optics," Opt. Express **16**, 16873-16885 (2008).

124. T. M. Shay, V. Benham, J. T. Baker, B. Ward, A. D. Sanchez, M. A. Culpepper, D. Pilkington, J. Spring, D. J. Nelson, and C. A. Lu, "First experimental demonstration of self-synchronous phase locking of an optical array," Optics Express **14**, 12015-12021 (2006).

125. M. K. Culpepper, "Coherent combination of fiber laser beams," Proc. SPIE **4629**, 99-108 (2002).

126. S. Hofer, H. Zellmer, J. P. Raske, and A. Tunnermann, "Coherent beam combining of fiber amplifiers," in *Lasers and Electro-Optics Europe*(2003), p. 635.

127. S. J. Augst, T. Y. Fan, and A. Sanchez, "Coherent beam combining and phase noise measurements of ytterbium fiber amplifiers," Optics Letters **29**, 474-476 (2004).

128. J. Anderegg, S. J. Brosnan, M. E. Weber, H. Komine, and M. G. Wickham, "8-W coherently phased 4-element fiber array," Proceedings of SPIE **4974**, 1-6 (2003).

129. J. Anderegg, S. Brosnan, E. Cheung, P. Epp, D. Hammons, H. Komine, M. Weber, and M. Wickham, "Coherently coupled high-power fiber arrays," Proceedings of SPIE **6102**, 61020U (2006).

130. M. Valley, G. Lombardi, and R. Aprahamian, "Beam combination by stimulated Brillouin scattering," Optical Society of America, Journal, B: Optical Physics **3**, 1492-1497 (1986).

131. D. A. Rockwell, and C. R. Giuliano, "Coherent coupling of laser gain media using phase conjugation," Optics Letters **11**, 147-149 (1986).

132. R. H. Moyer, "Beam combination with stimulated Brillouin scattering: A review," SPIE Conference on Laser Wavefront Control, 25-32 (1988).

133. D. L. Carroll, R. Johnson, S. J. Pfeifer, and R. H. Moyer, "Experimental investigations of stimulated Brillouin scattering beam combination," J. Opt. Soc. Amer. B **9**, 2214–2224 (1992).

134. D. S. Sumida, D. C. Jones, and D. A. Rockwell, "An 8.2 J phase-conjugate solid-state laser coherently combiningeight parallel amplifiers," Quantum Electronics, IEEE Journal of **30**, 2617-2627 (1994).

135. H. Becht, "Experimental investigation on phase locking of two Nd: YAG laser beams by stimulated Brillouin scattering," J Opt Soc Am B **15**, 16-78 (1998).

136. J. Falk, M. Kanefsky, and P. Suni, "Limits to the efficiency of beam combination by stimulated Brillouin scattering," Opt. Lett **13**, 39–41 (1988).

137. S. Sternklar, D. Chomsky, S. Jackel, and A. Zigler, "Misalignment sensitivity of beam combining by stimulated Brillouin scattering," Opt. Lett **15**, 469-470 (1990).

138. R. Moyer, M. Valley, and M. Cimolino, "Beam combination through stimulated Brillouin scattering," Optical Society of America, Journal, B: Optical Physics **5**, 2473-2489 (1988).

139. N. F. Andreev, E. A. Khazanov, O. V. Kulagin, B. Z. Movshevich, O. V. Palashov, G. A. Pasmanik, V. I. Rodchenkov, S. Scott, and P. Soan, "A two-channel repetitively pulsed Nd: YAG laser operating at 25 Hz with diffraction-limited beam quality," IEEE Journal of Quantum Electronics **35**, 110-114 (1999).

140. G. T. Moore, "A model for diffraction-limited high-power multimode fiber amplifiers using seeded stimulated Brillouin scattering phase conjugation," IEEE Journal of Quantum Electronics **37**, 781 (2001).

141. A. F. Vasil'ev, S. B. Gladin, and V. E. Yashin, "Pulse-periodic Nd: YAlO3 laser with a phase-locked aperture under conditions of phase conjugation by stimulated Brillouin scattering," Quantum Electronics **21**, 494-497 (1991).

142. S. M. Willis, and W. B. Roh, "Beam phasing properties of optical fiber as phase conjugate mirror," in *Lasers and Electro-Optics Society, 2003. LEOS 2003. The 16th Annual Meeting of the IEEE*(IEEE, 2003), pp. 105-106.

143. K. C. Brown, "Passive multiple beam combination of optical fibers via stimulated Brillouin scattering," in *Department of Engineering Physics*(Air University, AFIT, Wright-Patterson AFB, 2005).

144. B. W. Grime, W. B. Roh, and T. G. Alley, "Phasing of a two-channel continuous-wave master oscillator-power amplifier by use of a fiber phase-conjugate mirror," Optics Letters **30**, 2415-2417 (2005).

145. A. Liu, "Novel SBS suppression scheme for high-power fiber amplifiers," Proceedings of SPIE **6102**, 61021R (2006).

146. A. Liu, "Suppressing stimulated Brillouin scattering in fiber amplifiers using nonuniform fiber and temperature gradient," (OSA, 2007), pp. 977-984.

147. C. Wang, F. Zhang, Y. Lu, R. Geng, Z. Tong, T. Ning, and S. Jian, "Study of stimulated Brillouin scattering effect in high-power single-frequency fiber amplifiers," Chinese Journal of Lasers **33**, 1630-1635 (2006).

148. A. Yariv, "Optical electronics in modern communications," (1997).

149. K. Tankala, B. Samson, A. Carter, J. Farroni, D. Machewirth, N. Jacobson, U. Manyam, A. Sanchez, A. Galvanauskas, W. Torruellas, and Y. Chen, "New Developments in High Power Eye-Safe LMA Fibers," in *Photonics West*(SPIE, San Jose, CA, 2006).

150. Y. Jeong, J. K. Sahu, D. J. Richardson, and J. Nilsson, "Seeded erbium/ytterbium codoped fibre amplifier source with 87 W of single-frequency output power," Electronics Letters **39**, 1717-1719 (2003).

151. C. Alegria, Y. Jeong, C. Codemard, J. K. Sahu, J. A. Alvarez-Chavez, L. Fu, M. Ibsen, and J. Nilsson, "83-W single-frequency narrow-linewidth MOPA using large-core erbium-ytterbium co-doped fiber," Photonics Technology Letters, IEEE **16**, 1825-1827 (2004).

152. M. A. Dubinskii, and L. D. Merkle, "Ultrahigh-gain bulk solid-state stimulated Brillouin scattering phase-conjugation material," Optics Letters **29**, 992-994 (2004).

153. M. J. Adams, *An introduction to optical waveguides* (Chichester: Wiley, 1981).

154. S. Jiang (Telephone call, 2006).

155. J. Nilsson, J. K. Sahu, Y. Jeong, W. A. Clarkson, R. Selvas, A. B. Grudinin, and S. U. Alam, "High power fiber lasers: new developments," Proc. of SPIE **4974**, 51 (2003).

156. V. I. Kovalev, and R. G. Harrison, "Continuous wave stimulated Brillouin scattering in optical fibers: new results and applications for high power lasers," Proceedings of SPIE **5975**, 59750L (2006).

157. T. Russell, W. Roh, and J. Marciante, "Incoherent beam combining using stimulated Brillouin scattering in multimode fibers," Optics Express **8**, 246-254 (2001).

158. K. C. Brown, T. H. Russell, T. G. Alley, and W. B. Roh, "Passive combination of multiple beams in an optical fiber via stimulated Brillouin scattering," Optics Letters **32**, 1047-1049 (2007).

159. I. 11146-1, "Lasers and laser-related equipment - Test methods for laser beam widths, divergence angles, and beam propagation ratios - Part 1: Stigmatic and simple astigmatic beams," (International Organization for Standardization, 2005).

160. S. M. Massey, "Continuous wave stimulated Brillouin scattering phase conjugation in optical fiber," in *Solid State and Diode Laser Technology Review*, I. McKinnie, ed. (Directed Energy Professional Society, Albuquerque, NM, 2008).

161. S. M. Massey, and T. H. Russell, "Phase analysis of stimulated Brillouin scattering in long, graded-index optical fiber," Opt. Express **16**, 11496-11505 (2008).

162. M. Born, and E. Wolf, *Principles of Optics: Electromagnetic Theory of Propagation, Interference and Diffraction of Light* (Cambridge University Press, 1999).

163. P. R. Bevington, and D. K. Robinson, *Data Reduction and Error Analysis for the Physical Sciences (2d ed.)* (McGraw-Hill, New York, 1992).

164. S. Meister, T. Riesbeck, and H. J. Eichler, "Glass fibers for stimulated Brillouin scattering and phase conjugation," Laser and Particle Beams **25**, 15-21 (2007).

165. K. S. Abedin, "Stimulated Brillouin scattering in single-mode tellurite glass fiber," Opt. Express **11**, 2641-2645 (2006).

166. K. Tankala, "Large Mode Area Erbium-Ytterbium Fibers," (DTIC, 2006).

167. J. P. Koplow, D. A. V. Kliner, and L. Goldberg, "Single-mode operation of a coiled multimode fiber amplifier," Opt. Lett **25**, 442–444 (2000).

168. "www.blazephotonics.com," (Crystal Fibre A/S, 2005), Accessed June 16, 2008.

169. M. Damzen, and H. Hutchinson, "Laser pulse compression by stimulated Brillouin scattering in tapered waveguides," Quantum Electronics, IEEE Journal of **19**, 7-14 (1983).

REPORT DOCUMENTATION PAGE

Form Approved
OMB No. 0704-0188

1. REPORT DATE *(DD-MM-YYYY)*	2. REPORT TYPE	3. DATES COVERED *(From - To)*
12-09-2008	Doctoral Dissertation	Sep 2005 – Sep 2008

4. TITLE AND SUBTITLE

Stimulated Brillouin Scattering Phase Conjugation in Fiber Optic Waveguides

5a. CONTRACT NUMBER

5b. GRANT NUMBER

5c. PROGRAM ELEMENT NUMBER

6. AUTHOR(S)

Massey, Steven M., Major, USAF

5d. PROJECT NUMBER
F2KBAB7355G005

5e. TASK NUMBER

5f. WORK UNIT NUMBER

7. PERFORMING ORGANIZATION NAME(S) AND ADDRESS(ES)
Air Force Institute of Technology
Graduate School of Engineering and Management (AFIT/EN)
2950 Hobson Way
WPAFB, OH 45433-7765

8. PERFORMING ORGANIZATION REPORT

AFIT/DS/ENP/08-S03

9. SPONSORING / MONITORING AGENCY NAME(S) AND ADDRESS(ES)
High Energy Laser Joint Technology Office
ATTN: Walt Fink
901 University Blvd SE Ste 100
Albuquerque NM 87106
505-248-8204

10. SPONSOR/MONITOR'S ACRONYM(S)

11. SPONSOR/MONITOR'S REPORT NUMBER(S)

12. DISTRIBUTION / AVAILABILITY STATEMENT
APPROVED FOR PUBLIC RELEASE

13. SUPPLEMENTARY NOTES

14. ABSTRACT
The objective of this research effort was to demonstrate the path to continuous wave, coherent beam combination through stimulated Brillouin scattering phase conjugation in optical fiber. This work experimentally determined the fiber parameters necessary for phase conjugation in step-index optical fiber. Continuous wave phase conjugation using stimulated Brillouin scattering in step-index fibers was achieved for the first time with a fidelity of 0.8 and a threshold power of 16 W in a 15-m fiber with 0.13 NA. A fidelity of 0.8 was also achieved using 40 m of fiber with 0.06-NA and a threshold power of 15 W. The fidelity of phase conjugation was found to decline by ~45% in an additional 20 m of 0.13-NA fiber and by ~15% in 20 m of the 0.06-NA fiber. The effective Brillouin gain coefficient of the multimode fibers was found to vary directly with fidelity. A new technique using interference to measure fidelity was tested, and stimulated Brillouin scattering in a 2.5-km, graded-index fiber was found to produce beam cleanup to the fundamental fiber mode of the fiber with fidelity less than 0.1. This work demonstrated that coherent beam combining via continuous wave phase conjugation in optical fiber is achievable.

15. SUBJECT TERMS
Laser Amplifiers, Phase Conjugation, Brillouin Scattering, Stokes Radiation, Nonlinear Optics, Fiber Optics, Coherent Beam Combination

16. SECURITY CLASSIFICATION OF:			17. LIMITATION OF ABSTRACT	18. NUMBER OF PAGES	19a. NAME OF RESPONSIBLE PERSON
a. REPORT	b. ABSTRACT	c. THIS PAGE			Timothy H. Russell, AFIT/ENP
U	U	U	UU	198	19b. TELEPHONE NUMBER *(include area code)* 937-238-5818

Standard Form 298 (Rev. 8-98)
Prescribed by ANSI Std. Z39.18